ISSN 1349-6832

JEOL NEWS

June 2020
Vol.55
No.1

Electric Field and Charge Density of a $BiFeO_3$-$SrTiO_3$ Interface

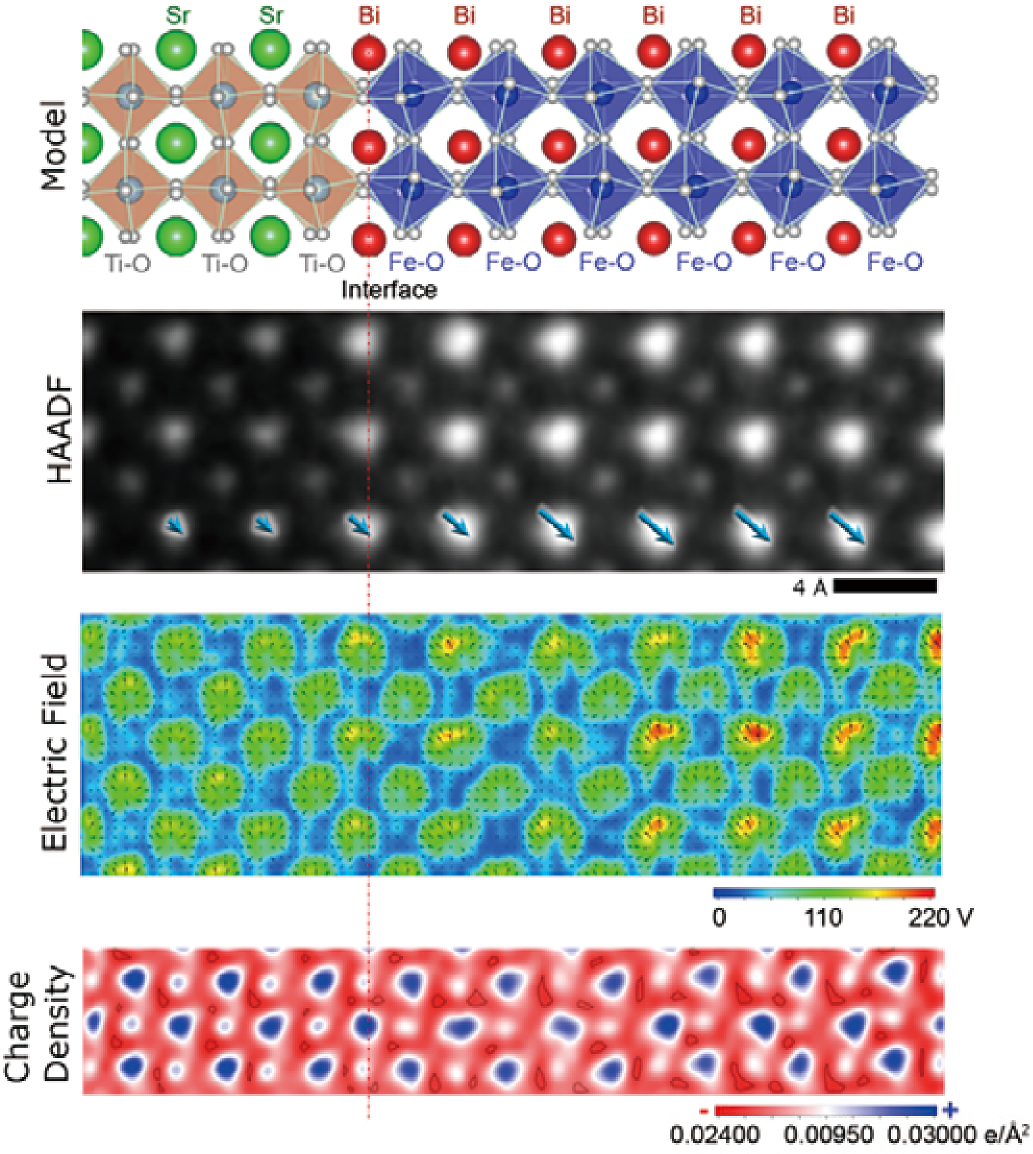

Contents

JEOL NEWS
June 2020 Vol.55 No.1

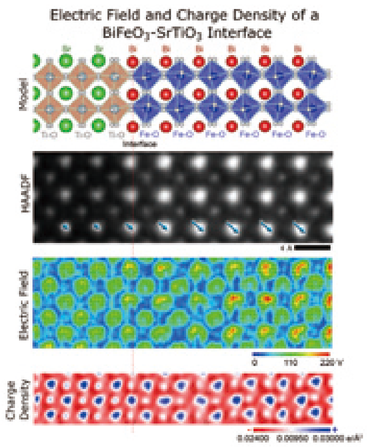

Cover micrograph

The high angle annular dark field (HAADF) image, electric field, and charge density calculated from atomic resolution four-dimensional scanning transmission electron microscopy (4D STEM) data showing the polarization gradient across a BiFeO$_3$-SrTiO$_3$ (ferroelectric-insulator) interface. The corresponding atomic structure model from density functional theory is shown at the top (see page 2 to 8).

Atomically Resolved Electric Field and Charge Density Imaging via 4D STEM

Christopher Addiego[1], Wenpei Gao[2], Xiaoqing Pan[1, 2, 3]

[1] Department of Physics and Astronomy, University of California, Irvine

[2] Department of Materials Science and Engineering, University of California, Irvine

[3] Irvine Materials Research Institute, University of California, Irvine

The redistribution of electrons when atoms are bound together in a lattice determines many of the properties of bulk crystalline materials and nanostructured materials. Therefore, the measurement of electron charge density is an important step in building structure-property relationships. With the sub-Å spatial resolution possible in an aberration-corrected scanning transmission electron microscope (AC-STEM), they are the ideal instrument to probe the electron interaction with local charges in materials. Recording a full diffraction pattern for every position of the scanning probe can capture the details of how the electron beam is influenced by local electric field. However, this has only recently become possible due to the developments in fast pixelated electron detectors. In this article, we will describe a method for extracting the real-space charge density from four-dimensional scanning diffraction data, utilizing the JEOL JEM-ARM300F aberration-corrected S/TEM equipped with a Gatan OneView camera and STEMx system at the University of California, Irvine Materials Research Institute (IMRI). By analyzing the high-quality images of the real-space charge density, we studied the dipole in ferroelectric $BiFeO_3$ and the charge redistribution at a $BiFeO_3$-$SrTiO_3$ (ferroelectric-insulator) interface.

Introduction

The development of aberration corrected transmission electron microscopes and fast pixelated electron detectors has led to the emergence of four-dimensional STEM (4D STEM) imaging, where a diffraction pattern is captured for every scanning position, as a prominent new method for studying materials down to atomic resolution. Diffraction patterns carry a great wealth of information about the electron beam's interaction with the sample, much of which is discarded by conventional STEM detectors when the signal is integrated to generate only a single pixel value per position of the probe. Some angular dependence can be extracted from the varying collection angles of conventional detectors, but most information is still lost. Initial efforts to capture additional information from conventional STEM detectors resulted in the development of segmented detectors [1] and differential phase contrast (DPC) imaging, which splits a monolithic detector into several sections and estimates the momentum shift of the probe by measuring the intensity difference between opposing segments; this is shown schematically in **Fig. 1** a, b. Imaging with this method was first demonstrated at atomic resolution by Shibata, et al [2]. Subsequent work used DPC to image the electric field surrounding single gold atoms [3] and in GaN [4]. Integrated DPC (iDPC) imaging has also proven to be an effective method for simultaneously imaging both light and heavy elements [5]. For example, recent work has used iDPC to measure the shift of oxygen octahedra in $PbTiO_3$-$SrTiO_3$ superlattices and accurately quantify the polarization [6].

As high-speed pixelated electron detectors and cameras have proliferated in the electron microscopy community, 4D STEM has garnered significant interest due to its versatility. With a 4D diffraction dataset, any type of STEM image (bright field, annular bright field, or annular dark field) can be generated [7]. Virtual apertures with arbitrary shape applied in post processing can also be used to generate images that would be impossible with a physical aperture plate [8]. But arbitrary image reconstruction is only the beginning of what is possible. If diffraction disks are separated, their spacing can be analyzed to map strain [9] or the symmetry can be analyzed to determine crystallographic orientation [10]. Nanocrystalline ordering in materials that are typically too disordered for high resolution imaging, such as organic semiconductors, can also be studied with this method [11]. If the diffraction disks are slightly overlapped, ptychography can be used to reconstruct the full exit wave function of the probe [12]. This enables image reconstruction with ultra-high resolution [13] and also retrieval of the projected atomic potential [14, 15]. In this condition, techniques for quantitively mapping the sample's thickness and orientation have also been developed [16, 17].

》 Irvine, CA 92697, USA | E-mail: xiaoqing.pan@uci.edu

Fig. 1 Experimental setup and the electric field in $SrTiO_3$.

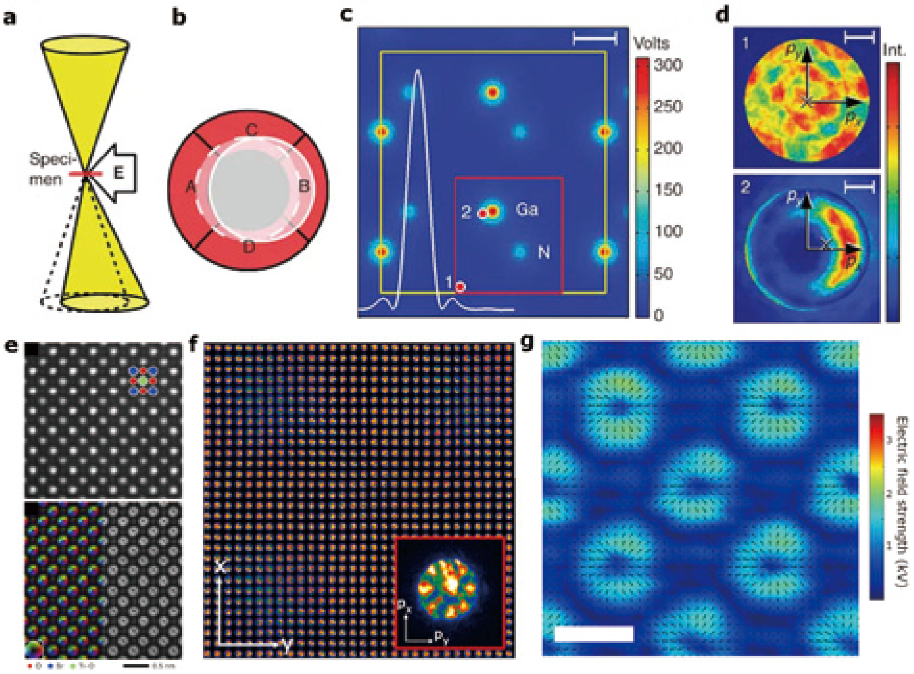

a, A schematic of the electron probe interacting with an electric field in the sample. An electric field pointing left shifts the beam to the right. b, A DPC detector with the center disk of the CBED pattern overlaid. The dotted circles show the undeflected position of the center disk and the solid circle shows the deflected position that results from interaction with an electric field. c, d, The projected potential map of a simulated GaN lattice from DFT projected along $[11\bar{2}0]$ (c). The white curve shows a line profile of a simulated electron probe. The markers 1 and 2 indicate the position of the probe associated with the CBED patterns in d. The × in each CBED pattern indicates the shift in the momentum from the origin. The scale bar in c is 1 Å. The scale bar in d is 10 mrad. a-d are reproduced from Muller et al., *Nat. Comm., 2014* [18]. e, On top, a HAADF image of STO with the atomic structure overlaid. On bottom, the electric field measured from DPC. The left image shows the direction and magnitude of the electric field based on the inset color wheel. The right image shows only the magnitude of the electric field. e is reproduced from Shibata et al., Nat. Comm., 2017 [3]. f, Raw 4D STEM data from 1 unit cell of STO; the inset shows a zoomed in image of one CBED pattern. g, the electric field calculated from 4D STEM.

Our research at UCI has focused on using the highly overlapped convergent beam electron diffraction (CBED) patterns for reconstructing the electric field and charge density at atomic resolution as originally proposed by Muller et al [18]. In this technique, the CBED pattern is used as momentum space image of the electron probe. Just as in DPC imaging, a probe placed near to a nucleus will experience a strong shift in its momentum due to the electric field of the nucleus; this is shown for a simulated GaN lattice in Fig. 1 c, d from Muller et al. [18] However, in 4D STEM, the full diffraction pattern is analyzed to determine the momentum shift instead of integrating different segments. In thin samples, the change in momentum of the probe (also called the momentum transfer) is negatively proportional to the average electric field in the interaction volume [18, 19]. This linear relationship relies on several assumptions, such as the probe experiencing minimal broadening during propagation and the electric field being approximately constant over the interaction volume. However, for samples below ~6 nm thickness, these conditions can generally be met and this technique can quantitatively map the electric field at atomic resolution. The local charge density can then be calculated from the electric field through the differential form of Gauss' law from basic electrodynamics.

Various other techniques using X-ray diffraction [20] and transmission electron microscopy (TEM) have been developed to study real-space charge density in the past, but they required significant simulation and analysis of diffraction data from the material under study. Quantitative convergent beam electron diffraction is one such example where experimental CBED patterns must be fit to simulated CBED patterns before determining the charge density [21]. This methodology of fitting experimental data to simulation makes it difficult to study irregular structures like defects and interfaces because of the increasing complexity of the necessary simulations. But atomic resolution 4D STEM allows us to overcome this barrier because each diffraction pattern in the 4D dataset is acquired from an area defined by the size of the electron probe and the highly localized charge distribution can be calculated without the need for simulation [18, 19]. To image the charge density surrounding a defect or interface, we need only to position our scanning probe over the desired region; this opens the door to imaging the charge density in all kinds of nanostructured materials.

In our work, we applied this method to a bulk $SrTiO_3$ (STO), bulk ferroelectric $BiFeO_3$ (BFO), and a BFO-STO interface. Ferroelectrics are an ideal system for applying this technique because they have an intrinsic polarization and electric field; in particular, BFO has a large spontaneous polarization that is caused by the deformation of the Bi 6s lone pair which induces a rotation of the FeO octahedra [22, 23]. It has been shown previously that DPC is sensitive to the change in polarization across ferroelectric domain walls in $BaTiO_3$[2], but not in atomic resolution images. In this review article, we will show how 4D STEM can be used to study the electric field and charge density at atomic resolution and briefly describe some of our related simulation studies [24, 25].

Experimental Results and Discussion

Electric field measurement in bulk $SrTiO_3$

4D STEM data was collected on a JEOL JEM-ARM300F aberration-corrected S/TEM. Using a convergence angle of 33 mrad, the achievable FWHM of the probe intensity is about 0.6 Å. Diffraction patterns were recorded at 300 fps on a Gatan OneView camera synchronized using the Gatan STEMx system. The fast framerate enables us to capture data from large regions of interest at a small step size while maintaining minimal sample drift. Similar to other studies, we used STO as a model system for examining the electric field. A representative HAADF image of STO is shown on top in Fig. 1e and, for comparison, the associated electric field image from DPC is shown on the bottom, both from Shibata et al [3]. We collected 4D STEM data from STO with a 0.2 Å step size; raw 4D STEM data from one unit cell of STO is shown in Fig. 1f.

Each diffraction pattern was analyzed to determine the momentum transfer ($\mathbf{p}_{\mathrm{xy}}$) of the probe by calculating the shift of the center of mass ($\Delta\mathbf{COM}$) of the image; the shift in the center of mass is directly proportional to the momentum transfer ($\mathbf{p}_{\mathrm{xy}} = p_z\Delta\mathbf{COM}$), where p_z is the momentum of the electron probe along the beam direction. The momentum transfer is then related to the electric field by

$$\mathbf{E} = -\mathbf{p}_{\mathbf{xy}}\frac{v_z}{e\Delta z}$$

where e is the elementary charge, v_z is the velocity of electrons along the beam direction, and Δz is the sample thickness along the beam direction [18, 19]. Since p_z and v_z are determined by the accelerating voltage, the electric field at every point in the scan can be quantitively determined from $\mathbf{p}_{\mathrm{xy}}$ and the sample thickness. We measured the thickness of our sample to be 5.6 ± 1 nm using position averaged CBED [16]. The resulting electric field is shown in Fig. 1g. The electric field points radially outward from each nucleus, as would be expected from the Coulomb potential surrounding a positive point charge (the nucleus in this case) and in agreement with previous DPC measurements. Since STO is not a ferroelectric and the structure is symmetric, there is no intrinsic polarization and this is reflected in fact that the electric field surrounding each atom is rotationally symmetric. The relative magnitude of the field also reflects the atomic number of the nucleus, with the heavier Sr atomic columns showing a slightly stronger field than the Ti/O columns, which is stronger than the O columns.

Electric field quantification

We studied the quantification of the electric field from the momentum transfer of the electron probe in more detail using bulk STO as a model system. Extensive simulations have been done to show the range of sample thicknesses for which the electric field is easily quantifiable is limited to only 5-6 nm in general [19]. However, from our experiments, electric field maps from regions with up to 22 nm thickness appeared qualitatively similar to the electric field maps from regions with only 5 nm thickness. **Figure 2**a and b show maps of the momentum transfer of the electron probe from two regions of an STO wedge sample where the thickness is 5.6 nm and 22.5 nm, respectively. Despite the qualitative similarity, quantifying the momentum transfer for each region reveals that the linear relationship between electric field and momentum transfer has broken down. If it held true, the measured momentum transfer should increase linearly with sample thickness. This is not the case for the data shown in Fig. 2; the magnitude of the momentum transfer measured for both regions are similar, as shown by the color scale.

To explain this divergence of the qualitative and quantitative behavior, we performed a series of multi-slice imaging simulations to examine how the measured momentum transfer is affected by the sample thickness and the magnitude of the local electric field. Simulations were conducted using a 15 nm thick sample, with the probe positioned at three positions of increasing distance from a Sr column, varying the local field magnitude; the results are shown in Fig. 2c. We found that the momentum transfer grew linearly within the first 6nm for all probe positions, indicating that the electric field can be quantified accurately within this thickness range (fitting a linear model to all three curves in this range results in a reduced-$R^2 > 0.9$). Beyond 6 nm, the behavior at the three positions diverges, with only the probe placed furthest from the Sr column, in the weakest electric field, growing linearly. However, the momentum transfer at all positions always maintains the correct qualitative ordering, with the probe closest to the atomic column experiencing the largest change in momentum. This explains the qualitative appearance of our experimental momentum transfer maps collected from thick regions of the sample. Also, surprisingly, it shows that the weak field between atoms can be quantified even for samples that are thicker than 6 nm.

Electric field measurement in $BiFeO_3$

We also measured the electric field in bulk BFO using the same method. The BFO lattice has a rhombohedral structure and is polarized along the (111) pseudo-cubic (pc) direction (**Fig. 3**a),

Fig. 2 Thickness effects on measured momentum transfer.

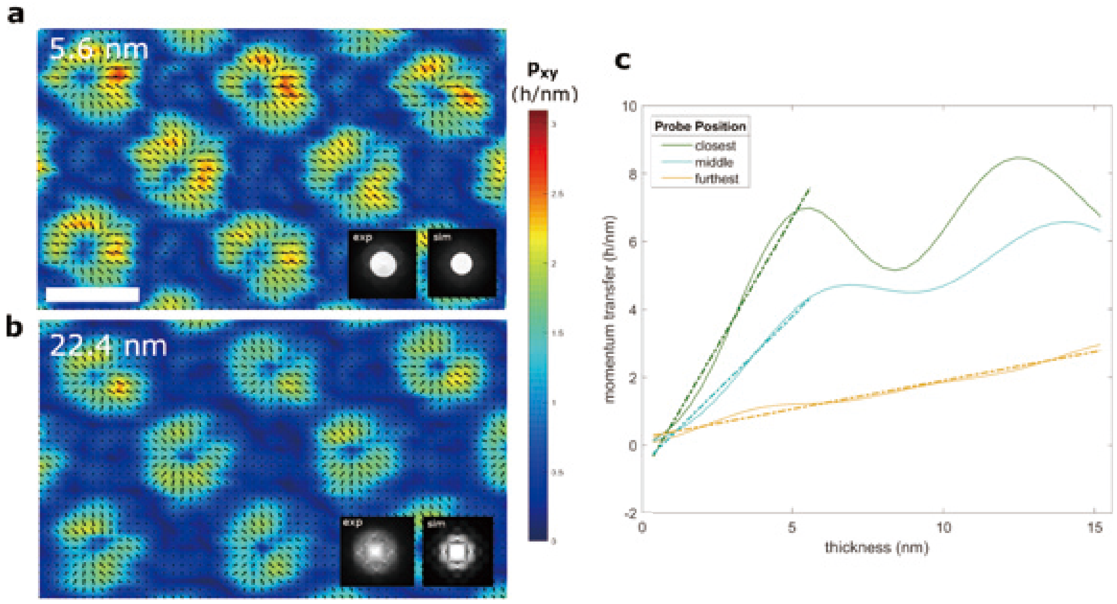

a, b, Momentum transfer maps of STO from a regions 5.6 nm (a) and 22.5 nm (b) in thickness. Insets show experimental and simulated PACBED patterns for comparison. c, The simulated momentum transfer plotted as a function of sample thickness for the electron probe at three different positions near an Sr column. The dashed lines are the result of a linear fitting. Scale bar: 2 Å which results in a displacement of the Fe atom away from the center of the four surrounding Bi atoms along the body diagonal, which can be imaged in the $(100)_{pc}$ projection. This results in a dipole pointing in the opposite direction. Fig. 3b is a HAADF image along the $(100)_{pc}$ direction with a vector map of the dipole in each unit cell overlaid. The electric field in bulk BFO also shows this dipole moment; Fig. 3c shows the electric field from one unit cell of bulk BFO. Notice that the rotational symmetry of the electric field found in STO is now broken in BFO; each cation column now shows a bias in the electric field towards the bottom right, as expected from the internal dipole which points in the opposite direction.

Measurement of the charge density in bulk $SrTiO_3$ and $BiFeO_3$

With a high quality map of the electric field, the charge density can be determined simply by calculating the divergence of the field. Note that STEM is a projective measurement, so the 2D map of the electric field yields a 2D map of the charge density. The experimental charge density maps from STO and BFO unit cells are shown in **Fig. 4** a and b, respectively. The charge density contains contributions from both the positive nuclei and the surrounding electrons; the positive nuclei appear as broad gaussians due to shielding from core electrons and the size of the electron probe. Just as in DPC imaging, oxygen is readily visible in the charge density map for both STO and BFO. The tilt of the oxygen octahedra in polarized BFO causes the oxygen column to split in this projection, as shown in Fig. 3a; this is visible in the BFO charge density as an elongation of the oxygen columns that is not present in STO.

The STO structure is symmetric, so there is little deformation in the shape of the atomic columns. In addition, the bonding in STO is primarily ionic, so the valence charge between atoms appears uniformly distributed with only weak negative concentrations, indicating mostly isotropic bonding. In contrast, the Bi and Fe/O columns appear deformed. Deformation of the Fe/O columns is caused by both the tilting of the oxygen octahedra, which shifts the oxygen atoms out of line with the Fe atom, and anisotropic bonding between Fe d-orbital electrons and O atoms. The covalent nature of bonding of Bi-O and Fe-O is also demonstrated by the strong accumulation of negative charge into distinctive pockets in interatomic regions.

Previous simulation studies have pointed out that current STEM probe sizes are still large compared to atomic nuclei and that, in this regime, the interaction between probe tails and the deep potential well of the nucleus may dominate the signal even when the probe is placed between atoms, making it difficult to detect the interatomic electron distribution [26]. To better understand the effect of charge redistribution on imaging charge density with 4D STEM, we initiated multi-slice 4D STEM simulations using STO as a model system. Multi-slice simulations were performed using the atomic potentials constructed by two different methods. In one case, delta functions were used to represent atomic nuclei in the potential and no screening from core electrons was introduced. In the other case, the Individual Atomic Model [27-29] (IAM) was used to calculate the potential landscape; this model includes contributions from core electrons which shield the nuclear charge [30], but not valence electrons that participate in bonding and

Fig. 3 Atomic structure and electric-field dipole of $BiFeO_3$.

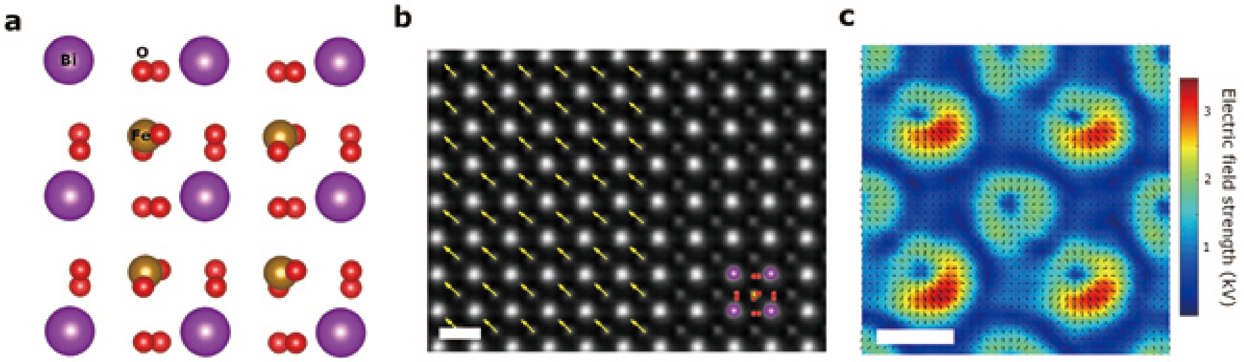

a, Structure model of BFO projected along $(100)_{pc}$; the Fe atoms are displaced towards bottom right, so the dipole points towards top left in this projection. b, HAADF image of BFO with a polarization map overlaid showing the orientation of the dipole in each unit cell. Scale bar: 4 Å. c, Electric field map from a BFO unit cell. The electric field surrounding each atom is biased towards bottom right, opposite the dipole, as expected. Scale bar: 2 Å.

Fig. 4 Real-space charge density mapping in $SrTiO_3$ and $BiFeO_3$.

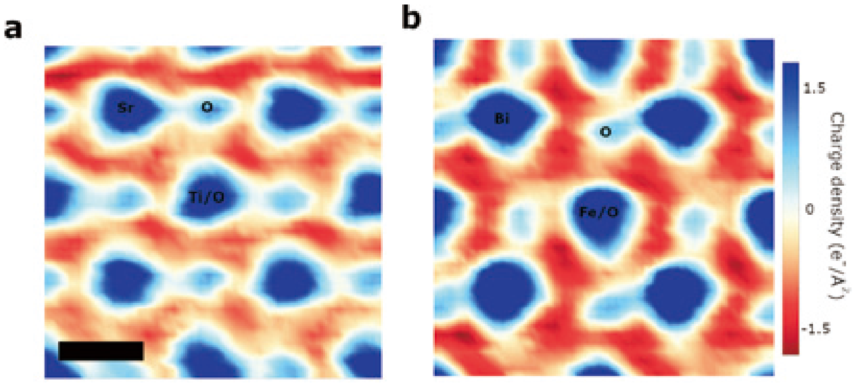

a, Charge density map of bulk STO from scanning diffraction experiments. b, Charge density map of bulk BFO. Scale bar: 2 Å.

might appear in the interatomic regions. IAM is the method used in most conventional STEM imaging simulations. By simulating 4D data with probe conditions identical to experiment and then following the same procedure to calculate the charge density, we can identify the effects of the probe size and the nuclear cores.

Our results from ideal STO structures with only 0.4 nm thickness (1 unit cell) and 5.6 nm thickness (matching with experiment) are shown in **Fig. 5**. Since there is no negative charge modeled in the delta function simulations and no valence electrons in the IAM simulations, we will refer to these as divergence maps to distinguish them. With the delta function potentials, for a 0.4 nm thickness model (Fig. 5a), clear +/– oscillations are visible surrounding each nucleus for the 1 unit cell structure. These oscillations are caused by the interactions of the probe tails with the nuclear core. However, the oscillations do not appear in divergence maps using IAM (Fig. 5c), indicating shielding from core electrons weakens the interaction with the probe tails significantly, to the point where the positive nucleus is not dominating the signal when the probe is placed in interatomic regions. When a 5.6 nm thickness is used (Fig. 5 b, d), the differences between the delta function model and IAM are even more stark; it is clear from the contrast reversals that the delta function model is insufficient to represent the atomic potentials. In addition, the divergence maps from IAM simulations show a marked difference from the real charge density maps captured in experiment; in particular, there is a strong negative ring surrounding each atom which is not present in experimental charge density maps. This indicates that valence electrons also can make a significant contribution. Although this has not been shown definitively for 4D STEM, several publications combining experiment and simulation have shown that valence electrons can impact HRTEM and STEM image contrast [27, 28, 31]. Since HRTEM and STEM are connected via reciprocity, this supports the idea that valence electrons can affect 4D STEM data as well; but additional work is needed to thoroughly explore these effects.

Electric field and Charge density at a $BiFeO_3$-$SrTiO_3$ Interface

Finally, we applied atomic resolution 4D STEM to a BFO-STO interface. A structure model based on DFT calculations and HAADF image of the interface are shown in **Fig. 6** a and b, respectively. Based on the A-site contrast in the HAADF image, the interface is atomically sharp. Qualitatively, the electric field map (Fig. 6c) shows that the bias in the BFO electric field is reduced approaching the interface, but still penetrates the STO; this is also reflected in reduced atomic displacement in the HAADF image. In addition, the charge density (Fig. 6d) shows reduced elongation of the oxygen columns, indicating a smaller octahedral tilt, and reduced separation of negative charge pockets.

With 4D STEM, we can quantify changes in the atomic structure, charge distribution in the unit cell, and nuclear charge state all with the same data set. The atomic structure is fully characterized by combining the heavy element positions from the HAADF image and the light elements visible in the charge density image. In Fig. 6e, we plot the A-site atom's (Bi or Sr) displacement and the oxygen octahedral tilt across the interface. The octahedral tilt is determined by the peak intensity of the oxygen columns in the charge density image, which decreases as the octahedral tilt increases. The same quantities from DFT calculations are also shown in Fig. 6e. Note that changes in the atomic structure begin only in layer 1 of the BFO film.

Given that the charge density image shows us the distribution of both positive and negative charges, we can quantify the charge separation in each unit cell based on the weighted centers of the positive and negative charge in isolation. The distance between the positive and negative charge centers across the interface is shown in Fig. 6f. The charge separation shows three distinct regions; it starts out large in layers 4 and 5 of the BFO film, but then is reduced in layer 3, plateaus from BFO layer 2 through STO layer 1, where it is then reduced even further in STO layer 2. These changes in the charge distribution are not synchronized with the atomic structure, indicating that the electron distribution does not change as rigidly as the atomic structure. This shows that the electrons are more strongly affected by the electric field in the BFO layer, building up at the interface layer where the atomic structure does not fully compensate the charge.

To confirm the build-up of negative charge at the interface, we also studied the nuclear charge state of each atomic species present by integrating the charge density surrounding each atomic column. In this projection, Fe and Ti are overlapped with O atoms, so the measured charge state of each B-site atom is summed with the charge state of O atoms. In addition, O sites in BFO are omitted since the column is split in the (100) projection.

Fig. 5 Simulation studies of atomic potential models in $SrTiO_3$.

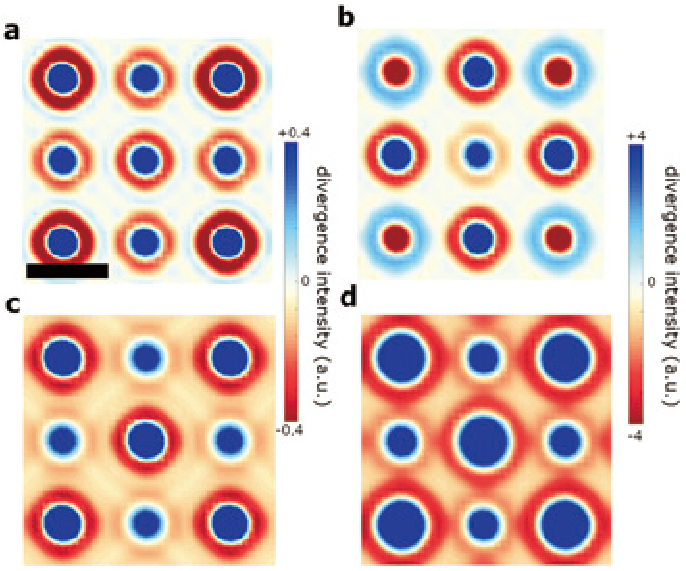

a, b, the divergence maps calculated from simulated 4D STEM data when atomic potentials are modeled with delta functions for 0.4 nm (a) and 5.6nm (b) samples. c, d, the divergence map when atomic potentials use the independent atomic model for 0.4 nm (c) and 5.6nm (d) samples. Scale bar: 2 Å.

Fig.6 Charge density map, O octahedron rotation and valence charge state at the interface between $SrTiO_3$ and $BiFeO_3$.

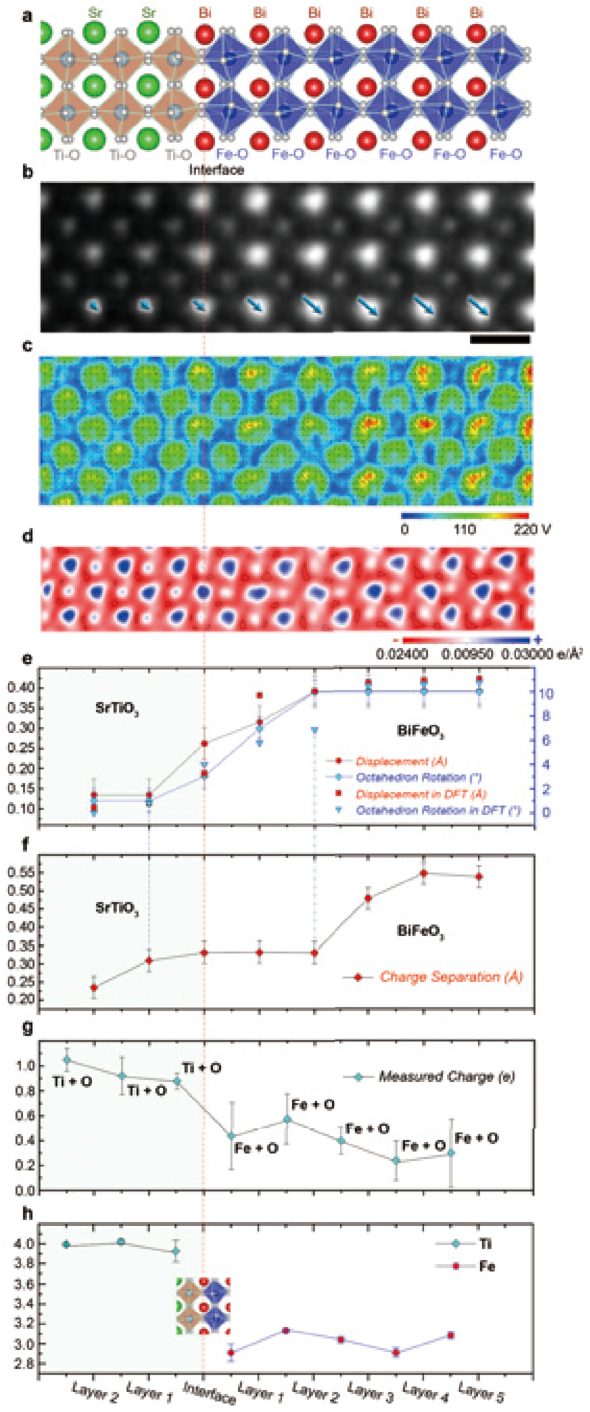

a, Atomic structure of a BFO-STO interface obtained from DFT calculations. b, Atomic-resolution HAADF-STEM image of BFO-STO. Scale bar: 4 Å. Arrows show the direction and relative magnitude of Bi/Sr displacement. c, The corresponding electric-field map derived from the 4D STEM dataset. d, Charge density map for BFO-STO. e, Changes in A-site displacement across the interface (that is, changes in the displacement of the Bi or Sr atom from the geometric center of the four nearest Fe or Ti atoms), determined experimentally and by DFT calculation (in ångströms; error bars denote standard deviation). Also shown is the O octahedron rotation determined experimentally (in degrees; error bars denote the detection limit) and from DFT calculations (scattered points). f, Charge separation between weighted centers of positive and negative charge within unit cells across the interface. Error bars denote the detection limit. g, Total charge of Ti + O and Fe + O on the two sides of the interface, measured using the charge density map. Error bars denote standard deviation. h, Valence states of Ti and Fe measured using high-energy-resolution EELS. Error bars denote standard deviation. Reproduced from *Gao et al., Nature, 2019* [24]. Copyright 2019 Nature Publishing Group.

The integration radius was determined based on Bader charge analysis [32, 33], which defines the boundary between atoms as the saddle point in calculated charge density. This is a method commonly used in DFT, where the full 3D charge density is available, but we have adapted the method to work with our projected 2D experimental data. In 2D, we define the boundary as the radius where the minimum charge density occurs surrounding the central nuclear peak. By performing the integration of the charge density image, and then comparing with DFT calculations, we can determine the partial charge state of each atomic column. The charge state of the Fe/O and Ti/O columns are plotted across the interface in Fig. 6g, showing a dip in the Ti/O and Fe/O charge states in the layers adjacent to the interface. This drop in the nuclear charge is also confirmed by measurements of the valence state of Ti and Fe from EELS (Fig. 6h) [34-36]. In particular, the Ti valence drops from 4+ to 3.7+ approaching the interface, indicating a mix of 4+ and 3+ states. These two together further confirm the build-up of electrons at the interface.

Summary

In summary, 4D STEM is a powerful paradigm for studying materials properties using TEM. Recent advancements in fast electron detection cameras have enabled electron microscopists to collect full diffraction patterns while scanning the electron probe, which can then be analyzed to calculate a wide variety of structural and electrical properties. We combine the high-resolution capabilities of AC-STEM with the new momentum-space information that is available in 4D STEM data to measure the electric field and charge density in perovskite materials with sub-atomic resolution. Using this method, we have shown that an interface between a ferroelectric and a non-ferroelectric insulator hosts an electron rich region confined to only a few unit cells. High resolution charge density imaging enabled by 4D STEM provides a new method for studying the charge distribution in nanostructured materials where the most interesting phenomena often emerge.

Acknowledgments

This work was supported by the US Department of Energy (DOE), Office of Basic Energy Sciences, Division of Materials Sciences and Engineering under grant DE-SC0014430. TEM experiments were conducted using the facilities in the Irvine Materials Research Institute (IMRI) at the University of California at Irvine.

References

[1] Haider, M.; Epstein, A.; Jarron, P.; Boulin, C., A versatile, software configurable multichannel STEM detector for angle-resolved imaging. *Ultramicroscopy* **1994**, *54* (1), 41-59.

[2] Shibata, N.; Findlay, S. D.; Kohno, Y.; Sawada, H.; Kondo, Y.; Ikuhara, Y., Differential phase-contrast microscopy at atomic resolution. *Nature Physics* **2012**, *8* (8), 611-615.

[3] Shibata, N.; Seki, T.; Sánchez-Santolino, G.; Findlay, S. D.; Kohno, Y.; Matsumoto, T.; Ishikawa, R.; Ikuhara, Y., Electric field imaging of single atoms. *Nature Communications* **2017**, *8* (1), 15631.

[4] Sánchez-Santolino, G.; Lugg, N. R.; Seki, T.; Ishikawa, R.; Findlay, S. D.; Kohno, Y.; Kanitani, Y.; Tanaka, S.; Tomiya, S.; Ikuhara, Y.; Shibata, N., Probing the Internal Atomic Charge Density Distributions in Real Space. *ACS Nano* **2018**, *12* (9), 8875-8881.

[5] Lazić, I.; Bosch, E. G. T.; Lazar, S., Phase contrast STEM

for thin samples: Integrated differential phase contrast. *Ultramicroscopy* **2016**, *160*, 265-280.

[6] Sun, Y.; Abid, A. Y.; Tan, C.; Ren, C.; Li, M.; Li, N.; Chen, P.; Li, Y.; Zhang, J.; Zhong, X.; Wang, J.; Liao, M.; Liu, K.; Bai, X.; Zhou, Y.; Yu, D.; Gao, P., Subunit cell–level measurement of polarization in an individual polar vortex. *Science Advances* **2019**, *5* (11), eaav4355.

[7] Hachtel, J. A.; Idrobo, J. C.; Chi, M., Sub-Ångstrom electric field measurements on a universal detector in a scanning transmission electron microscope. *Advanced Structural and Chemical Imaging* **2018**, *4* (1), 10.

[8] Gammer, C.; Burak Ozdol, V.; Liebscher, C. H.; Minor, A. M., Diffraction contrast imaging using virtual apertures. *Ultramicroscopy* **2015**, *155*, 1-10.

[9] Ozdol, V. B.; Gammer, C.; Jin, X. G.; Ercius, P.; Ophus, C.; Ciston, J.; Minor, A. M., Strain mapping at nanometer resolution using advanced nano-beam electron diffraction. *Applied Physics Letters* **2015**, *106* (25), 253107.

[10] Shao, Y.-T.; Zuo, J.-M., Lattice-Rotation Vortex at the Charged Monoclinic Domain Boundary in a Relaxor Ferroelectric Crystal. *Physical Review Letters* **2017**, *118* (15), 157601.

[11] Panova, O.; Ophus, C.; Takacs, C. J.; Bustillo, K. C.; Balhorn, L.; Salleo, A.; Balsara, N.; Minor, A. M., Diffraction imaging of nanocrystalline structures in organic semiconductor molecular thin films. *Nature Materials* **2019**, *18* (8), 860-865.

[12] Nellist, P. D.; McCallum, B. C.; Rodenburg, J. M., Resolution beyond the 'information limit' in transmission electron microscopy. *Nature* **1995**, *374* (6523), 630-632.

[13] Jiang, Y.; Chen, Z.; Han, Y.; Deb, P.; Gao, H.; Xie, S.; Purohit, P.; Tate, M. W.; Park, J.; Gruner, S. M.; Elser, V.; Muller, D. A., Electron ptychography of 2D materials to deep sub-ångström resolution. *Nature* **2018**, *559* (7714), 343-349.

[14] Yang, H.; Rutte, R. N.; Jones, L.; Simson, M.; Sagawa, R.; Ryll, H.; Huth, M.; Pennycook, T. J.; Green, M. L. H.; Soltau, H.; Kondo, Y.; Davis, B. G.; Nellist, P. D., Simultaneous atomic-resolution electron ptychography and Z-contrast imaging of light and heavy elements in complex nanostructures. *Nature Communications* **2016**, *7* (1), 12532.

[15] Pelz, P. M.; Qiu, W. X.; Bücker, R.; Kassier, G.; Miller, R. J. D., Low-dose cryo electron ptychography via non-convex Bayesian optimization. *Scientific Reports* **2017**, *7* (1), 9883.

[16] LeBeau, J. M.; Findlay, S. D.; Allen, L. J.; Stemmer, S., Position averaged convergent beam electron diffraction: Theory and applications. *Ultramicroscopy* **2010**, *110* (2), 118-125.

[17] Xu, W.; LeBeau, J. M., A deep convolutional neural network to analyze position averaged convergent beam electron diffraction patterns. *Ultramicroscopy* **2018**, *188*, 59-69.

[18] Müller, K.; Krause, F. F.; Béché, A.; Schowalter, M.; Galioit, V.; Löffler, S.; Verbeeck, J.; Zweck, J.; Schattschneider, P.; Rosenauer, A., Atomic electric fields revealed by a quantum mechanical approach to electron picodiffraction. *Nature Communications* **2014**, *5* (1), 5653.

[19] Müller-Caspary, K.; Krause, F. F.; Grieb, T.; Löffler, S.; Schowalter, M.; Béché, A.; Galioit, V.; Marquardt, D.; Zweck, J.; Schattschneider, P.; Verbeeck, J.; Rosenauer, A., Measurement of atomic electric fields and charge densities from average momentum transfers using scanning transmission electron microscopy. *Ultramicroscopy* **2017**, *178*, 62-80.

[20] Kasai, H.; Tolborg, K.; Sist, M.; Zhang, J.; Hathwar, V. R.; Filsø, M. Ø.; Cenedese, S.; Sugimoto, K.; Overgaard, J.; Nishibori, E.; Iversen, B. B., X-ray electron density investigation of chemical bonding in van der Waals materials. *Nature Materials* **2018**, *17* (3), 249-252.

[21] Nakashima, P. N. H.; Smith, A. E.; Etheridge, J.; Muddle, B. C., The Bonding Electron Density in Aluminum. *Science* **2011**, *331* (6024), 1583-1586.

[22] Seshadri, R.; Hill, N. A., Visualizing the Role of Bi 6s “Lone Pairs” in the Off-Center Distortion in Ferromagnetic $BiMnO_3$. *Chemistry of Materials* **2001**, *13* (9), 2892-2899.

[23] Wang, J.; Neaton, J. B.; Zheng, H.; Nagarajan, V.; Ogale, S. B.; Liu, B.; Viehland, D.; Vaithyanathan, V.; Schlom, D. G.; Waghmare, U. V.; Spaldin, N. A.; Rabe, K. M.; Wuttig, M.; Ramesh, R., Epitaxial $BiFeO_3$ Multiferroic Thin Film Heterostructures. *Science* **2003**, *299* (5613), 1719-1722.

[24] Gao, W.; Addiego, C.; Wang, H.; Yan, X.; Hou, Y.; Ji, D.; Heikes, C.; Zhang, Y.; Li, L.; Huyan, H.; Blum, T.; Aoki, T.; Nie, Y.; Schlom, D. G.; Wu, R.; Pan, X., Real-space charge-density imaging with sub-ångström resolution by four-dimensional electron microscopy. *Nature* **2019**, *575* (7783), 480-484.

[25] Addiego, C.; Gao, W.; Pan, X., Thickness and defocus dependence of inter-atomic electric fields measured by scanning diffraction. *Ultramicroscopy* **2020**, *208*, 112850.

[26] Cao, M. C.; Han, Y.; Chen, Z.; Jiang, Y.; Nguyen, K. X.; Turgut, E.; Fuchs, G. D.; Muller, D. A., Theory and practice of electron diffraction from single atoms and extended objects using an EMPAD. *Microscopy* **2017**, *67* (suppl_1), i150-i161.

[27] Meyer, J. C.; Kurasch, S.; Park, H. J.; Skakalova, V.; Künzel, D.; Groß, A.; Chuvilin, A.; Algara-Siller, G.; Roth, S.; Iwasaki, T.; Starke, U.; Smet, J. H.; Kaiser, U., Experimental analysis of charge redistribution due to chemical bonding by high-resolution transmission electron microscopy. *Nature Materials* **2011**, *10* (3), 209-215.

[28] Susi, T.; Madsen, J.; Ludacka, U.; Mortensen, J. J.; Pennycook, T. J.; Lee, Z.; Kotakoski, J.; Kaiser, U.; Meyer, J. C., Efficient first principles simulation of electron scattering factors for transmission electron microscopy. *Ultramicroscopy* **2019**, *197*, 16-22.

[29] Kirkland, E. J., *Advanced Computing in Electron Microscopy*. Springer US: 2010.

[30] Doyle, P. A.; Turner, P. S., Relativistic Hartree-Fock X-ray and electron scattering factors. *Acta Crystallographica Section A* **1968**, *24* (3), 390-397.

[31] Kurasch, S.; Meyer, J. C.; Künzel, D.; Groß, A.; Kaiser, U., Simulation of bonding effects in HRTEM images of light element materials. *Beilstein Journal of Nanotechnology* **2011**, *2*, 394-404.

[32] Henkelman, G.; Arnaldsson, A.; Jónsson, H., A fast and robust algorithm for Bader decomposition of charge density. *Computational Materials Science* **2006**, *36* (3), 354-360.

[33] Bader, R. F. W., *Atoms in molecules : a quantum theory*. Clarendon Press: Oxford ;, 1990.

[34] Ohtomo, A.; Muller, D. A.; Grazul, J. L.; Hwang, H. Y., Artificial charge-modulationin atomic-scale perovskite titanate superlattices. *Nature* **2002**, *419* (6905), 378-380.

[35] Tan, H.; Verbeeck, J.; Abakumov, A.; Van Tendeloo, G., Oxidation state and chemical shift investigation in transition metal oxides by EELS. *Ultramicroscopy* **2012**, *116*, 24-33.

[36] Rojac, T.; Bencan, A.; Drazic, G.; Sakamoto, N.; Ursic, H.; Jancar, B.; Tavcar, G.; Makarovic, M.; Walker, J.; Malic, B.; Damjanovic, D., Domain-wall conduction in ferroelectric $BiFeO_3$ controlled by accumulation of charged defects. *Nature Materials* **2017**, *16* (3), 322-327.

Phase-Modulated S-RESPDOR at Ultra-Fast MAS to Measure Accurate ^{1}H-^{14}N Distances

Federica Rossi[1], Nghia Tuan Duong[1], Maria Makrinich[1], Amir Goldbourt[1],
Michele R. Chierotti[1], Roberto Gobetto[1], Yusuke Nishiyama[2]
[1] Department of Chemistry and NIS Centre, University of Torino
[2] JEOL Resonance Inc.

Here we present a recently developed solid-state NMR (SSNMR) sequence which combines a phase-modulate (PM) saturation pulse and a rotational-echo saturation-pulse double-resonance (RESPDOR) to measure accurate ^{1}H-^{14}N distances at very fast magic angle spinning (MAS) condition. Besides a deep analysis of the performances of the sequence by means of numerical simulations, we demonstrated its successful applicability to L-tyrosine·HCl and N-acetyl-L-alanine, two samples with a small and large quadrupolar constant, respectively, to probe the feasibility of the sequence to different systems. For the first time, multiple ^{1}H-^{14}N heteronuclear dipolar couplings, and thus quantitative distances, have been simultaneously and reliably extracted by fitting the experimental fraction curves with the analytical expression.

Introduction

Among the different data aimed at the structural characterization of materials, internuclear distances play a very crucial role. In particular, the measurement of H-N distances is of fundamental importance in different fields of research such as chemistry and biology and for diverse kind of samples, from peptides and proteins [1, 2] to co-crystal/salt drugs [3]. For instance, in the pharmaceutical industry when dealing with multicomponent systems formed by a drug and a second GRAS ("generally recognized as safe") molecule, the position of the hydrogen atom along N···H···O HB interactions, and thus the N-H distance, plays a key role from many points of view. It determines not only the character of the system, whether neutral (co-crystal) or ionic (salt), but also several parameters, such as solubility, stability, bioavailability, and manufacturability [4]. This is a very important subject also from the legal and regulatory point of view, connected to intellectual property issues. Solid-state NMR (SSNMR) has proved to be a valuable method for structure refinement, overcoming the major issues encountered by X-Ray diffraction technique. The latter is traditionally the most effective method for structural elucidation, but it does have restrictions of crystal dimension and poses difficulties in reliably defining proton positions. The capability of SSNMR in the structure determination relies upon the dependence of the dipolar coupling D on the inverse cubed power of the internuclear distance. Being the NMR parameter with the highest crystallographic content [5], dipolar coupling is the most exploited interaction to measure distances and get information about geometric and electronic structure of solids. Unfortunately, anisotropic interactions such as dipolar coupling and chemical shift anisotropy are averaged out by magic angle spinning (MAS) condition, which is the main employed technique to achieved high-resolution spectra in the solid state. To overcome such loss of structural information, the suppressed interactions can be selectively reintroduced by means of tailored recoupling sequences. Among those mainly used, R-symmetry schemes introduced by Levitt are the most promising and of easier design [6]. Many applications of such sequences have been presented to measure ^{1}H-^{13}C and ^{1}H-^{15}N distances at moderate and fast spinning speeds [7-9]. Besides reintroducing the ^{1}H-N heteronuclear dipolar coupling, a suitable recoupling scheme must also suppress the strong ^{1}H-^{1}H homonuclear coupling interactions to precisely determine ^{1}H-N distances. The current advanced technologies in fast MAS have eased the aforementioned requirements on recoupling techniques since, under such spinning speeds, the ^{1}H-^{1}H dipolar couplings are sufficiently averaged out. Such ultrafast MAS regime ($\nu_R \geq 60$ kHz) made possible "solution-like" indirect-detection experiments, as for example the cross-polarization with variable contact time (CP-VC) technique and its variants which provided straightforward and accurate determination of ^{1}H-^{15}N dipolar couplings and thus quantitative distances [10, 11]. The additional difficulties related to the low natural abundance of ^{15}N isotope (0.4 %), such as the low signal intensity, can be overcome by using the ^{14}N isotope with a natural abundance of 99.6%. However, being an integer quadrupolar nucleus (spin number $I = 1$), it suffers from quadrupolar interactions making the ^{1}H-^{14}N distance measurement more challenging.

›› V.P. Giuria 7, 10125, Italy | E-mail: rossi@jeol.it (She now works for JEOL ITALIA.)

To overcome the difficulty related to large quadrupolar interaction, the resonance-echo saturation-pulse double-resonance (RESPDOR) sequence was introduced, enabling ^{13}C-^{14}N distance measurements [12]. The later development of RESPDOR with the more robust SR4^2_1 recoupling sequence (S-RESPDOR) [13] instead of R$_3$ has extended its application to various systems [14-18] and more importantly allowed multiple distance measurements. Despite being widely used, the saturation of the different crystallites is not uniform but does depend on the quadrupolar constant (C_Q) and thus on the nature of the system. To achieve the same extents of saturation for the whole powder, Goldburg and coworkers have introduced an interesting phase-modulated (PM) scheme into RESPDOR sequences, which is not affected by large quadrupolar interactions [19-23]. This approach allows the determination of the distances by a simple fitting procedure between the theoretical and the experimental fraction curves, matched by adjusting only one parameter, i.e. dipolar coupling $d_{1H\text{-}14N}$.

In this work, we present the combination of PM pulse and the SR4^2_1 recoupling scheme to determine ^{1}H-^{14}N distances under ultra-fast MAS frequency of 70 kHz. As the PM-pulse has not been demonstrated at high MAS frequencies, we ran numerical simulations on a modelled ^{1}H-^{14}N spin system to investigate its practicability under such spinning condition combined with the RESPDOR scheme. Then, we examined the robustness of PM-RESPDOR sequence with respect to ^{14}N quadrupolar interaction and its application to a wide range of $d_{1H\text{-}14N}$. Finally, the method was applied to two different real samples, i.e. L-tyrosine·HCl and N-acetyl-L-alanine and the distances obtained were compared with those derived from diffraction techniques [24].

Pulse sequence

The design of the PM-S-RESPDOR sequence is similar to that of the more known dipolar-heteronuclear multiple quantum coherence (*D*-HMQC) sequence, with the difference that during t_1, a PM pulse for the saturation is used instead of a pair of single-quantum excitation and reconversion pulses. Both sequences employ the SR4^2_1 recoupling scheme to reintroduce ^{1}H-^{14}N dipolar couplings. The PM pulse, lasting for $N.t_R$, is composed by the combination of A-B-A-C-B-A-C-A blocks. Block A consists of 1 (one) pulse, lasting for $0.075{\cdot}Nt_R$ and a phase of $\varphi_0 = 225$. Block B consists of 16 (sixteen) pulses. Each lasts for $0.0109375{*}N.t_R$ with a phase of $\varphi_{i=1\text{-}16}$ = {80.5, 2.2, 245.0, 92.5, 275.7, 98.5, 330.3, 348.1, 126.3, 265.2, 349.3, 23.9, 24.1, 23.8, 92.4, 6.7}. Block C consists of 16 (sixteen) pulses. Each one lasts for $0.0109375{\cdot}Nt_R$ with a phase of $\varphi_{i=1\text{-}16}$ = {319.6, 75.6, 242.7, 95.8, 340.9, 226.5, 48.0, 38.1, 5.3, 44.4, 145.8, 303.2, 139.7, 336.7, 95.6, 341.3} (**Fig. 1**).

The method based on the PM-S-RESPDOR sequence requires the acquisition of two sets of data to extract distance information. Firstly, the experiment is run without irradiation of the PM pulse on the ^{14}N channel during a delay of $N{\cdot}t_R$. The π pulse on the ^{1}H channel refocuses the ^{1}H-^{14}N dipolar coupling and the ^{1}H CSA, whereas the incremental SR4^2_1 recoupling periods average the ^{1}H-^{1}H dipolar coupling. In this way, the decaying of ^{1}H magnetization is only due to higher-order terms of the effective Hamiltonian and not to the parameter we want to measure, resulting in the signal $S_0(\tau)$. Secondly, the identical experiment is run with the PM irradiation pulse on the ^{14}N channel. Such pulse prevents the refocusing of ^{1}H-^{14}N heteronuclear dipolar coupling which thus modulates the achieved ^{1}H signal, $S'(\tau)$. By plotting $\Delta S/S_0 = (S_0(\tau)\text{-}S'(\tau))/S_0(\tau)$ as a function of τ, the decaying effects are minimized. The curve is then matched with the theoretical one and the $d_{1H\text{-}14N}$ is extracted to obtain accurate distances, according to the equation:

$$^1\mathrm{H}{-}^{14}\mathrm{N}\ \mathrm{distance}\ \left(\mathring{A}\right) = \left(\frac{120.1}{b_{1\mathrm{H}-14\mathrm{N}}/2\pi(\mathrm{kHz})}\frac{\gamma_{14\mathrm{N}}}{\gamma_{1\mathrm{H}}}\right)^{1/3}$$

where γ_X (X = ^{1}H or ^{14}N) represents the gyromagnetic ratio of the X nucleus.

Numerical simulations

Different numerical simulations were carried out using the SIMPSON package on an isolated ^{1}H-^{14}N spin system to analyze the new sequence in terms of applicability. First of all,

Fig. 1

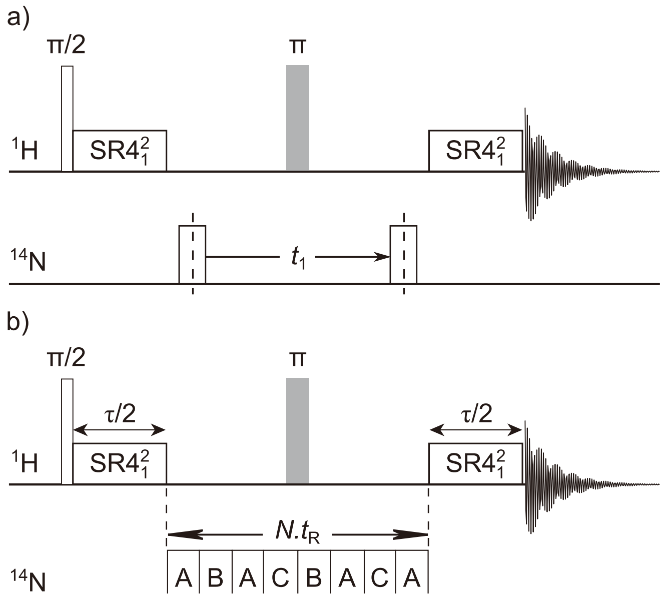

a) ^{1}H-^{14}N *D*-HMQC sequence. The second dimension is achieved by incrementing t_1. b) ^{1}H-^{14}N PM-S-RESPDOR sequence. The fraction curve is obtained by incrementing the total mixing time (τ) of the SR4^2_1 blocks in absence and presence of ^{14}N irradiation. The PM pulse is the combination of A-B-A-C-B-A-C-A blocks. Nt_R represents the pulse length of the PM pulse, N is an integer and t_R is the length of the rotor period. The interval between these two blocks should be kept rotor-synchronized for both *D*-HMQC and PM-S-RESPDOR sequences. Reproduced with permission from ref [26].

its feasibility at very fast MAS spinning speeds ($\nu_R \geq 70$ kHz) was tested by changing the MAS frequencies from 20 to 70 kHz and keeping unchanged the dipolar coupling value ($|b_{1H\text{-}14N}/(2\pi)| = 2$ kHz) for the modelled system under investigation. The obtained fraction curves are displayed in **Fig. 2** together with the analytical one (unfilled circles).

It is possible to observe that all the curves are similar to each other and that they reach the theoretical maximum of $\Delta S/S_0 = 2I/(2I+1) \sim 0.67$ at the same mixing time ($\tau = 1.6$ ms), meaning that only the first-order averaged Hamiltonian is involved in their behavior. These data confirm the possibility of this sequence to be employed at fast MAS regime. Moreover, by focusing the attention on the initial part of the curves, it can be noticed that the $\Delta S/S_0$ intensities at $\tau = 0$ ms are not equal to zero, as it would be expected. This is probably caused by the reintroduction of ^{1}H-^{14}N dipolar coupling during the PM pulse ascribed to higher order effects, which become more significant as the MAS speed decreases. Hence, not only the sequence can be applied at 70 kHz, but such frequency is also preferred, given its ability in minimizing the effects of high-order terms of ^{1}H-^{14}N dipolar interaction.

The high-order contribution described above is also observed in the second set of numerical simulations which aimed at the analysis of the effects of ^{14}N radio-frequency fields (ν_1). In the PM-S-RESPDOR sequence, in fact, the uniform and efficient saturation of ^{14}N nucleus is fundamental. The simulations were performed with $|b_{1H\text{-}14N}/(2\pi)| = 2$ kHz, PM pulse length of 10 t_R and by fixing a quadrupolar constant C_q of 4 MHz, being it a common value for most organic molecules. The experimental fraction curves obtained by varying the ν_1 (^{14}N) from 10 to 100 kHz and the analytical fraction curve are shown in **Fig. 3** and, as in the previous case, they all reach the theoretical maximum at the same mixing time. Still, the radio-frequency field of 80 kHz is the one that shows the best performances in terms of efficiency of saturation and minimization of high-term effects, which would negatively affect the accuracy of the fittings.

Fig. 2

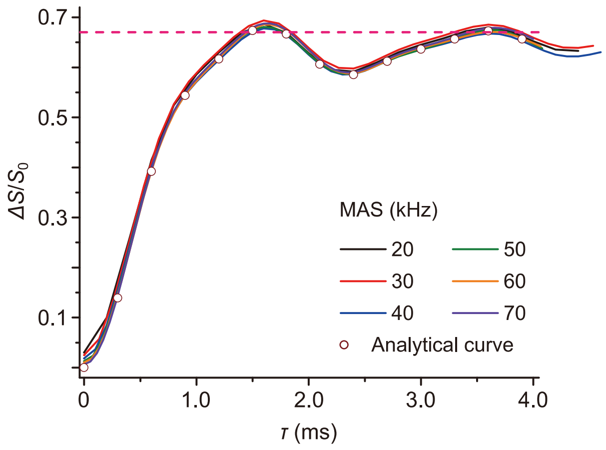

Simulated PM-S-RESPDOR fraction curves (solid lines) with $\Delta S/S_0$ intensities plotted as a function of τ for a powdered sample. The parameters used for the isolated ^{1}H-^{14}N spin system are the followings: $|b_{1H\text{-}14N}/(2\pi)| = 2.0$ kHz, ^{14}N C_Q of 1.0 MHz, $B_0 = 14.1$ T, MAS frequencies ranging from 20 to 70 kHz. The analytical curve (unfilled circle) is plotted with $|b_{1H\text{-}14N}/(2\pi)|$ of 2.0 kHz for comparison. The dash line represents the $\Delta S/S_0$ value of 0.67. Reproduced with permission from ref [26].

Lastly, by keeping unchanged all the optimum conditions found with the previous numerical simulations, the effect of different quadrupolar constant values was examined. Indeed, the ^{14}N C_q can extensively change in different systems and large values could hamper the saturation of ^{14}N nuclei and thus the RESPDOR efficiency. By comparing the experimental fraction curves obtained with C_q from 1.0 to 6.0 MHz (**Fig. 4**), it is possible to note that even if reaching the maximum at the same mixing time, they slightly deviate from each other and that the larger the C_q, the larger is the difference with respect to the analytical curve.

Fig. 3

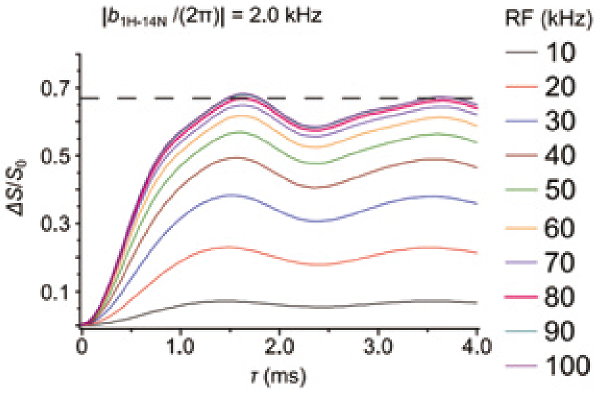

Simulated PM-S-RESPDOR fraction curves (solid lines) with $\Delta S/S_0$ intensities plotted as a function of τ for a powdered sample. The parameters used for the isolated ^{1}H-^{14}N spin system are the followings: $|b_{1H\text{-}14N}/(2\pi)| = 2.0$ kHz, ^{14}N C_Q of 4.0 MHz, $B_0 = 14.1$ T and $\nu_R = 70$ kHz. The PM pulse length is $10t_R$ (0.14 ms) while ν_1(^{14}N) has been varied from 10 to 100 kHz with steps of 10 kHz. The dash line represents the $\Delta S/S_0$ value of 0.67. Readapted from Fig. 3 of ref [26].

Fig. 4

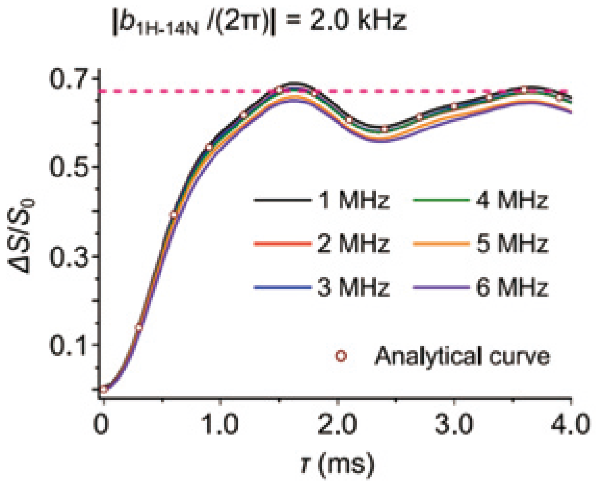

Simulated PM-S-RESPDOR fraction curves (solid lines) with $\Delta S/S_0$ intensities plotted as a function of τ for a powdered sample. The parameters used for the isolated ^{1}H-^{14}N spin system are the followings: $|b_{1H\text{-}14N}/(2\pi)| = 2.0$ kHz, ^{14}N C_Q has been varied from 1.0 to 6.0 MHz, $B_0 = 14.1$ T and $\nu_R = 70$ kHz. The PM pulse length and ν_1 is $10t_R$ (0.14 ms) and 83 kHz, respectively. The analytical curve (unfilled circle) is also included for comparison. The dash line represents the $\Delta S/S_0$ value of 0.67. Readapted from Fig. 3 of ref [26].

However, it is important to point out that such deviations are not significant and the PM-S-RESPDOR sequence could be devised as robust towards ^{14}N quadrupolar interactions under MAS of 70 kHz.

The following experiments, which show the application of the sequence to two model samples, were performed employing the optimum conditions discussed above, i.e. length of PM pulse of $10t_R$ and ^{14}N rf field of 83 kHz.

Experimental results

By using a JEOL JNM-ECZ600R spectrometer, the sequence was first applied to a simple system, i.e. L-tyrosine·HCl (inset in **Fig. 5**), in which the highly symmetric NH_3^+ group shows a small quadrupolar constant (approximately 1.0 MHz). Prior to the application of PM-S-RESPDOR, *D*-HMQC experiment (Fig. 5) was performed to unambiguously assign the ^1H chemical shift of the three protons at 7.7 ppm.

The results obtained from the application of the sequence on the ^1H signal of NH_3^+ are shown in **Fig. 6** together with the related errors of $\Delta S/S_0$ intensities displayed as vertical bars.

The fraction curve reaches the maximum intensity at $\tau \sim$ 1.4 ms, whereas after that, the curve shows a large fluctuation due to low signal-to-noise ratio. Hence, those points are not reliable and are not taken into account for the extraction of the dipolar coupling. The obtained $|b_{1H\text{-}14N}/(2\pi)|$ value extracted from the best fitting of the experimental fraction curve with the analytical expression corresponds to a ^1H-^{14}N distance of 1.68 Å ± 0.04 Å. This value is significantly longer than the H-N distance of 1.01 Å, determined by neutron diffraction technique (CDS entry: LTYRHC10) [25]. Such disagreement is due to the dynamic averaging of the distance caused by the fast rotation of the three protons along the C-N bond. By correcting the original distance with a modulation factor, we obtain:

(Original $d_{H\text{-}N}$) = (Averaged $d_{H\text{-}N}$)$\cdot|P_2(\cos(109.5^{\circ}))^{1/3}|$=1.68 Å $\cdot|P_2(\cos(109.5^{\circ}))^{1/3}|$=1.16 Å

The value of 1.16 Å is now perfectly agreeing with the real value and demonstrates how the sequence can be easily and accurately used to measure H-N distances.

To further explore the potentialities of the method, the sequence was applied to a second model sample, i.e. N-acetyl-L-alanine (structure in **Fig. 7**), with a larger ^{14}N quadrupolar constant. From the matching between the experimental fraction curve of the ^1H signal at 7.9 ppm (NH group) and the analytical one, a H-N distance of 1.06 Å ± 0.02 Å was found (Fig. 7).

Also in this case, the distance perfectly agrees with a reference value of 1.0 Å found from a CSD survey on neutron diffraction data collected for similar systems. It is to be noted that the fitting was performed only up to mixing time of 0.4 ms, as for longer τ large uncertainties are observed. Such behaviour is the same already observed for the previous sample, in which the signal-to-noise-ratio was too low to make the intensities reliable. The main cause of such spinning fluctuations is probably the reintroduced ^1H-^{14}N dipolar interaction which prevents the echo formation of ^1H signals. Preliminary investigations on such phenomenon have already carried out and showed it does not affect the measurements, under the conditions used in our work.

Conclusions

In this work we successfully combined a phase-modulated pulse and the S-RESPDOR experiment in a novel sequence called PM-S-RESPDOR able to accurately measure ^1H-^{14}N distances at very fast MAS frequencies. Numerical simulations were fundamental in examining the applicability, performances and robustness of the sequence which resulted suitable for both high spinning speeds and large variations of dipolar and quadrupolar coupling constants. The sequence has shown the ability to measure multiple distances by a simple fitting procedure which involves the adjustment of only the ^1H-^{14}N dipolar coupling strength. The method was experimentally proved by its application to L-tyrosine·HCl and N-acetyl-

Fig.5

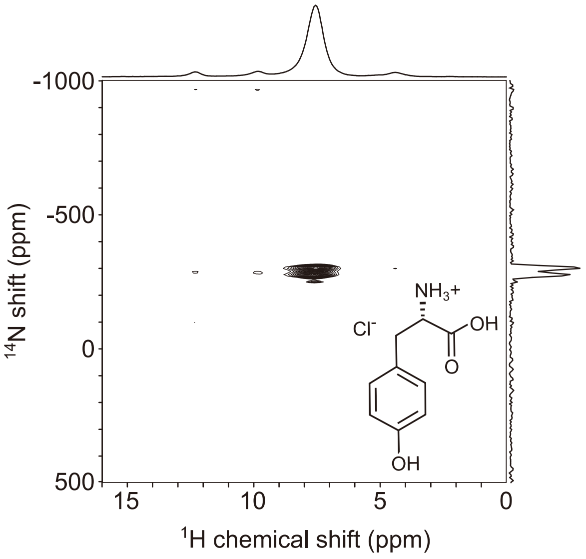

2D ^1H-{^{14}N} *D*-HMQC spectrum of Tyr (inset) with ^1H-^{14}N correlations. The experiment was run with 24 scans, 72 t_1 points, and rotor-synchronized t_1 increment of 14.3 μs. The τ and recycle delay were 400 μs and 3.5 s, respectively. The experimental time was ~ 3.4 hours. Reproduced with permission from ref [26].

Fig. 6

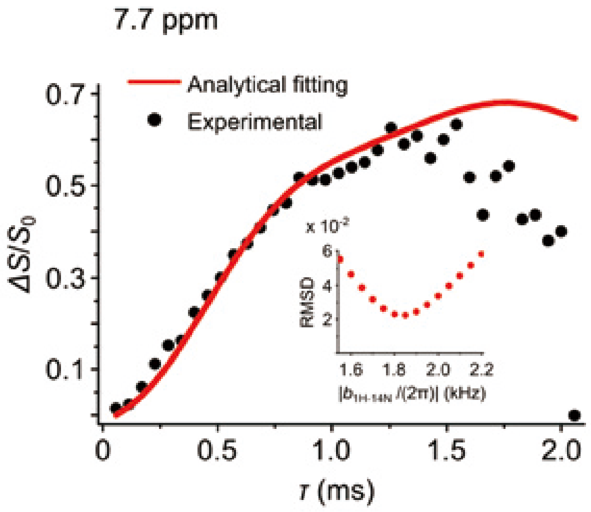

Tyr: the experimental ^1H-^{14}N fraction curves at ^1H chemical shift of 7.7 ppm achieved by PM-S-RESPDOR (dots) and the fitting curves by the analytical expression (solid lines). The experimental time was ~ 6 hours. The insets show the best fitting ^1H-^{14}N dipolar coupling values based on the RMSD analysis. Fittings are performed solely by adjusting $b_{1H\text{-}14N}/(2\pi)$. Readapted from Fig. 6 of ref [26].

Fig. 7

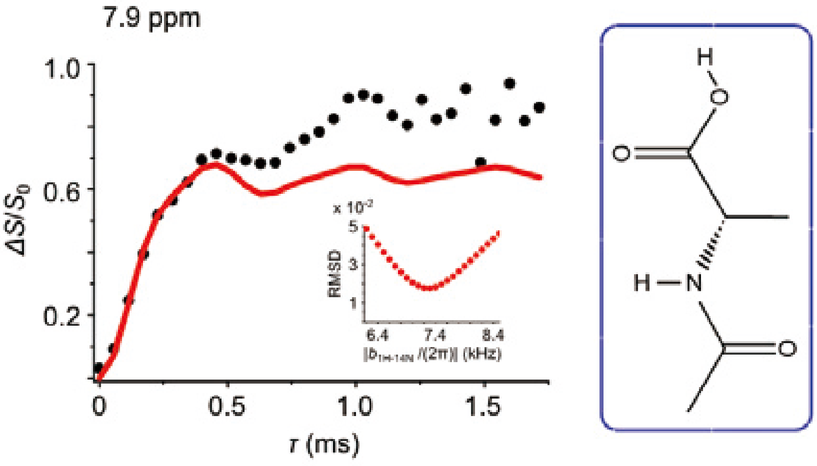

AcAla: the experimental ^{1}H-^{14}N fraction curves at ^{1}H chemical shift of 7.9 ppm achieved by PM-S-RESPDOR (dots) and the fitting curves by the analytical expression (solid lines). The experimental time was ~ 20 hours. The insets show the best fitting ^{1}H-^{14}N dipolar coupling values based on the RMSD analysis. Fittings are performed solely by adjusting $b_{1H\text{-}14N}/(2\pi)$. Readapted from Fig. 6 of ref [26].

L-alanine samples for which distances consistent with the literature values were found. The sequence represents a significant improvement for such measurements and can be applied to other systems and quadrupolar nuclei. Recently some of us published an interesting example of application of the ^{1}H−^{14}N PM-S-RESPDOR for the evaluation of N−H distances in the case of salt/cocrystal polymorphism involving an adduct between ethionamide and salicylic acid [27]. In this real case this technique provided for the main N···H···O interaction N−H distances of 1.07 Å for the salt and of 1.50 Å for the co-crystal in remarkable agreement with those derived by DFT optimized X-ray diffraction.

References

[1] C. M. Rienstra, L. Tucker-Kellogg, C. P. Jaroniec, M. Hohwy, B. Reif, M. T. McMahon, B. Tidor, T. Lozano-Pérez and R. G. Griffin, *Proc. Natl. Acad. Sci*., 2002, **99**, 10260−10265.
[2] W. T. Franks, B. J. Wylie, H. L. F. Schmidt, A. J. Nieuwkoop, R.-M. Mayrhofer, G. J. Shah, D. T. Graesser and C. M. Rienstra, *Proc. Natl. Acad. Sci*., 2008, **105**, 4621−4626.
[3] L. Rajput, M. Banik, J. R. Yarava, S. Joseph, M. K. Pandey, Y. Nishiyama and G. R. Desiraju, *IUCrJ*, 2017, **4**, 466−475.
[4] P. Cerreia Vioglio, M.R. Chierotti, R. Gobetto, *Adv. Drug Delivery Rev*., 2017, **117**, 86-110.
[5] M. R. Chierotti and R. Gobetto, *CrystEngComm*, 2013, **15**, 8599−8612.
[6] M. H. Levitt, in *Encyclopedia of Nuclear Magnetic Resonance. Volume 9, Advances in NMR*, eds. D. M. Grant and R. K. Harris, Wiley, 2002, pp. 165–196.
[7] G. Hou, I. J. L. Byeon, J. Ahn, A. M. Gronenborn and T. Polenova, *J. Am. Chem. Soc*., 2011, **133**, 18646−18655.
[8] G. Hou, X. Lu, A. J. Vega and T. Polenova, *J. Chem. Phys*., 2014, **141**, 104202.
[9] X. Lu, H. Zhang, M. Lu, A. J. Vega, G. Hou and T. Polenova, *Phys. Chem. Chem. Phys. PCCP*, 2016, **18**, 1–10.
[10] P. Paluch, T. Pawlak, J. P. Amoureux and M. J. Potrzebowski, *J. Magn. Reson*., 2013, **233**, 56–63.
[11] Y. Nishiyama, M. Malon, M. J. Potrzebowski, P. Paluch and J. P. Amoureux, *Solid State Nucl. Magn. Reson*., 2015, **73**, 1–7.
[12] Z. Gan, *Chem. Commun*., 2006, 4712–4714.
[13] T. G. Oas, R. G. Griffin and M. H. Levitt, *J. Chem. Phys*., 1988, **89**, 692–695.
[14] A. Brinkmann and A. P. M. Kentgens, *J. Am. Chem. Soc*., 2006, **128**, 14758–14759.
[15] L. Chen, X. Lu, Q. Wang, O. Lafon, J. Trébosc, F. Deng and J. P. Amoureux, *J. Magn. Reson*., 2010, **206**, 269–273.
[16] L. Chen, Q. Wang, B. Hu, O. Lafon, J. Trébosc, F. Deng and J. P. Amoureux, *Phys. Chem. Chem. Phys*., 2010, **12**, 9395–9405.
[17] X. Lu, O. Lafon, J. Trébosc and J. P. Amoureux, *J. Magn. Reson*., 2011, **215**, 34–49.
[18] F. Pourpoint, J. Trébosc, R. M. Gauvin, Q. Wang, O. Lafon, F. Deng and J. P. Amoureux, *ChemPhysChem*, 2012, **13**, 3605–3615.
[19] T. Gullion and J. Schaefer, *J. Magn. Reson. 1969*, 1989, **81**, 196–200.
[20] E. Nimerovsky, R. Gupta, J. Yehl, M. Li, T. Polenova and A. Goldbourt, *J. Magn. Reson*., 2014, **244**, 107–113.
[21] E. Nimerovsky, M. Makrinich and A. Goldbourt, *J. Chem. Phys*., DOI:10.1063/1.4978472.
[22] M. Makrinich, R. Gupta, T. Polenova and A. Goldbourt, *Solid State Nucl. Magn. Reson*., 2017, **84**, 196–203.
[23] M. Makrinich, E. Nimerovsky and A. Goldbourt, *Solid State Nucl. Magn. Reson*., 2018, **92**, 19–24.
[24] N. T. Duong, F. Rossi, M. Makrinich, A. Goldbourt, M.R.Chierotti, R. Gobetto, Y. Nishiyama, *J. Magn. Res*., 2019, **308**, 106559.
[25] M. N. Frey, T. F. Koetzle, M. S. Lehmann and W. C. Hamilton, *J. Chem. Phys*., 1973, **58**, 2547–2556.
[26] N. Tuan Duong, F. Rossi, M. Makrinich, A. Goldbourt, M. R. Chierotti, R. Gobetto, Y. Nishiyama, *J. Magn. Res*., 2019, **308**, 106559.
[27] D. Bernasconi, S. Bordignon, F. Rossi, E. Priola, C. Nervi, R. Gobetto, D. Voinovich, D. Hasa, N.T. Duong, Y. Nishiyama, M.R. Chierotti, *Cryst Growth Des*., 2020, **20**, 2, 906-915.

Electrostatic Potential Imaging of Organic Materials using Differential Phase Contrast Scanning Transmission Electron Microscopy

Shin Inamoto, Akiyo Yoshida, Akihiro Masuda, and Yuji Otsuka
Morphological Research Laboratory, Toray Research Center, Inc.

In 1965, at the Central Research Laboratories in Toyo Rayon Company, Ltd., the predecessor of Toray Research Center, Inc., the electron staining method was applied to organic materials for the first time in the world. Even now, more than half a century later, electron staining is an important technique for transmission electron microscopy (TEM) observations of organic materials. However, the electron staining method has certain drawbacks, such as the possibility of deterioration in the original structure of samples. To overcome these problems, we considered applying electrostatic potential imaging based on differential phase contrast (DPC) scanning transmission electron microscopy (STEM) to organic materials. By applying this imaging technique to various organic materials, it was found that the image contrast between different materials was significantly improved compared to the conventional TEM method. This paper introduces the electrostatic potential images of unstained organic materials, which are difficult to visualize using the conventional TEM.

Introduction

Currently, various polymer materials, such as polyethylene (PE), polypropylene (PP), and polystyrene (PS), are widely used. Polymer materials have the ability to achieve high functionality by synthesizing two or more polymers. For example, polymer alloys manufactured by combining high-strength resin and flexible rubber have both strength and impact resistance. A typical example of a polymer alloy is acrylonitrile-butadiene-styrene (ABS) resin. ABS resin is known to form a phase-separated structure composed of sea phases of acrylonitrile-styrene copolymer (AS) and island phases of butadiene rubber (B). As polymer alloys often form small domain structures, transmission electron microscopy (TEM) is suitable for structural analysis. However, since organic materials show low electron scattering contrast, it is difficult to observe the phase-separated structure using conventional TEM. Typically, in TEM imaging of organic materials, the electron staining method is used to enhance the electron scattering contrast [1, 2]. **Figure 1** shows the TEM image of ABS resin. The upper part of the TEM image is an unstained region. Although titan-oxide particles of the inorganic filler contained in the resin can be observed, the phase-separated structures of the AS and the B phases are not visible. Conversely, the lower part of the TEM image is an electron-stained area using osmium tetroxide (OsO_4). Because the B phases are selectively stained by OsO_4, the scattering cross section for electrons increases in the B phases. Accordingly, the B phase shows a dark contrast. As a result, the phase-separated structures of the AS and B phases are clearly visualized. Hence, electron staining is an important technique for TEM observation of polymer materials.

Fig. 1 TEM image of ABS resin.

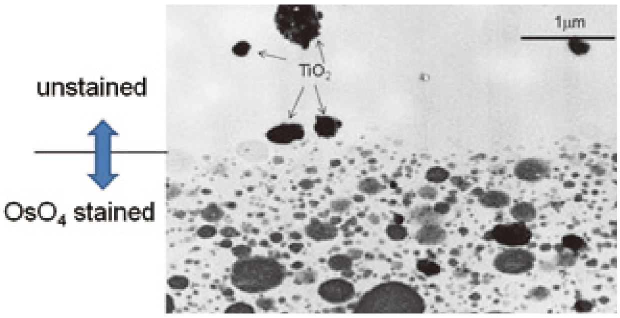

The upper and lower parts of the TEM image are unstained and the OsO_4 electron-stained area, respectively. Because osmium selectively penetrates the B phase, the B phases of 50–500 nm in size are visible. Titan-oxide particles of the inorganic filler are contained in the ABS resin, which are black in the TEM image.

However, electron staining has several drawbacks. To begin with, electron staining is not applicable to all organic materials, and there are limited applicable combinations. Furthermore, the stainability is drastically different even between similar materials with slightly different chemical structures. This means that it takes a considerable amount of time to find the optimal electron staining conditions. Another major problem is that by penetrating heavy metal into the polymer, there is a high possibility that

›› 3-7, Sonoyama 3-chome, Otsu, Shiga, 520-8567, Japan | E-mail: Shin_Inamoto@trc.toray.co.jp

expansion of each phase and breaking / crosslinking of molecular chains are induced. Because there are no methods to easily check whether such deformations are induced, such concerns are always present when applying electron staining. Therefore, to visualize the original structure of organic materials, an observation method without electron staining is required.

Electrostatic Potential Imaging via Differential Phase Contrast Scanning Transmission Electron Microscopy

In this study, we utilized differential phase contrast (DPC) scanning transmission electron microscopy (STEM) as an imaging technique for organic materials without electron staining. DPC STEM is mainly used to visualize the electromagnetic field inside the specimens. When incident electrons pass through a specimen having an electromagnetic field, they are deflected by the Coulomb or Lorentz force. By detecting the deflected electrons with an azimuthally segmented detector, the amount and direction of the deflection can be calculated. Based on this information, the electromagnetic field inside the specimen can be visualized. DPC STEM was first proposed by Dekkers and de Lang in 1974 [3]. They used two half-split detectors and discussed the one-dimensional phase contrast transfer functions (PCTFs) of DPC images. To extend DPC imaging into two dimensions, Rose proposed a quadrant-segmented detector [4]. Recently, the University of Tokyo and JEOL co-developed a high-sensitivity and high-speed segmented detector. Thus, DPC STEM has once again attracted much attention [5-8]. The DPC STEM has been applied for visualizing the electric field at the p-n junction in semiconductor materials [8] and magnetic fields in magnetic materials [9-13]. Moreover, as electrostatic potentials are dependent on individual materials, in principle, a weak electric field derived from the difference between the electrostatic potential should be induced at the interface between different materials. If the weak electric field induced at the interface of the polymer alloy is detectable, there is a possibility that the phase-separated structure of the polymer alloy can be visualized.

The information directly obtained by DPC STEM is the electric field vector at each scanning point. According to the Poisson equation and Gauss's law, the electrostatic potential $\phi(\vec{r})$, electric field $\vec{E}(\vec{r})$, and charge density $\phi(\vec{r})$ are connected as

$$\nabla^2\phi(\vec{r}) = -\vec{\nabla}\cdot\vec{E}(\vec{r}) = -\frac{1}{\varepsilon_0}\rho(\vec{r}), \qquad (1)$$

where $\vec{r}$ is the real space coordinate and ε_0 is the permittivity of vacuum. Eq. (1) implies that the electrostatic potential can be obtained through the integration of an electric field. The electrostatic potential is linearly correlated with phase contrast in the case of thin samples [14]. Since phase contrast is sensitive to light elements [15], the imaging technique could be effective for organic materials. In this study, the results of electrostatic potential imaging via DPC STEM for various organic materials are introduced.

Experimental Methods

A transmission electron microscope (JEM-ARM200F, JEOL) equipped with an aberration corrector for probe-forming systems (CESCOR, CEOS) and a segmented annular all field detector (SAAF Octa, JEOL) was used for the analysis. All observations were performed at an accelerating voltage of 200 kV. Electrostatic potential integrations were performed using a commercial software program (qDPC, HREM Research Inc.) [16].

Visualization of phase-separated structure in ABS resin

As ABS resin has a well-known structure, it is used to confirm the image contrast in DPC STEM images. A commercially available plate-shaped black ABS resin was used as the sample. Since unstained ABS resin is very soft, cryo-thinning is essential for preparing the TEM samples. The thinning method using the cryo-ultramicrotome method and the cryo-focused ion beam (FIB) method were investigated. As shown in **Figs. 2**(a) and 2(b), the sample thinned by the cryo-ultramicrotome method has wrinkles due to physical contact with a diamond knife. Because DPC STEM is highly sensitive to the differences in local sample thickness, such as the wrinkles and small scratches on the sample surface that are not observed by conventional TEM, it is difficult to detect the weak electric field from such samples. Thus, the samples are not suitable for DPC STEM measurements. In contrast, the sample thinned by the cryo-FIB method has no wrinkles, as shown in Figs. 2(c) and 2(d). Therefore, the cryo-FIB method was used for the ABS resin sample preparation so that it could be observed with the DPC STEM.

Figure 3(a) shows a high-angle annular dark field (HAADF)-STEM image of the ABS resin thinned by the cryo-FIB method. To improve strength and heat resistance, filler particles are often incorporated into commercially available ABS resins. Consequently, in this sample, filler particles showing a white contrast are observed inside the ABS resin. In the HAADF-STEM image, the phase-separated structure of the AS and B phases as observed in Fig. 1 are not visible. Conversely, Fig. 3(b) shows an electric field strength image obtained via DPC STEM of the same field of view as Fig. 3(a). As indicated by the arrows, circular-shaped patterns are clearly observed in the electric field strength image. The patterns indicate the positions of the interface between the AS and B phases. Judging from the shape of each phase in the electron-stained TEM image shown in Fig. 1, the circular domains correspond to the B phases. The electrostatic potential image calculated from the electric field strength image in Fig. 3(b) is shown in Fig. 3(c). Circular B phases that are not distinguishable in the HAADF-STEM image are visualized in the electrostatic potential image. Thus, the phase-separated structure between the

Fig. 2

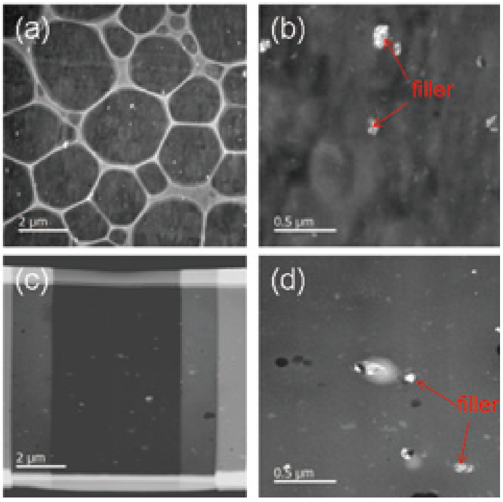

(a)(b) Low- and high-magnification HAADF-STEM images of unstained ABS resin thinned by cryo-ultramicrotome method. Wrinkles in the thin film are induced by physical contact with a diamond knife. (c)(d) Low- and high-magnification HAADF-STEM images of unstained ABS resin thinned by cryo-FIB method. There are no wrinkles in this sample.

Fig. 3

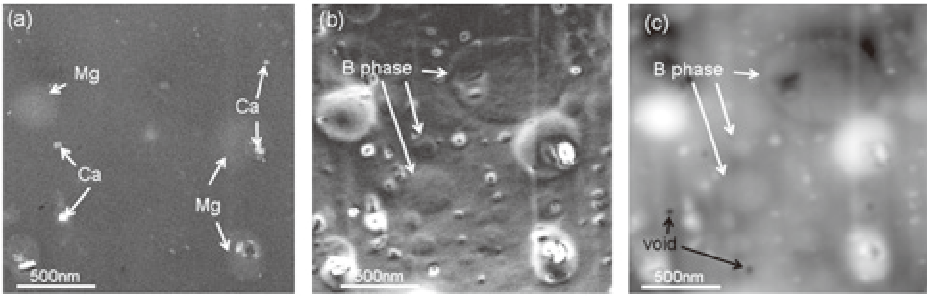

(a) HAADF-STEM image, (b) electric field strength image, and (c) electrostatic potential image of unstained ABS resin. The phase-separated structure between the AS and B phases that cannot be discerned in the HAADF-STEM image is visualized in the electrostatic potential image.

AS and B phases of the unstained ABS resin has been successfully observed by electrostatic potential imaging. Moreover, compared with the HAADF-STEM image, the contrast between the filler particles and the voids is significantly enhanced. As voids inside the polymer show low scattering contrast in conventional TEM or STEM images, electrostatic potential imaging is effective for the observation of such small voids.

Visualization of bulk hetero structure in active layer of organic photovoltaics

Organic photovoltaic (OPV) devices have many advantages, such as their light weight and mechanical flexibility, which enable them to be mounted on walls, windows, and clothes [17-19]. Accordingly, OPV devices are expected to create new photovoltaic market opportunities. The active layer in OPV devices comprises a mixed layer of donor and acceptor, which are both organic materials. To operate OPV devices, it is necessary to convert excitons generated by sunlight in the active layer into free carriers at the interface between the donor and acceptor. Since the exciton diffusion distance is approximately 10 nm in the active layer, small donor and acceptor domains are preferred [20]. The bulk heterojunction (BHJ) is a promising structure for high-efficiency OPV devices as the phase-separated morphology of the donor and acceptor within the nanometer scale is formed. Moreover, controlling the BHJ morphology is possible by a thermal annealing process [21, 22]. In this study, we have prepared the active layer based on poly(3-hexylthiophene) (P3HT) as the donor and [6,6]-phenyl-C61-butyric acid methyl ester (PCBM) as the acceptor, which is one of the most common systems, and we analyzed the BHJ structure by electrostatic potential imaging via DPC STEM [23].

P3HT and PCBM were dissolved in chloroform with a weight ratio of 1:1. The solution was spin-coated at 1500 rpm for 30 s on a glass substrate. This spin-coating condition produces a thin film approximately 100 nm in thickness. After dropping deionized water onto the spin-coated glass substrate, small pieces of the spin-coated film were scratched off using a needle. The small pieces floating on the water droplet were collected onto collodion film-coated copper TEM grids. **Figure 4**(a) shows a BF-STEM image of the P3HT–PCBM thin film. The phase-separated structure of the donor and acceptor is not visualized in the BF-STEM image as the image contrast between P3HT and PCBM is indistinguishable. However, in the electrostatic potential image shown in Fig. 4(b), a particle-like structure is observed. Judging from the height of the electrostatic potential, the black and white domains correspond to the donor and the acceptor, respectively. In the high-magnification electrostatic potential image shown in Fig. 4(c), it is evident that the size of each domain is approximately 10 to 20 nm, and both domains form a co-continuous-like structure. Thus, the electrostatic potential imaging can visualize the phase-separated structure in the P3HT–PCBM blend, which is impossible to distinguish by conventional TEM/STEM. Additionally, to investigate the annealing behavior of the phase-separated structure, the sample was annealed at 150 °C for 10 min in air and analyzed by electrostatic potential imaging. Figure 4(d) shows an electrostatic potential image of the annealed sample. Compared to the sample before annealing, the size of each domain increases. Moreover, some black domains that correspond to P3HT phases become line-shaped. Similar shape domains are formed in pure P3HT polymer, which were observed using atomic force microscopy (AFM) [24]. Hence, it can be concluded that the line-shape domains are derived from an edge-on packing structure (P3HT with a planar structure is vertically oriented to a substrate). Additionally, in this study, P3HT domains possibly form the edge-on packing. Thus, the BHJ structure of the OPV active layer can be analyzed in detail by electrostatic potential imaging. We believe that this information is useful for improving the OPV power conversion efficiency.

Fig. 4

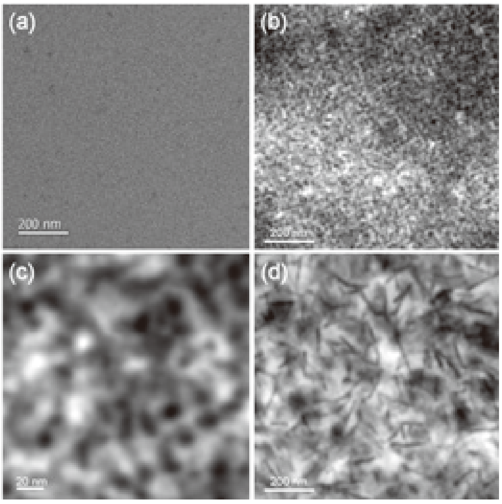

(a) BF-STEM image and (b) electrostatic potential image of the P3HT–PCBM thin film. The BF-STEM image shows flat image intensity, whereas a particle-like structure is observed in the electrostatic potential image. (c) High-magnification electrostatic potential image. The size of each domain is approximately 10–20 nm. (d) Electrostatic potential image of the annealed sample. The size of each domain increases after annealing when compared to the sizes before annealing. Some black domains, which correspond to the P3HT phases, become line-shaped.

Identification of carbon particles and ionomers in fuel cell electrode layer

Generally, catalyst metal particles of several nanometers supported on carbon particles of several 100 nm and gel ionomers for proton conduction are used as composite materials of the catalyst layer in polymer electrolyte fuel cells (PEFCs) [25, 26].

The morphology of the three-phase interface of the ionomer-carbon-catalyst plays a role in PEFC performance improvement or degradation. Therefore, a precise analysis of the morphology is essential for manufacturing high-performance PEFCs. However, it is difficult to distinguish carbon particles and ionomers in conventional TEM imaging, because the difference in electron scattering contrast is low. To overcome this problem, electron staining by means of ruthenium tetroxide (RuO_4) is used to provide high contrast, where the ionomer region is selectively stained by RuO_4. However, after electron staining, the resistance to electron beam irradiation clearly increases. This means that the chemical bonding state may change during the electron staining process. In this study, we have investigated whether the image contrast between carbon particles and ionomers appeared without electron staining using electrostatic potential imaging.

The catalyst layer in commercially available PEFC was thinned by an ultramicrotome method. The ultra-thin section supported on a TEM grid was used for TEM observations. **Figure 5**(a) shows a BF-STEM image of the catalyst layer. The particles of approximately 2 to 10 nm in size showing a black contrast in the image are platinum catalyst particles. In the high-magnification BF-STEM image shown in Fig. 5(b), it is possible to distinguish between the ionomers and the carbon particles because ionomers have an amorphous structure, whereas carbon particles have weak crystallinity. Contrastingly, in the HAADF-STEM image shown in Fig. 5(c), it is impossible to distinguish them because the granular contrast derived from amorphous structures is not visible, as can be observed in the BF-STEM images. Figure 5(d) shows an electrostatic potential image of the same field of view as Figs. 5(a) and 5(c). The image intensity in the carbon particle region is higher than that in the ionomer region. Accordingly, the carbon particles and the ionomers can be distinguished in the electrostatic potential image. In reality, as the electrostatic potential image strongly reflects the influence of the sample thickness in the observation direction, it is impossible to discuss the extent to which the image contrast of this sample with a non-uniform thickness is enhanced. However, compared to the BF-STEM and HAADF-STEM images, it is evident that the image contrast between the carbon particles and the ionomers has definitely increased. To analyze this in further detail and obtain quantitative information on the three-phase interface, it is necessary to perform three-dimensional analysis using electron tomography based on electrostatic potential images, as shown in Fig. 5(d). We have already successfully performed DPC STEM tomography measurements on ABS resin [27]. It is expected that precise quantitative information on the three-phase interface in PEFCs can be obtained by DPC STEM tomography.

Observation of internal structure of nylon/elastomer alloy

The aforementioned electrostatic potential images were used to visualize the structures that had no image contrast in conventional TEM images. Additionally, this imaging is also effective for the precise analysis of structures that are visualized even in the conventional TEM images.

Figure 6(a) shows a HAADF-STEM image of the nylon/elastomer alloy. Since this sample is relatively hard even without electron staining, a thin sample with a uniform thickness can be produced by the ultramicrotome method at room temperature. In the HAADF-STEM image shown in Fig. 6(a), the phase-separated structure of nylon and elastomer is visualized even though electron staining is not applied. Judging from the shape of each phase, the black sea and the white island phases are nylon and elastomer, respectively. In the high-magnification HAADF-STEM image shown in Fig. 6(b), small black phases, approximately 100 to 200 nm in size, are observed inside the elastomer island phase. This indicates that small nylon phases are formed inside the elastomer island phases. Figures 6(c) and 6(d) show electrostatic potential images of the same field of view shown in Figs. 6(a) and 6(b). In these electrostatic potential images, the phase-separated structure can be observed with greater clarity than that in the HAADF-STEM images. Accordingly, it is possible to confirm the existence of small

Fig. 5

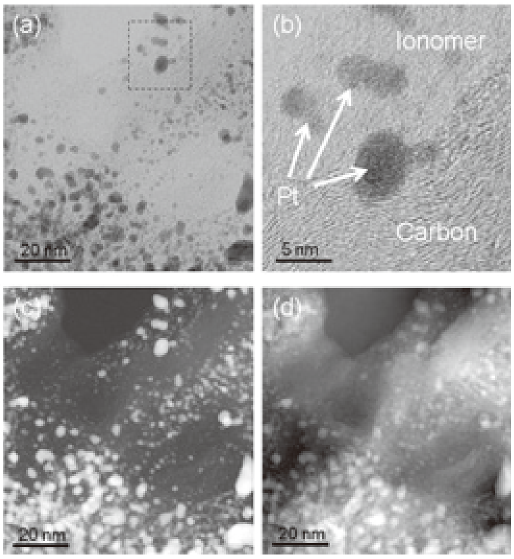

(a) BF-STEM image of the catalyst layer. The particles approximately 2–10 nm in size, with a black contrast in the image, are platinum particles. (b) High-magnification BF-STEM image of the region surrounded by broken black lines in (a). It is possible to distinguish between the ionomer and carbon particles based on their crystallinity. (c) HAADF-STEM image of the same field of view as (a). It is impossible to distinguish the ionomer and carbon particles. (d) Electrostatic potential image of the same field of view as (a) and (c). The image intensity is high in the carbon particle region when compared to that of the ionomer region. Accordingly, the carbon particles and the ionomers can be distinguished.

Fig. 6

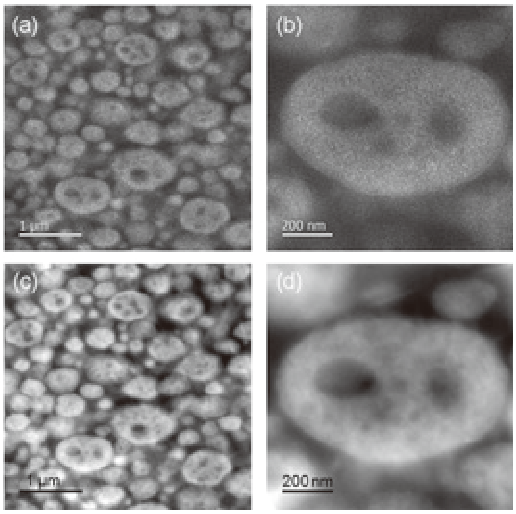

(a)(b) HAADF-STEM images and (c)(d) electrostatic potential images of the nylon/elastomer alloy. In these electrostatic potential images, it is possible to confirm the existence of small nylon phases, several tens of nanometers in size, inside the elastomer island phases.

nylon phases, several tens of nanometers in size, inside the elastomer island phases. Thus, electrostatic potential imaging can provide a high signal-to-noise ratio and high contrast image even with the same electron dose as HAADF-STEM imaging, thereby enabling precise analysis of phase-separated structures.

Summary

In this study, we applied electrostatic potential imaging via DPC STEM to various organic materials and confirmed its effectiveness. Electron staining is generally used to observe organic materials composed of multiple components. However, if the materials have sufficient electrostatic potential difference between each component, the phase-separated structure can be visualized using electrostatic potential imaging even without electron staining. Therefore, the original structure can be observed without concerns of deterioration due to electron staining. Moreover, since electrostatic potential imaging allows visualization of phase-separated structures that electron staining is not applicable, electrostatic potential imaging is highly effective as a novel imaging method for organic materials. However, because of its high sensitivity for electrostatic potential, new problems (e.g., requirement for samples of highly uniform thickness) emerge. Therefore, improving the precision of electrostatic potential imaging and developing a higher quality sample preparation method are important aspects to be considered for future research.

Acknowledgments

We thank Dr. N. Shibata and Dr. T. Seki (The University of Tokyo), Dr. K. Ishizuka and Dr. A. Ishizuka (HREM Research Inc.) for their valuable discussions. We thank Dr. S. Kobayashi, Mr. T. Takamoto, and Dr. S. Shimomura (Toray Industries, Inc.) for providing the samples.

References

[1] K. Kato, "Osmium Tetroxide Fixation of Rubber Latices", *J. Electron Microsc*. **14**, (1965) 219-220.
[2] J.S. Trent, J.I. Scheinbeim, and P.R. Couchman, "Ruthenium Tetraoxide Staining of Polymers for Electron Microscopy", *Macromolecules* **16**, (1983) 589-598.
[3] N.H. Dekkers, and H. de Lang, "Differential phase contrast in a STEM", *Optik* **41**, (1974) 452-456.
[4] H. Rose, "Nonstandard imaging methods in electron microscopy", *Ultramicroscopy* **2**, (1977) 251-267.
[5] N. Shibata, Y. Kohno, S.D. Findlay, H. Sawada, Y. Kondo, and Y. Ikuhara, "New area detector for atomic-resolution scanning transmission electron microscopy", *J. Electron Microsc*. **59(6)**, (2010) 473-479.
[6] N. Shibata, S.D. Findlay, Y. Kohno, H. Sawada, Y. Kondo, and Y. Ikuhara, "Differential phase-contrast microscopy at atomic resolution", *Nat. Phys*. **8**, (2012) 611-615.
[7] N. Shibata, T. Seki, G. Sanchez-Santolino, S.D. Findlay, Y. Kohno, T. Matsumoto, R. Ishikawa, and Y. Ikuhara, "Electric field imaging of single atoms", *Nat. Commun*. **8**, (2017) 15631.
[8] N. Shibata, S.D. Findlay, H. Sasaki, T. Matsumoto, H. Sawada, Y. Kohno, S. Otomo, R. Minato, and Y. Ikuhara, "Imaging of built-in electric field at a p-n junction by scanning transmission electron microscopy", *Sci. Rep*. **5**, (2015) 10040.
[9] J.N. Chapman, P.E. Batson, E.M. Waddell, and R.P. Ferrier, "The direct determination of magnetic domain wall profiles by differential phase contrast electron microscopy", *Ultramicroscopy* **3**, (1978) 203-214.
[10] J.N. Chapman, I.R. McFadyen, and S. McVite, "Modified differential phase contrast Lorentz microscopy for improved imaging of magnetic structures", *IEEE Trans. Magn*. **26(5)**, (1990) 1506-1511.
[11] K. Kurushima, K. Tanaka, H. Nakajima, M. Mochizuki, and S. Mori, "Microscopic magnetization distribution of Bloch lines in a uniaxial magnet", *J, Appl. Phys*. **125**, (2019) 053902.
[12] T. Matsumoto, Y.-G. So, Y. Kohno, H. Sawada, Y. Ikuhara, and N. Shibata, "Direct observation of $\Sigma 7$ domain boundary core structure in magnetic skyrmion lattice", *Sci. Adv*. **2**, (2016) e1501280.
[13] T. Matsumoto, Y.-G. So, Y. Kohno, H. Sawada, R. Ishikawa, Y. Ikuhara, and N. Shibata, "Jointed magnetic skyrmion lattices at a small-angle grain boundary directly visualized by advanced electron microscopy", *Sci. Rep*. **6**, (2016) 35880.
[14] I. Lazic, E.G.T. Bosch, and S. Lazar, "Phase contrast STEM for thin samples: Integrated differential phase contrast", *Ultramicroscopy* **160**, (2016) 265-280.
[15] M. Tosaka, R. Danev, and K. Nagayama, "Application of Phase Contrast Transmission Microscopic Methods to Polymer Materials", *Macromolecules* **38**, (2005) 7884-7886.
[16] A. Ishizuka, M. Oka, T. Seki, N. Shibata, and K. Ishizuka, "Boundary-artifact-free determination of potential distribution from differential phase contrast signals", *Microscopy* **66**, (2017) 397-405.
[17] M.C. Scharber and N.S. Sariciftci, "Efficiency of bulk-heterojunction organic solar cells", *Prog. Polym. Sci*. **38**, (2013) 1929-1940.
[18] A.J. Heeger, "25th Anniversary Article: Bulk Heterojunction Solar Cells: Understanding the Mechanism of Operation", *Adv. Mater*. **26**, (2014) 10-28.
[19] G. Yu, J. Gao, J.C. Hummelen, F. Wudl, and A.J. Heeger, "Polymer Photovoltaic Cells: Enhanced Efficiencies via a Network of Internal Donor-Acceptor Heterojunctions", *Science*. **270**, (1995) 1789-1791.
[20] B.G. Mendis, S.J. Bishop, C. Groves, M. Szablewski, A. Berlie, and D.P. Halliday, "Plasmon-loss imaging of polymer-methanofullerene bulk heterojunction solar cells", *Appl. Phys. Lett.* **102**, (2013) 253301 1-4.
[21] M. Reyes-Reyes, K. Kim, and D.L. Carroll, "High-efficiency photovoltaic devices based on annealed poly(3-hexylthiophene) and 1-(3-methoxycarbonyl)-propyl-1-phenyl-(6, 6)C_{61} blends", *Appl. Phys. Lett*. **87**, (2005) 083506 1-3.
[22] Z. Gu, T. Kanto. K. Tsuchiya. T. Shimomura, and K. Ogino, "Annealing Effect on Performance and Morphology of Photovoltaic Devices Based on Poly(3-hexylthiophene)-b-Poly(ethylene oxide)", *J. Polym. Sci. A Polym. Chem*. **49**, (2011) 2645-2652.
[23] S. Inamoto, S. Shimomura, and Y. Otsuka, "Electrostatic Potential Imaging of Phase-separated Structures in Organic Materials via Differential Phase Contrast Scanning Transmission Electron Microscopy", *Microscopy* (2020) accepted.
[24] H. Yang, S.W. LeFevre, C.Y. Ryu, and Z. Bao, "Solubility-driven thin film structures of regioregular ploy(3-hexyl thiophene) using volatile solvents", *Appl. Phys. Lett*. **90**, (2007) 172116.
[25] B.C.H. Steele and A. Heinzel "Materials for fuel-cell technologies", *Nature* **414** (2001) 345–352.
[26] H.A. Gasteiger, S.S. Kocha, B. Sompalli, and F.T. Wagner "Activity benchmarks and requirements for Pt, Pt-alloy, and non-Pt oxygen reduction catalysts for PEMFCs", *Appl. Catal. B: Environ*. **56** (2005) 9–35.
[27] S. Inamoto, A. Yoshida, and Y. Otsuka, "Three-dimensional Analysis of Non-stained Polymer Alloy Using Differential Phase Contrast-STEM Tomography", *Microsc. Microanal*. **25**(Suppl 2), (2019) 1826-1827.

Visualization of Biological Structures by Ultra High-Voltage Electron Cryo-Microscopy

Kaoru Mitsuoka Research Center for Ultra-High Voltage Electron Microscopy, Osaka University

Structural analysis by electron cryo-microscopy at near-atomic resolution has been generalized through electron direct detectors and so on. On the other hand, electron microscopy has been used as a tool for high-resolution visualization of the cellular structures traditionally, and techniques for cellular structural analysis at higher resolution has been developed. Here we introduce possible uses of ultra-high voltage electron microscopy (UHVEM) toward high-resolution structural analysis for biological sciences, especially an application for neuron model cultured cells.

Introduction

Recently, single-particle electron cryo-microscopy (cryo-EM) is widely used for high-resolution structural analysis of biomolecules and their complexes, and it is now accepted as one of the fundamental techniques of structural analysis for biomolecules as X-ray crystallography and Nuclear Magnetic Resonance spectroscopy [1]. On the other hand, electron microscopy has been used as a tool for high-resolution visualization of the cellular structures traditionally, and cryo-EM is also used as a visualizing tool of fine structures of organelle and so on in cells. Recently it has become more popular to determine the structures of biomolecules and their complexes at near-atomic resolution in the cellular environment by electron tomography and sub-tomogram averaging [2]. Thus, it is expected to use cryo-EM for structural analysis of biomolecules and their complexes in cells.

However, cells are usually too thick to analyze structurally at high resolution by EM operated at conventional accelerating voltage and so the sample thickness must be reduced by some techniques. Recently, it has been generalized to use focused ion beam (FIB) and scanning electron microscopy (SEM) to make lamellas from biological cryo-samples [3], but observing cells as they are should be more efficient for a method to analyze inside the cells. Ultra-high voltage electron microscopy (UHVEM) is one of the possible methods to observe at least some regions of many cells directly. Thus, here we would like to explain the current situation for the ultra-high voltage cryo-EM (cryo-UHVEM) operated at 1 MeV, which is introduced recently to our center.

Visualization of fine structures in cells by electron cryo-microscopy

Biomolecules and their complexes are working in the cellular environment. Thus, observing their structures and the localization in cells is essential to understand their functions in the native environment. Observing their localization by light microscopy has become general by using fluorescent labels like green fluorescent protein, and resolution of light microscopy using fluorescent labels has improved by the development of super-resolution microscopes [4]. However, to visualize the structural changes for biomolecules to function, for an instance, the use of electron microscopy is essential. Electron microscopes have enough resolution to visualize atoms and attempts using electron microscopes to visualize cells have been made from the initial development. However, cells can function only in water environment and it is difficult to insert them into the vacuum of electron microscopes with their native structures. Currently to solve this problem, fixation is used to preserve the structures in the vacuum and two types of fixation, chemical or physical fixation, are used.

Chemical fixation uses cross-linkers to fix the structures of biomolecules even in the vacuum by linking the two different positions in the biomolecules. As the cross-linkers, glutaraldehyde is usually used for electron microscopy. After fixing by glutaraldehyde, the specimens are dehydrated and then embedded in resin to make ultra-thin sections by a diamond knife, which is thin enough to observe by transmission electron microscopy (TEM). Then by staining by heavy atoms, the contrast of biomolecules by TEM can be enhanced. By this method, fine structures of cells have been visualized and studied. In addition, by applying electron tomography, which will be explained later, to the sections, it is possible to obtain the three-dimensional structures. Recently using the biological samples fixed chemically, three-dimensional reconstruction of the large area of the samples become possible by serial block-face SEM, which is used to observe the sample by SEM after cutting the surface by FIB or by a diamond knife serially. However, the resolution of the imaging is limited to about 2 nm by chemical fixation and/or staining.

On the other hand, the resolution of single-particle cryo-EM become near-atomic resolution as explained above. For the single-particle cryo-EM, physical fixation is used. By the physical fixation, biological specimens in solution at about room temperature are rapidly frozen to about liquid-nitrogen temperature in milli-seconds. Then the biological specimens are embedded in amorphous ice with biological molecules in the

〉〉Ibaraki, Osaka 567-0047, Japan | E-mail: kaorum@uhvem.osaka-u.ac.jp

specimen without changing their native structures in the solution at about room temperature. As the methods for rapid freezing, several methods, as metal contacting and immersion to cooling medium, are known, and we used immersion into liquid ethane for rapid freezing of cultured cells, which will be explained later. For the freezing, an automatic plunge freezer, Leica EM GP, was used. In the Leica EM GP, the excess solution of the biological specimen was blotted by filter paper from one side of the EM grid without damage to the cultured cells on the grid, and then the cells could be fixed as it is.

Ultra-High Voltage Electron Cryo-Microscopy

The sizes and the shapes of the cells are widely different but many human cells are typically several to tens μm in diameter. Thus, they are too thick to penetrate electrons accelerated at the voltage of typical electron microscopes and so only the area that is thin enough for electrons to transmit could be observed. On the other hand, UHVEMs could be used for many areas of cells visualizing the fine structures inside cells. Especially if we use rapid-freezing technique, as descried above, fine structures of cells, which were constituted by biomolecules, could be preserved at high resolution. Thus, cryo-UHVEM might be used for high-resolution structural analysis of biomolecules and their complexes in cells. Here we apply this technique to neuron model cultured cells and show the results.

However, before going to the application for the cultured cells, we would like to consider about some other applications. The features of UHVEM are high penetration ability of electrons to the sample and high resolution because of the short wavelength [6]. Thus, if we utilize these features to single-particle cryo-EM, high-resolution structural analysis of biological samples with extremely high molecular weight become possible. For example, as the sample with extremely high molecular weight, virus with an exceptionally large diameter could be considered. For the specimen over 100 nm diameter, the resolution of structural analysis by EM is limited by the effect of Ewald sphere and the resolution d can be evaluated as

$$d \approx \sqrt{\frac{2}{t\lambda}}$$

with a diameter t and wavelength λ [7]. In the case of virus with 120 nm diameter, because the wavelength of electrons with accelerating voltage of 300 kV is about 3 pm, the resolution is about 0.4 nm. In the case of electrons with accelerating voltage of 1 MV, because the wavelength is 0.9 pm, the resolution of 0.23 nm could be achieved.

To achieve near-atomic resolution, cryo-UHVEM could be used but taking many images is necessary for single-particle cryo-EM. To take many images, cryo-EM with an autoloader is preferable. The cryo-UHVEM installed in our center has an autoloader with 12 slots for cryo-grid as in CRYO ARM$^{\mathrm{TM}}$ and the appropriate grid can be observed from the 12 grids. However, no automated software for single-particle data collection can be used for the cryo-UHVEM currently and so many images must be collected manually. The overall picture of the cryo-UHVEM in our center is shown in **Fig. 1**.

Sample preparation of neuron model cultured cell NK108-15 for cryo-EM

The next example is the application to structural analysis in the cells. We selected NG108-15 as a model cultured cell related to neurons. Neurons extend axons to transmit the signals and also grow dendrites, which are branched protoplasmic extensions, to get the signals from other neurons. The fine extensions of the growth cone, which are hand-like structure found in the tips of axons and dendrites, are pointed filopodia

Fig. 1 Materials- and Bio-Science Ultra-High Voltage Electron Microscope

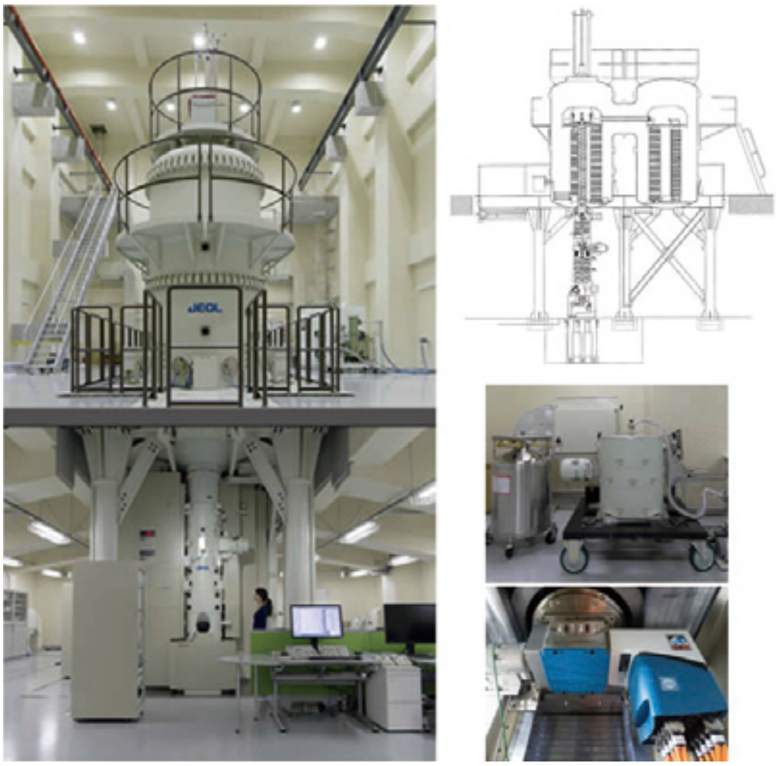

The left panel shows the overview of the cryo-UHVEM installed to the Research Center of Ultra-High Voltage Electron Microscopy, Osaka University. The right panels show the sectional view of the EM and the direct electron camera, K2 IS (Gatan), etc.

and lamellipodia like the webbing of the hands that are important for axon growth and guidance. Because the filopodia is about 100-250 nm in diameter, the ice thickness of the frozen specimen is especially suitable for observation by TEM with the usual accelerating voltage. The mean free energy of electrons in ice is about 500 nm for 300 kV and about 900 nm for 1 MV, and so it is possible to observe the specimen with about 1 µm thick by cryo-UHVEM. Thus, if we use the cryo-UHVEM, not only the filopodia but also the part of the lamellipodia and the surrounding thicker area could be observed.

For cryo-UHVEM observation, we cultured the NK108-15 cells on the EM grids directly [8]. For the grids, we used those made with Au to avoid toxicity to the cells and with carbon films with periodically spaced holes (Quantifoil). The hole size is 0.6 µm in diameter, which is the smallest in normally available ones, to have more filopodia across the holes. On the carbon films, we absorbed colloidal golds in about 20 nm diameter as positional markers and then evaporated carbon on the grids to use for cell culture. The grids were covered by laminin to enhance cell adhesion and then NK108-15 cells were cultured on the grids as usual. The EM grids with cultured cells on the carbon films were shown in **Fig. 2**. To grow filopodia, the neuron model cultured cells were activated by cAMP. The grids with the cultured cells were rapidly frozen by plunge freezing as described above for cryo-EM observation.

The cryo-UHVEM installed in our center was equipped with a direct electron detector, K2 IS (Gatan). By the direct electron detectors, the resolution of the cryo-EM structural analysis for biological specimen has improved dramatically. One of the reasons of the improvement is the high detective quantum efficiency of the detectors but another reason is the movie collection by the CMOS detectors. By using the K2 IS camera, it is possible to collect 1600 frames per 1 second. By movie collection, it is shown that the ice specimen is deforming by electron irradiation and that the particles in the ice are moving while EM observation. The movement by electron irradiation is called beam-induced movement of the sample. Thus, in single-particle cryo-EM, the particle movements were compensated by averaging each frame with correction of the movements to achieve the high resolution [9]. In electron tomography, the movie correction also can be used to improve the resolution of the structural analysis. For the precise movie correction, it is better to have positional markers closer to the cultured cells as in the solutions compared with the markers on carbon films as described above. Thus, we need more adjustment for the sample preparation like better positional markers for cells, keeping their native functions.

Damages of biological samples by electron irradiation in electron cryo-microscopy

The resolution of biological specimen by electron cryo-tomography (cryo-ET) is limited by the electron irradiation damage. For example, to analyze the structure of biological specimen at higher than 3 Å resolution, the total electron doses irradiated to the specimen should be less than about 30 e^-/A^2. In single-particle cryo-EM, the images can be collected at the electron dose, and then high-resolution structure can be calculated by averaging the particle images collected from many different areas. However, in cryo-ET, because the three-dimensional (3D) structure is reconstructed from the tilt series, many images should be collected from the same area, as shown in **Fig. 3**. For example, if we collect tilt series from -70 degrees tilt to 70 degrees tilt at 2 degrees step, the total electron dose become about 100 e^-/A^2 even when only 1 e^-/A^2 dose is used for each image. Thus, it is impossible to get the 3D structure at near-atomic resolution. As described below, 3D reconstruction at near-atomic resolution is possible only when the same structures could be found in the specimen. Then the images taken at the total electron dose suitable for high-resolution structural analysis are used to calculate the subtomograms and then the subtomograms are averaged as in the single-particle cryo-EM to get the 3D structure at high resolution.

Recent structural analysis by cryo-ET assumes the subtomogram

Fig. 2 NK108-15 cells cultured on an EM grid

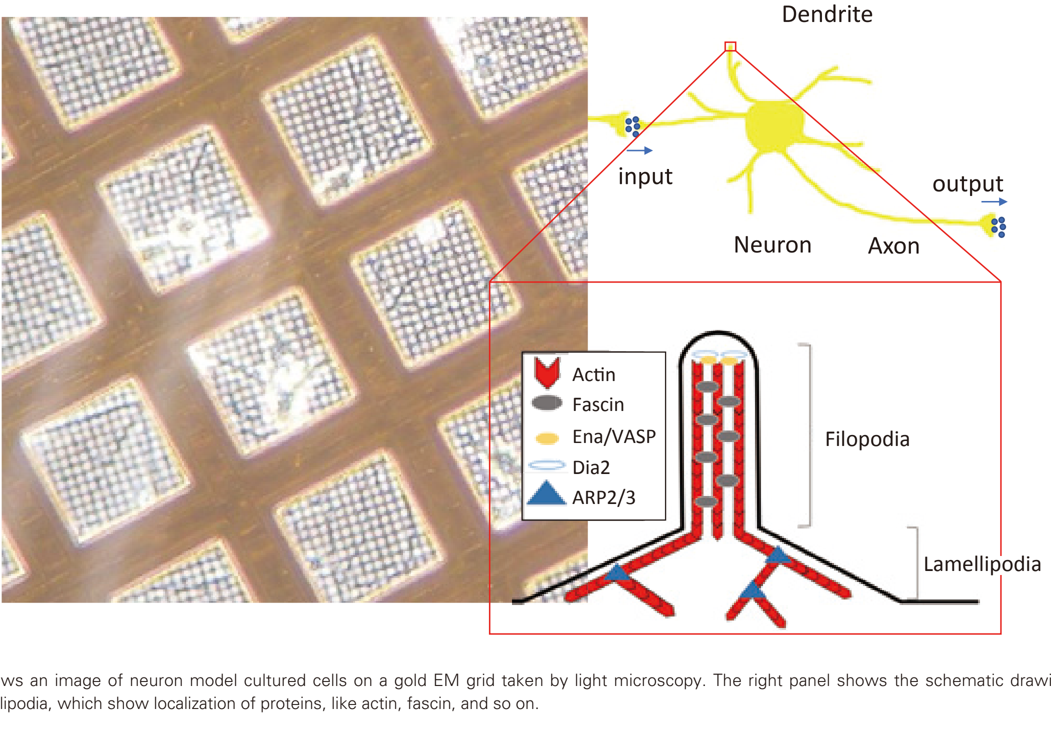

The left panel shows an image of neuron model cultured cells on a gold EM grid taken by light microscopy. The right panel shows the schematic drawings of a neuron, filopodia and lamellipodia, which show localization of proteins, like actin, fascin, and so on.

averaging for high-resolution structure determination. For this purpose, it is better to collect images at low-tilt angles before the high-tilt images and then subtomogram averaging at higher resolution could be achieved. Thus, the symmetric tilt scheme, which begins from the non-tilt image and then alternates between increasingly positive and negative tilts, should give the structure at the highest resolution [10]. However, the symmetric tilt scheme is not widely used mainly because of the limitation of automated data acquisition, and so it is also used to collect tilt series from an appropriate low angle to non-tilt up to high tilt angles and then collect the tilt series from the same low angle to the opposite direction. As the initial trial for data collection by cryo-UHVEM, we collected several tilt-series from high tilt angles to the opposite direction by the Recorder program from TEMography.com but we would like to use the tilt scheme from an appropriate low-tilt angle for structural analysis at higher resolution.

In addition, the contrast of the subtomograms to be averaged is limited because of the limited electron dose for collecting the tilt series for 3D reconstruction and so it is difficult to identify the region of interest by cryo-ET. Thus, it is advantageous to use the phase plate. By using the phase plate, the contrast transfer function for imaging could be changed from sin-form to cos-form, and so the low-frequency information in inverse space could be enhanced [11]. Actually, we introduced the phase plate to 300 kV cryo-EM and could get the better contrast EM images. Thus, if we can introduce the hole-free phase plate to the cryo-UHVEM, the contrast of tomograms should improve and the subtomogram averaging should become efficient. Furthermore, the limited total electron dose described here is when the specimen is kept at the liquid-nitrogen temperature. At the liquid-helium temperature, it is thought to be able to irradiate more electrons to biological specimen with the same damage [12]. However, the beam-induced movement described above should become more prominent at the liquid-helium temperature but the improvement of movie correction to compensate the beam-induced movement might advance the use of liquid-helium for cryo-EM.

Subtomogram averaging by electron cryo-tomography

We collected several tilt-series from filopodia of NK108-15 cells and reconstructed the 3D volumes by the program for tomographic reconstruction IMOD [13]. As shown in Fig. 3, we calculated the 3D reconstructions by weighted back-projection, and then the calculated volumes are used as the initial model for simultaneous iterative reconstruction technique (SIRT) to get the 3D reconstruction with less artifacts. Because the noise in the reconstruction is severe in cryo-ET, reconstruction by SIRT, which is more time-consuming than the weighted back-projection, is necessary to get interpretable reconstructions. As a result, we could observe the bundles of actin filaments in filopodia clearly as shown in **Fig. 4**.

Although the actin filaments were clearly visualized, the resolution of the reconstruction is not good enough to see the protein fascin, which interacts with actin filaments to make the bundle. Thus, we applied the subtomogram averaging to the complex of actin filaments and fascin, which is thought to have the same structures in cells. As in the single-particle cryo-EM, which averages the particle images, the high-resolution structure of the complex should appear by averaging the subtomograms. To pick the regions of the complex from the tomogram, we used the periodic features of the actin bundles. As shown in **Fig. 5**, we could identify the periodic structures corresponding to the pitch of actin filaments and the periodic densities with the same pitch to connect the actin filaments, which we assumed to be the positions of fascin. Then we cut out those positions from the tomogram and applied the subtomogram averaging using the program RELION, which is also used for the single-particle cryo-EM. As a result, the resolution of the averaged structure was estimated to be 2.6 nm. Thus, by optimizing the electron dose for 1 MV, by changing the tilting scheme suitable for subtomogram averaging and by increasing the number of tomograms, we are expecting to improve the resolution, being able to fit the atomic models of actin and fascin clearly.

Fig. 3 Electron tomography

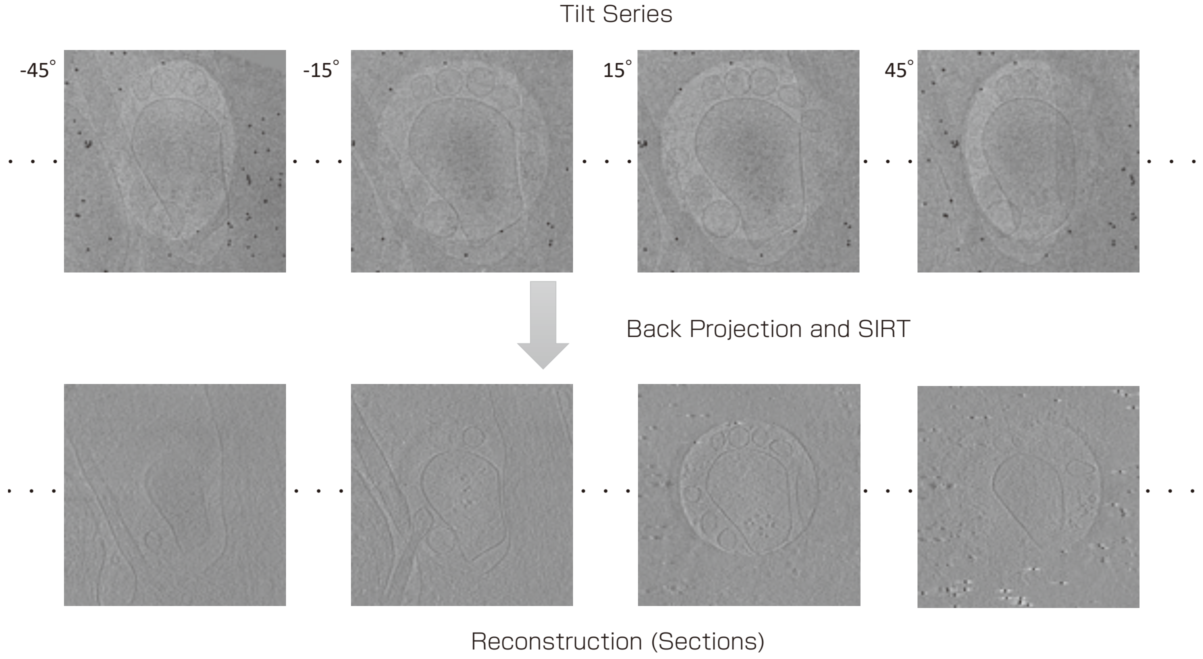

The upper panels show an example of a tilt series taken by the cryo-UHVEM. The lower panels show the sections of the 3D reconstruction calculated by SIRT using the reconstruction by weighted back-projection as the initial model.

Fig. 4 Visualization of a bundle of actin filaments

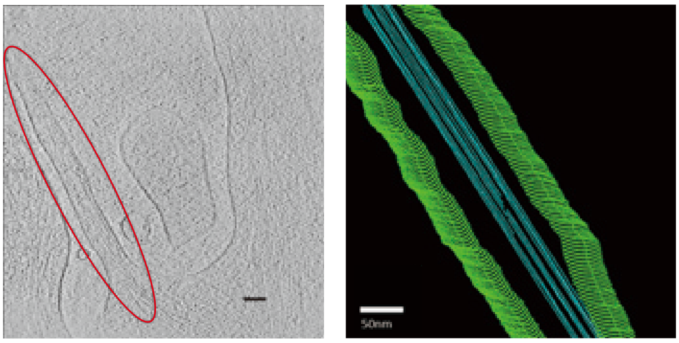

The left panel shows a reconstruction of filopodia by electron tomography by cryo-UHVEM. On the right panel, the identified actin filaments and the membrane in the reconstruction were indicated by blue and green colors, respectively.

Fig. 5 Arrangement of Fascin

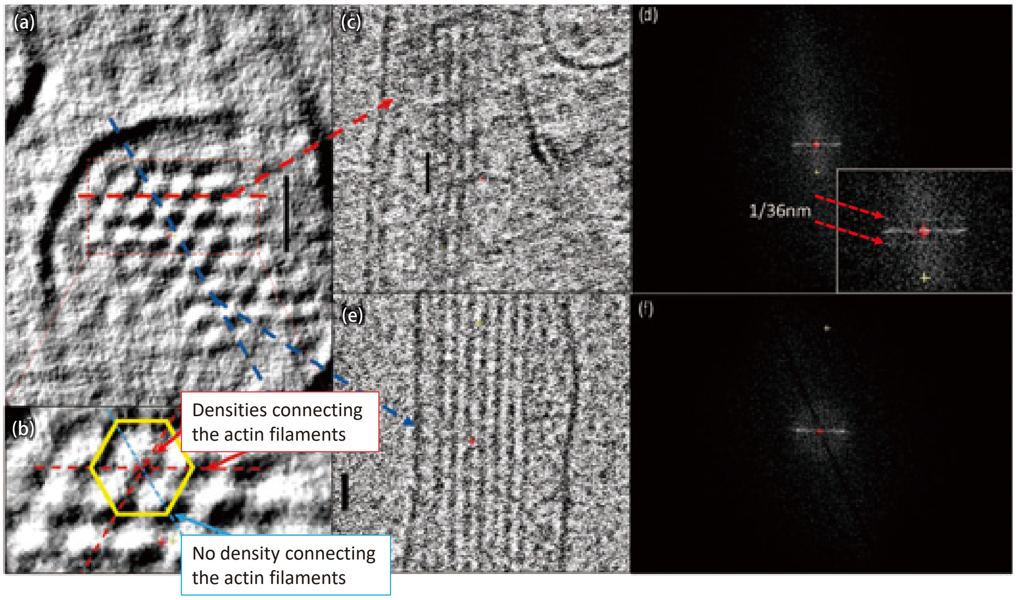

A section of the bundle of actin filaments shown in Fig. 4 is shown in the left panel. The hexagonal array of the actin filaments is clearly visualized. The fascin densities connecting the actin filaments were confirmed on the red dashed line. In the central panel (c), the section through the red line is shown and periodic lines with the pitch of 36.8 nm, which is confirmed in the Fourier transform (d) as layer lines, are observed. No connecting density is found on the blue dashed line, no periodic line is found in the section (e), and no layer line is observed in the Fourier transform (f).

Future prospect

As described here, a cryo-UHVEM was installed in the Research Center of Ultra-High Voltage Electron Microscopy, Osaka University. Thus, we applied it for the neuron model cultured cells to investigate its use for the structural analysis in cells. In addition, we started to collect single-particle images of the virus with extremely high molecular weight. However, there was an earthquake in the north of Osaka in June, 2018, and the high-voltage electron microscopes in our center were damaged and we found that both need major fixes. Thus, here we described the results of data collection that we could get before the earthquake, toward the structural analysis in cells. We could get the budget to fix the microscopes in 2018, and we could start to fix them in 2019. Now we just finished fixing the cryo-UHVEM and so we can start optimizing the electron dose and changing the tilting scheme and so on. By these fundamental experiments, we would like to advance the study for the cryo-UHVEM for their wide use for the high-resolution structural analysis of biomolecules.

Acknowledgements

I would like to thank Dr. Hidehiro Yasuda, the director of the research center of ultra-high voltage electron microscopy, Osaka university, for his effort to install and fix the cryo-UHVEM, and all the JEOL members who actually worked to install and fix it.

References

[1] Merk A, Bartesaghi A, Banerjee S, Falconieri V, Rao P, Davis MI, Pragani R, Boxer MB, Earl LA, Milne JLS, Subramaniam S: *Cell* **165**, 1698–1707 (2016).
[2] Asano S, Engel BD, Baumeister W: In Situ Cryo-Electron Tomography: A Post-Reductionist Approach to Structural Biology. *J. Mol. Biol*. **428**, 332–343 (2016).
[3] Weber MS, Wojtynek M, Medalia O: *Cells* **8**, 57 (2019).
[4] Achimovich AM, Ai H, Gahlmann A: *Curr. Opin. Struct. Biol*. **58**, 224–232 (2019).
[5] Smith D, Starborg T. *Tissue Cell* **57**, 111–122 (2019).
[6] Murata K, Shigemoto R: *Kenbikyo* **46**, 170-174 (2011).
[7] Zhu D, Wang X, Fang Q, Van Etten JL, Rossmann MG, Rao Z, Zhang X: *Nat. Commun*. **9**, 1552 (2018).
[8] Aramaki S, Mayanagi K, Jin M, Aoyama K, Yasunaga, T: *Cytoskeleton* **73**, 365–374 (2016).
[9] Li X, Mooney P, Zheng S, Booth CR, Braunfeld MB, Gubbens S, Agard DA, Cheng Y: *Nat. Methods* **10**, 584–590 (2013).
[10] Hagen WJH, Wan W, Briggs JAG: *J. Struct. Biol*. **197**, 191–198 (2017).
[11] Malac M, Beleggia M, Kawasaki M, Li P, Egerton RF: *Ultramicroscopy* **118**, 77–89 (2012).
[12] Mitsuoka K: *Micron* **42**, 100-106 (2011).
[13] Mastronarde DN, Held, SR: *J. Struct. Biol*. **197**, 102–113 (2017).
[14] Bharat TAM, Scheres SHW: *Nat. Protoc*. **11**, 2054–2065 (2016).

Observation of Phase Objects using STEM - Differential Phase Contrast (DPC) Microscopy

Akimitsu Ishizuka, Kazuo Ishizuka
HREM Research Inc.

Scanning transmission electron microscopy (STEM) becomes popular owing to its compatibility with analytical capability. However, it is difficult to observe a phase object using STEM. The differential phase contrast (DPC) microscopy has been proposed to overcome this limitation. Here, a detector is split into two halves, and an image signal (the DPC signal) is given by a difference between the signals from two segments. The split detector has been used to observe a magnetic structure at a low/medium magnification. On the other hand, it has recently been shown that the DPC signals with atomic resolution can be obtained using a multiple quadrant detector. Since it has been demonstrated that the DPC signal is a derivative of phase distribution function of an exit wave, the phase distribution can be restored by integrating the DPC signal. In this report, we introduce the discrete cosine transform (DCT) to integrate the DPC signals for obtaining the phase distribution, because the DCT is consistent with the Neumann boundary condition that is applicable to the data observed only in a finite region. In addition, we describe the real-time integration method that displays the phase distribution in accord with STEM scanning. After that, using the model structure we compare the phase distributions restored by the DCT and the method based on fast Fourier transform (FFT). Then, using experimental data obtained from single-layer graphene we will discuss on observation of phase objects in atomic resolution.

Introduction

The materials act as a phase object for an electron beam, and a high-resolution image observed by transmission electron microscopy (TEM) reflects a phase modulated by the object. For a thin sample, this phase modulation is proportional to the electrostatic potential of the sample, which is approximately proportional to the atomic number. Therefore, the phase contrast image obtained by TEM is important for analyzing the atomic structure of the sample. In recent years, scanning transmission electron microscopy (STEM) has become remarkably popular owing to its compatibility with analysis capabilities, such as electron energy loss spectroscopy. Especially, STEM is particularly effective in analyzing atomic structures in conjunction with aberration correction technology. In high-angle annular dark-field (HAADF) images obtained by STEM, heavy elements can be selectively detected, since image contrast is approximately proportional to the square of the atomic number. However, this means that HAADF images are not suitable to detect light elements. Recently, the annular bright-field (ABF) STEM [1] that can detect light elements has been proposed, but its contrast does not directly represent a phase change as observed by TEM. From the reciprocity theorem the bright-field method in STEM using a small disc-shaped detector, as shown in **Fig. 1** (a), makes it possible to obtain a phase contrast image equivalent to that in TEM. However, the imaging efficiency of this bright-field STEM is extremely poor compared with the one for the phase contrast in TEM, since only a part of incident electrons that hit the small detector contribute to the image formation.

Dekkers and de Lang [2] proposed differential phase contrast (DPC) microscopy to observe a phase object in STEM, where all transmitted electrons are collected by a split detector as shown in Fig. 1 (a), and the difference signal between the outputs from two segments is used to create an image. They demonstrated that using a scanning optical microscope, a phase change perpendicular to the bisector of the detector can be observed. Later, Waddell and Chapman [3] showed that the centroid (center of mass) of the electron diffraction intensity is proportional to a gradient of the phase distribution function. They also showed that the difference signal from the split detector closely approximates the component of the centroid perpendicular to the bisector. Then, if we use a four-segment (quadrant) detector [4] as shown in Fig. 1 (b), without rotating the split detector, approximate differentials of the phase distribution in two perpendicular directions can be obtained simultaneously with a single beam scan. Recently, it has been shown that the DPC signals with atomic resolution can be obtained using multiple quadrant detectors [5]. Now, an eight-segment (double-quadrant) detector and an annular four-segment detector as shown in Figs. 1 (c) and (d), respectively, have been made commercially available. It should be noted here the phase

〉〉 14-48 Matsukazedai, Higashimatsuyama, Saitama 355-0055, Japan | E-mail: ishizuka@hremresearch.com

distribution can be obtained by integrating the DPC signal, since the DPC signal is a gradient of the phase distribution function. Therefore, DPC in STEM (STEM-DPC) not only allows us to detect a phase object, but also gives us an electrostatic potential of a sample that is important for analysis of a sample structure, by integrating the DPC signal.

On the other hand, the propagation direction of electrons is changed by Lorentz force of an electro-magnetic field, which gives contrast of Lorentz microscopy image in TEM. Similarly, Chapman et al. [6] showed that electro-magnetic fields could be observed, if the displacement of the transmission disk when the electron beam passes through the sample is detected by a split detector at each scanning point of the STEM. A recent study of magnetic field observation with an aberration-corrected STEM was discussed by a group at Glasgow University in JEOL News [7].

In recent years, a high-speed pixelated detector (Fig. 1 (e)) that measures diffraction intensity distribution from each scanning point is getting closer to practical use. In this case, since two-dimensional diffraction intensity is obtained for each two-dimensional scanning point, the four-dimensional 4D-STEM data is obtained. Then, a highly accurate DPC signal can be obtained from the centroid of the diffraction intensity distribution of the 4D-STEM data. By using this DPC signal, it is also possible to obtain the phase distribution in quasi-real-time.

In this report we firstly describe the integration methods for obtaining the phase distribution from the DPC signal, and then introduce the qDPC [8], a DigitalMicrograph® plug-in, to which the described integration methods are implemented. In addition, we mention the SD module that directly captures signals from a segmented detector into DigitalMicrograph® and performs phase integration in real time, and also the 4D-STEM module that performs quasi-real-time phase integration from 4D-STEM data obtained by a pixelated detector. Then, we apply DPC integration to an experimental 4D-STEM data obtained from single-layer graphene. Finally, we compare the phase distribution obtained by Ptychography [9] with the phase distribution obtained by integrating the DPC signal.

Integration of the DPC signal

As described above, the DPC signal is the gradient of a phase distribution function, i.e., differential of the phase distribution in two orthogonal directions. Therefore, a phase distribution can be restored by integrating the DPC signal. For this purpose, the following Fourier transform relationship may be used:

$$\partial f(x,y)/\partial x \Leftrightarrow 2\pi i k_x \hat{f}(k_x,k_x) \tag{1}$$

Here, $\hat{f}(k_x,k_x)$ is a Fourier transform of $f(x,y)$, and can be efficiently calculated by using a fast Fourier transform (FFT). When integrating the DPC signal using the Fourier transform, a solution that simultaneously satisfies the two DPC signals, $I_x(x,y)$ and $I_y(x,y)$, should be searched. Among any linear combinations, Close et al. [10] multiplied one of the DPC signals by an imaginary unit i (we call this method FFT-1):

$$\begin{aligned} &I_x(x,y) + iI_y(x,y) = \partial\phi(x,y)/\partial x + i\,\partial\phi(x,y)/\partial y \\ &\Leftrightarrow \hat{I}_x(x,y) + i\hat{I}_y(x,y) = \left(2\pi i k_x - 2\pi k_y\right)\hat{\phi}(k_x,k_x) \end{aligned} \tag{2}$$

On the other hand, a Poisson equation for the phase distribution $\phi(x,y)$ can be obtained when we differentiate the two DPC signals and add them together:

$$\begin{aligned} &\partial I_x(x,y)/\partial x + \partial I_y(x,y)/\partial y = \partial^2\phi(x,y)/\partial x^2 + \partial^2\phi(x,y)/\partial y^2 = \nabla^2\phi \\ &\Leftrightarrow 2\pi i k_x \hat{I}_x(x,y) + 2\pi i k_y \hat{I}_y(x,y) = \left\{(2\pi i k_x)^2 + \left(2\pi i k_y\right)^2\right\}\hat{\phi}(k_x,k_x) \end{aligned} \tag{3}$$

In general, it is necessary to assume a boundary conditions to solve a Poisson equation. Lazic et al. [11] proposed a method using an FFT that assumes periodic boundary conditions (we call this method FFT-2). It may be noted here that we observe the DPC signal that is the derivative of the function to be obtained. Therefore, it should be better to use the Neumann boundary condition that assumes the derivative at the boundary. Then, the discrete cosine transform (DCT) can be used to solve the Poisson equation under Neumann boundary conditions [12].

$$(\lambda_k + \lambda_l)DCT[\phi(i,j)] = DCT[\partial^2\phi(i,j)/\partial x^2 + \partial^2\phi(i,j)/\partial y^2]\Delta^2 \tag{4}$$

Here, DCT indicates the discrete cosine transform, and $\lambda_k = 2\cos(k\pi/m) - 2$. We have implemented the DCT-based solution for integrating the DPC signal to the qDPC [13].

Now, we show the superiority of the DCT solution to the FFT solutions using a synthetic model. **Figure 2** (a) shows the model distribution, and Figs. 2 (b) and (c) show the differences (DPCx, DPCy) of the model distribution in two directions as

Fig. 1 Schematic diagram for differential phase contrast (DPC)

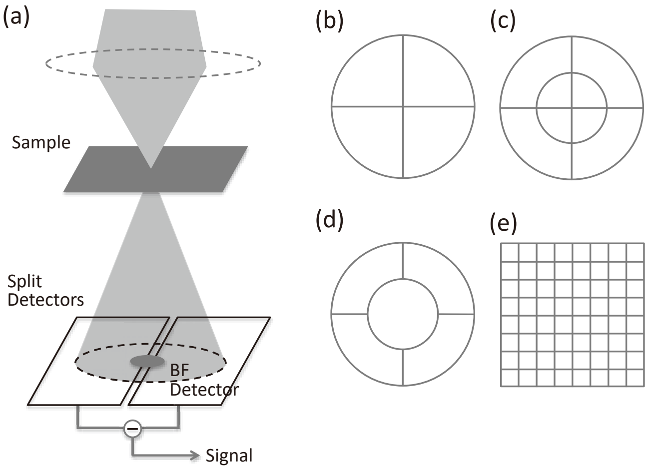

In DPC, all transmitted electrons are detected by a split detector as shown in (a). Using the difference signal between two segments the structure of a phase object that changes perpendicular to the bisector is observed. By using a four-segment detector as shown in (b), it is possible to measure orthogonal DPC signals in two directions simultaneously with a single beam scan. (c) and (d) show a double quadrant (eight-segment) and annular quadrant detectors, respectively, which are commercially available. (e) illustrates schematically a pixelated detector, in which more pixels actually exist.

an approximation of the derivative. Then, we added a random noise of ± 10% of the data range to these differences as shown in (d) and (e), which were used as the model of observed DPC signals. A reconstructed model distribution obtained by integrating the noise added DPCx and DPCy using the DCT is shown in **Fig. 3** (a). For comparison, model distributions obtained by using two FFT methods are shown in Fig. 3 (b) and (c). In the lower part of Fig 3, (d) to (f), show the error in each reconstruction from the model distribution. You may note that in the reconstructions with the FFT there are gradual fluctuations originated from inappropriate periodic boundary conditions. In contrast, the reconstruction with the DCT that employs the Neumann conditions using the differential at the boundary, does not show any appreciable deviation from the model. For this reason, the error in the reconstruction with the DCT is displayed after multiplied by 10, which shows fluctuation equivalent to the random noise added to the signal. We may note here that the results obtained by the DCT as well as two FFTs are smooth, which means the influence of random noise added to the DPC signal is mostly suppressed. As will be described later, using this observation, we can obtain a noise suppressed electric / magnetic field by differentiating the restored phase distribution obtained by integrating an experimental DPC signal.

The integration method described above can be applied only after the whole data are collected at the end of scanning. However, the DPC signals can be progressively displayed according to scanning as other STEM signals. When the phase distribution is displayed in live mode, the throughput of experiment will be significantly improved. If there is no noise in

Fig. 2 Model for evaluating the integration method

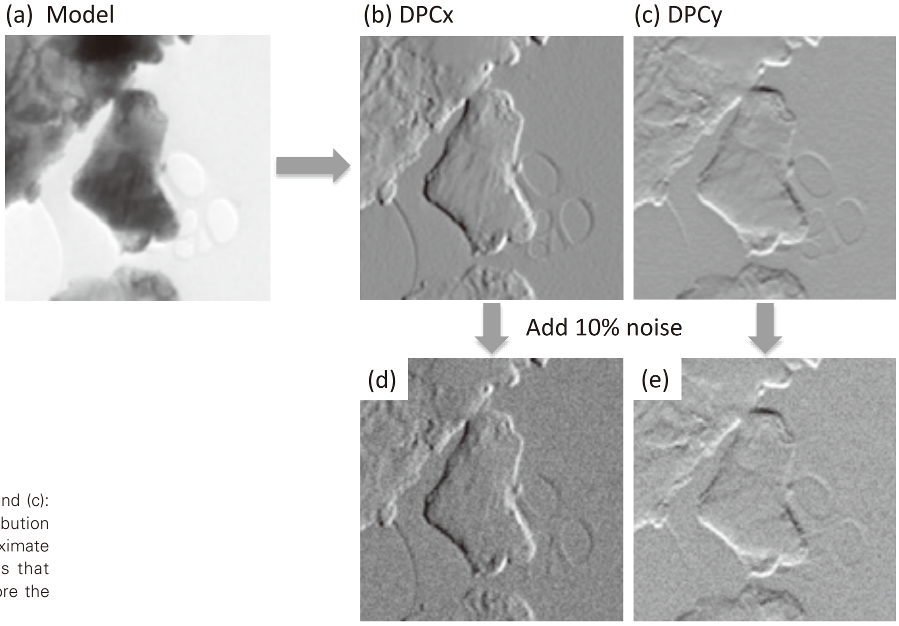

(a): Model distribution function (256 × 256 pixels). (b) and (c): Ideal DPC signals, namely differences of model distribution function along two perpendicular directions that approximate the derivatives. (d) and (e): Noise added derivatives that emulate experiment DPC signals. We attempt to restore the model function from the noise added derivative.

Fig. 3 Phase distributions restored by integration

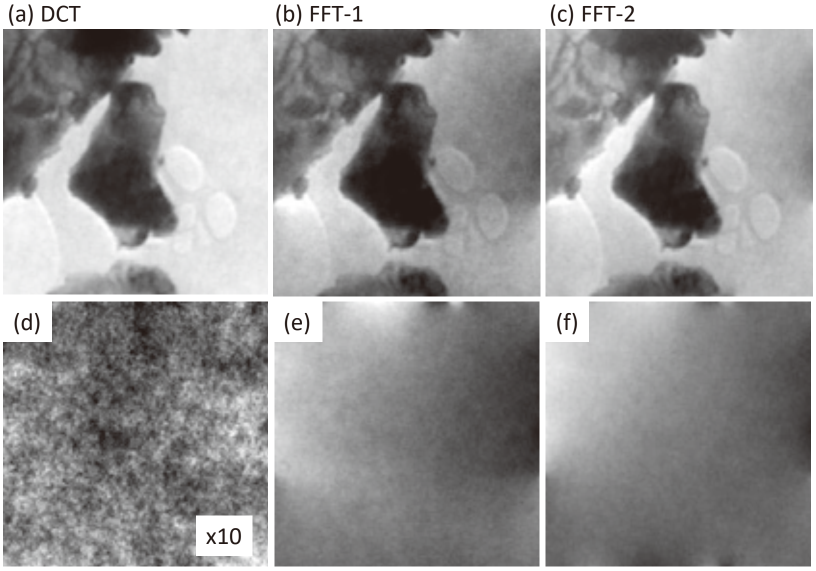

(a): Phase distribution restored by discrete cosine transform (DCT). (b) and (c): Phase distributions restored by two fast Fourier transforms, FFT-1 and FFT-2, respectively. Errors of the reconstructed phase distributions from the model function are shown in (d) to (f), respectively. Since the phase distribution reconstructed by DCT is very close to the model function, the error (d) is displayed after multiplied by 10. On the other hand, the phase distributions restored by the two FFTs show additional slow variations, which result from the failure of the periodic boundary condition.

the DPC signal, a phase distribution may be obtained by simply adding the DPC signals sequentially in the scanning direction. However, there is no experimental data without noise. When we simply add the noise-added DPC signals, shown in Fig. 2, in the horizontal direction, the pronounced horizontal stripes become visible as shown in **Fig. 4** (a). Here, the relationship between the horizontal scan lines is determined by adding the leftmost vertical DPC signal. In contrast, we can obtain Fig. 4 (b), when we estimate the value of the new scanning point from the average of the two derivatives (DPC signals) at the point directly above and the point immediately before. The reconstructed phase is considerably improved compared to (a), although a slowly varying faint pattern appears from top-left to bottom-right. This encourages us to use more the DPC signals to estimate the phase at a new scanning point of interest. Here, we use the fact that all points on the preceding scan line have been already integrated and thus their values have been determined, and that all derivatives on the current scan line are known. Then, using a set of horizontal derivatives on the left and right of the scanning point of interest and a set of vertical derivatives between the previous and current scanning lines, we estimate an integrated value of the said scanning point by the least square method [13]. In Fig. 4 (c), the phase value of the scanning point is determined from the four horizontal and five vertical derivatives (the total of nine DPC signals). From Fig. 4 (d), which shows the error between the model distribution and this integral, it can be seen that the model distribution is determined sufficiently well without influence of noise.

About qDPC Capability

The qDPC [8] is a plug-in for DigitalMicrograph®, and implements the offline capabilities of integrating the DPC signals discussed above. Namely, the qDPC has the following features:

- Functions to create the DPC signal from the signals of a quadrant detector
- Functions to calculate phase distribution by DCT from the DPC signal
- Utilities to correct the DPC signal

In addition, it is possible to evaluate the phase calculated by FFT and the real-time integration routine.

At first, we describe the utilities to correct the DPC signal. Some deficiencies that are not discernible in the DPC signal becomes remarkable when the phase distribution is obtained by integrating the DPC signal. For example, a small adjustment error to the dark level of the segmented detector or misalignment of the transmitted wave on the detector results in a constant imbalance in the DPC signal. Although this imbalance is not visually detectable, it introduces a distinct phase gradient when the DPC signal is integrated. In addition, if an adjustment of the beam deflection system is inaccurate, the transmitted wave moves on the detector according to the beam scanning. When this movement is linear with respect to the scanning position, a slope will appear in the DPC signal. Since a linear function becomes a quadratic function by integration, a slightly inclined plane in the DPC signal may give a remarkable parabolic surface in the integrated phase. Therefore, the qDPC provides the off-line functions of correcting a constant value and/or a constant slope from a DPC signal.

When performing the integration, the coordinate system of the DPC signal, namely the rotation angle of the segmented detector, should coincide with the coordinates of STEM images, namely the scanning system. Also, when displaying electric or magnetic field vectors on a STEM image based on DPC signals, the orientation of the segmented detector should be known in terms of the STEM image coordinate. For this reason, when the segmented detector is installed, the direction of the deflection system is made to match the coordinates of the segmented detector for some camera lengths, or the mutual angle between them is measured and stored as correction data for a later use. In an actual experiment, the operator often rotates the direction of the scanning system, i.e., the STEM image, with respect to the direction of the sample orientation. Therefore, this ad hoc image rotation should be also considered in the relationship between the coordinates of the DPC signal and the image system. Since the rotation adjustment of the DPC signal is so important, the qDPC has the function to determine the rotation angle from the acquired DPC signal

Fig. 4 Phase distribution restored by real-time integration

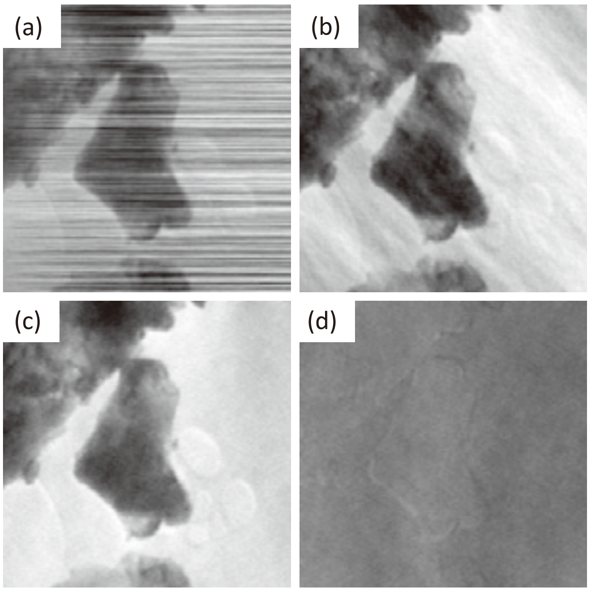

a): The DPC signals are simply added in the scanning direction (horizontal). Pronounced horizontal stripes result from the added noise. (b): The value of a scanning point is obtained by averaging two DPC signals at the directly preceding point and the directly above point. Although weak oblique stripes appear, the restored phase is significantly improved. (c): The value of a scanning point is obtained using four horizontal and five vertical (total of nine) DPC signals in a least-square sense (see text). The error from the model distribution is shown in (d), which demonstrates that the model distribution is obtained without influenced by added noise.

itself. Here, we use the following attribute of integration of the DPC signal: When the relationship between the coordinate systems is correct, the differential of the integration of the DPC signal should reproduce the original DPC signal. Contrary, if the relationship between the coordinate systems is not correct, the integration of the DPC signal will not be performed correctly, and thus the differential of the phase distribution will not reproduce the original DPC signal. Using this property, we rotate the observed DPC signal as a vector, integrate the rotated signal to obtain the phase distribution, and differentiate the phase distribution to obtain an emulated DPC signal. Finally, we calculate the sum of squared difference (SSD) between the emulated and the original DPC signals. Since the differential of the integrated signal returns to the original signal at the correct rotation angle for a noiseless data, the angle that minimizes the SSD would indicate the rotation angle for the real-world data (See **Fig. 6**).

SD module

The qDPC has the optional on-line module, the SD module, where the signals from a segmented detector are acquired in real time using Gatan's DigiScan$^{\mathrm{TM}}$ II. Here, the phase distribution is obtained by using the real-time integration routine of the qDPC, and displayed according to the progress of the scan. Since the DigiScan$^{\mathrm{TM}}$ II is usually used to capture the BF and/or HAADF signals, we add DigiScan$^{\mathrm{TM}}$ II to collect the signals from the segmented detector and transferred them in live to DigitalMicrograph® as shown in **Fig. 5**. In the case of the SAAF Octa, which is a commercial double quadrant detector from JEOL, it is possible to acquire eight signals simultaneously using two DigiScan$^{\mathrm{TM}}$ II (Gatan Microscopy Suite® (GMS) 3.4 supports up to four DigiScan$^{\mathrm{TM}}$ II). Here, the DPC signals are synthesized from the signals captured into the DigitalMicrograph®, then they are integrated in real time, and a phase distribution is displayed in accord with the scanning (see **Fig. 10**). The phase distribution obtained by real-time integration makes it possible to evaluate the sample and experimental conditions in live mode, and thus we expect the SD module will substantially accelerate the experiment. It is also possible to obtain a more accurate phase distribution by the DCT integration just after the completion of scanning.

4D-STEM module

The qDPC has also another optional extension, the 4D-STEM module, for a pixelated detector. The 4D-STEM module has an offline function that calculates DPC signals from existing 4D-STEM data. Once the DPC signal is obtained from the 4D-STEM data, the phase distribution can be calculated offline using the qDPC function. The 4D-STEM module has also an online function that calculates DPC signals just after the completion of each scan, and obtains the phase distribution in quasi-real-time using the DCT. In the case of the 4DCanvas$^{\mathrm{TM}}$, a commercial pixelated detector of JEOL, the DPC signals become available immediately after the completion of scanning, and there is no need to calculate the DPC signal from 4D-STEM data. Therefore, a high-precision phase distribution can be obtained by the DCT integration just after the scanning, which makes it possible to judge the sample and experimental conditions, and thus greatly facilitates the experiment.

Results and Discussion

Up to now, the integration method of the DPC signal has been studied with a model structure. Here, we compare the DCT and FFT integration of the ideal DPC signal, which is obtained as the centroid of the diffraction intensity acquired with a pixelated detector, namely the 4DCanvas$^{\mathrm{TM}}$ provided by JEOL. The 4D-STEM data used here is obtained from single-layer graphene observed at 80 kV by 4DCanvas$^{\mathrm{TM}}$ attached to a JEOL JEM-ARM200F, and the number of pixels is 256 × 256. Figs. 6 (a) and (b) show the DPC signals (the centroid of the diffraction intensity) calculated from the 4D-STEM data in the camera coordinate system. The DPC signals in (c) and (d) are obtained by rotating the raw DPC signals, (a) and (b), by 31 degrees using the function of the qDPC mentioned above. The phase distributions obtained by the DCT and the FFT-2 using the DPC signal after rotation correction are shown in (e) and (f), respectively. By comparison between the two, it can be seen that the remarkable difference appears in the upper right corner of the phase distributions. In this example, unfortunately multilayer graphene is present at three corners except the upper right of the observation area. Therefore, the periodic boundary condition assumed in the FFT breaks down considerably, and a false image contrast appears at the upper right corner in FFT-

Fig. 5 SD module

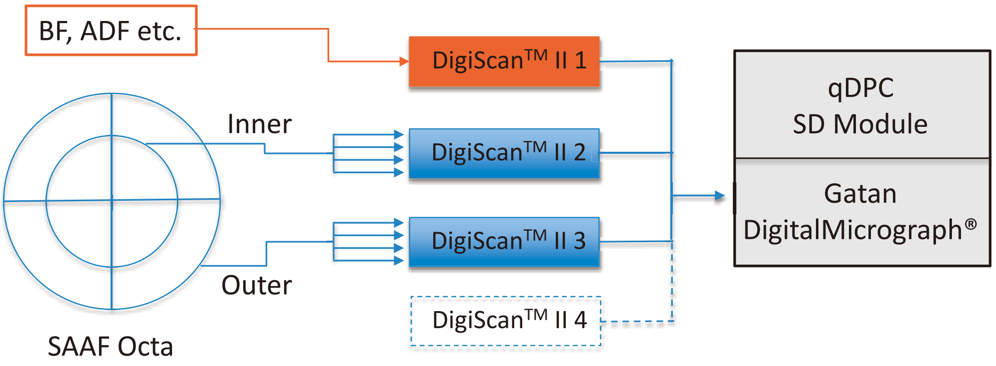

The signals from the segmented detector are taken into DigitalMicrograph® using multiple DigiScan$^{\mathrm{TM}}$ IIs (Gatan), and the DPC signals are synthesized. Then, the phase distribution obtained from of the DPC signals by real-time integration is displayed in accord with the scanning. In the case of SAAF Octa, a commercial segmented detector of JEOL, it is possible to acquire eight signals simultaneously using two DigiScan$^{\mathrm{TM}}$ II. (See Fig. 10).

2 (consult comparison with Ptychography in **Fig. 9**). Note that a clear six-membered ring like in (e) and (f) does not appear when the phase distribution is obtained from as-acquired DPC signals, (a) and (b).

Next, we compare the phase distributions reconstructed from the emulated DPC signals for the different segmented detectors using the same 4D-STEM data. **Figure 7** (a) and (b) show the phase distributions obtained by DCT from the DPC signals emulated for a quadrant and annular quadrant detectors, respectively. The both phase distributions are very similar to the one shown in Fig. 6 (e) obtained from the DPC signal estimated as the centroid of the diffraction intensity. The histograms of the phase distributions of Fig. 6 (e) and Figs. 7 (a) and (b) are shown in **Figs. 8** (a), (b) and (c), respectively. The histogram (c) obtained from the annular quadrant detector is very similar to the result (a) obtained from the pixelated detector. Figure 8 also shows correlation diagrams of the phase distributions of Figs. 7 (a) and (b) with respect to the phase distribution shown in Fig. 6 (e). The correlation diagram also demonstrates that the phase distribution of Fig. 7 (b) obtained from the annular quadrant detector is very close to the phase distribution of Fig. 6 (e) obtained from the pixelated detector. We may note that the phase change from single-layer graphene has been measured by electron holography as 50 ± 50 mrad [14]. The widths of the main peak of the histograms shown in Fig. 8 (a) and (c) are about 50 mrad, which closely corresponds to the result measured by electron holography. However, an atomic resolution phase distribution as obtained here is not reported in [14]. This seems to be because the DPC is more immune to quantum noise.

Now, the phase distribution obtained by using the DPC signal will be compared with the phase distribution obtained by Ptycography. Figure 9 (a) shows the phase distribution of single-layer graphene obtained by Ptychography from the same 4D-STEM data [15]. The phase distribution of Ptychography is close to the result of the DCT (Fig. 6 (e)), and the abnormal contrast as shown in the result of the FFT (Fig. 6 (f)) does not appear at the upper right. However, the DCT result shows a slight contrast change in the single-layer graphene region, and the contrast of the multilayer graphene regions is slightly different from the Ptychography result. Since the DCT or FFT integration includes a division by frequency during the processing, low frequencies are apt to be emphasized. Figure 9 (b) shows the phase distribution where the low frequency is slightly attenuated from the DCT result, which becomes closer to the one obtained by Ptychography. We have already confirmed that the phase distributions obtained from the DPC signals corresponding to the segmented detectors (Fig. 7) are similar to the phase distribution obtained from the DPC signal estimated from the pixelated detector (Fig. 6 (e)). Therefore, it has been demonstrated that the phase distribution that is used for a practical application can be obtained by integrating the DPC signal from the segmented detector. As introduced in the next section, the phase distribution can be observed in live mode by using the DPC signal from the segmented detector. Contrary, Ptychography is not suitable to obtain the phase distribution in real-time, since it requires a two-dimensional Fourier transform at each diffraction point of the 4D-STEM data [9].

Finally, we will show the SD module applied to JEOL SAAF Octa, where the phase is displayed according to the scan as described in the section for the real time integration method. Figure 10 is a screenshot at the time the SD module is operating, where the sample is STO [$SrTiO_3$]. The upper part

Fig. 6 Phase distributions restored from the DPC signal obtained from the pixelated detector

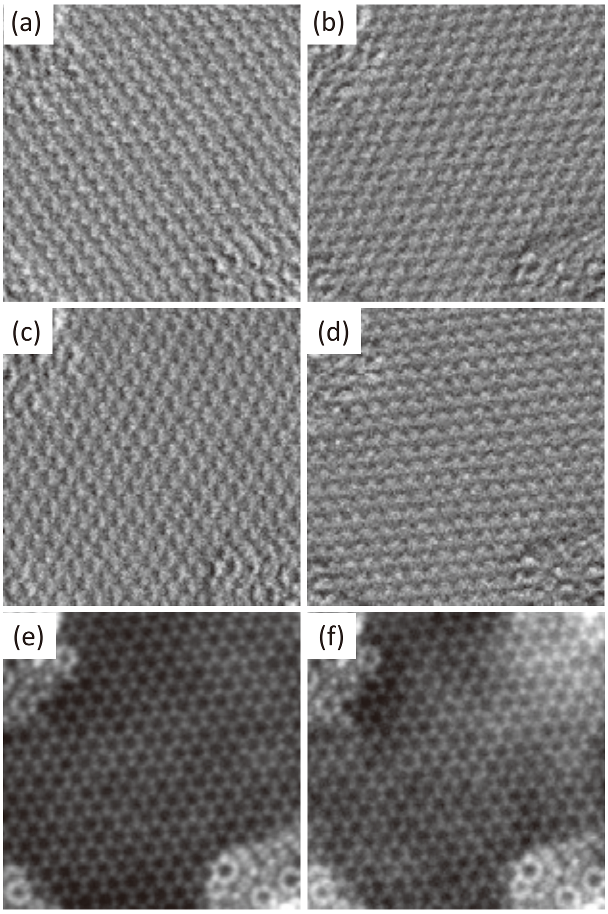

The integration methods were compared using an ideal DPC signal obtained as the centroid of the diffraction intensity of 4D-STEM data. The sample was single-layer graphene, and 4D-STEM data was acquired by 4DCanvas™ mounted on JEM-ARM200F. Top (a and b): DPC signals in two directions calculated from the 4D-STEM data in the camera coordinate system. Middle (c and d): DPC signals in the scanning direction, where the DPC signals are rotated by 31 degrees using the DPC signal correction function. Bottom (e and f): Phase distributions obtained by DCT and FFT-2, respectively, from the rotated DPC signals. A remarkable difference between two phases appears in the upper right, which result from the failure of the periodic boundary condition assumed by FFT (cf. Fig. 9).
Experimental conditions: JEM-ARM200F (acceleration voltage 80 kV, magnification 50M), 4DCanvas™ (264 × 66 pixels (binning 4), 4,000 fps), number of scan points 256 × 256, data acquisition time 16s.

Fig. 7 Phase distributions obtained from the DPC signals emulated for the segmented detectors

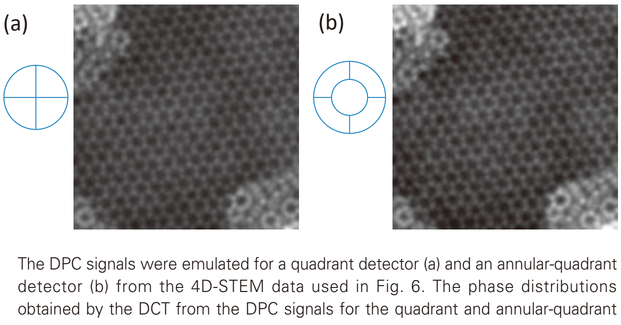

The DPC signals were emulated for a quadrant detector (a) and an annular-quadrant detector (b) from the 4D-STEM data used in Fig. 6. The phase distributions obtained by the DCT from the DPC signals for the quadrant and annular-quadrant detectors are very close to the phase distribution shown in Fig. 6 (e).

displays four signals from the inner or outer quadrant detector, and the lower part from the left corresponds to two synthesized DPC signals, a phase distribution integrated in real time, a simultaneously acquired HAADF image, and an electric field map in color display mode. Although no contrast is visible at the position of oxygen in the HAADF image, contrast from oxygen appears in the DPC signal, phase distribution, and electric field map. The electric field vector here uses the derivative of the phase distribution instead of the observed DPC signal. Therefore, the random noise in this electric field map is reduced compared to the case where the observed DPC signal is displayed. This is because the influence of random noise included in the observed DPC signal is suppressed by the integration as described before. Although this real-time integration can be done in live, the integrated phase is an approximate solution, and does not simultaneously satisfy the entire DPC signal contrary to the solution of the DCT. Nevertheless, the real-time integration will accelerate the experiment significantly, since it gives a sufficiently accurate phase distribution, from which the sample and experimental conditions can be safely evaluated.

Fig. 8 Comparison of phase distributions obtained from the DPC signals of various detectors

(a) Pixel

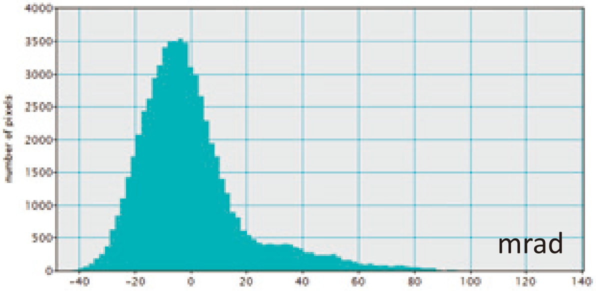

(b) Split

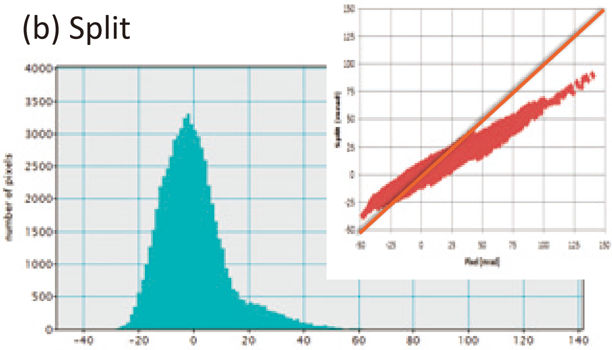

(c) Annular Split

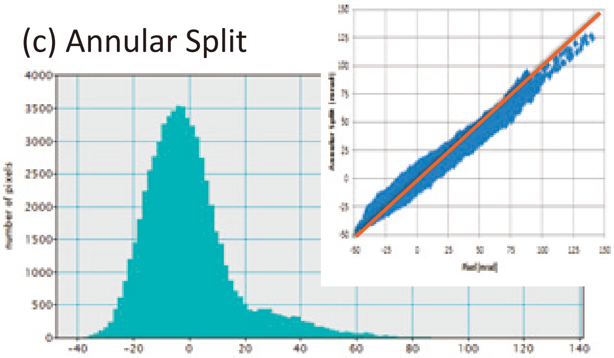

(a): Histogram of the phase distribution of Fig. 6 (e). (b) and (c): Histograms of the phase distributions of Figs. 7 (a) and (b), respectively, where the correlation diagrams with the phase distribution of Fig. 6 (e) are also shown. The histogram and correlation diagram demonstrate that the phase distribution of the annular quadrant detector is close to that of the pixelated detector. The horizontal axis of the phase histogram is mrad.

In Conclusion

Differential phase contrast (DPC) using a two-segment (split) detector has been proposed as a method of observing a phase object in scanning transmission electron microscopy (STEM). From the DPC signal we can obtain the phase distribution, since the DPC signal is a derivative of the phase distribution. In this report, we introduced the discrete cosine transform (DCT) as a method of integration to obtain the phase distribution using the Neumann boundary condition, which is not affected by the boundary of data acquired in a finite interval in contrast to the method based on the fast Fourier transform (FFT) that uses a periodic boundary condition. We also described the real-time integration method that displays the phase in accord with the scanning of the STEM. Then, we examined the phase distributions obtained by DCT from the DPC signals emulated for the segmented detectors using experimental data of single-layer graphene obtained by a pixelated detector, 4DCanvas^{TM}. In addition, we compared the phase distribution obtained by DPC with the one obtained by Ptychography, and demonstrated that the segmented detector provides a phase distribution that can be used for a practical application. The phase distribution can be observed in real time by using the DPC signal from a segmented detector, while Ptychography is not suitable for real-time application, since it requires a large

Fig. 9 Comparison of the phase distributions obtained by Ptychography and DPC integration

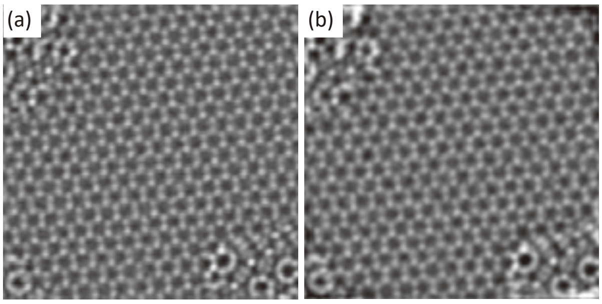

Processed by R. Sagawa (JEOL)

(a): Phase distribution of single-layer graphene obtained by Ptychography. (b): Phase distribution obtained by slightly attenuating low frequencies of Fig. 6 (e). The distribution especially at multilayer graphene regions becomes more similar to (a). This demonstrates that a practically acceptable phase distribution can be obtained using the DPC signal from a segmented detector.

Fig. 10 SD module

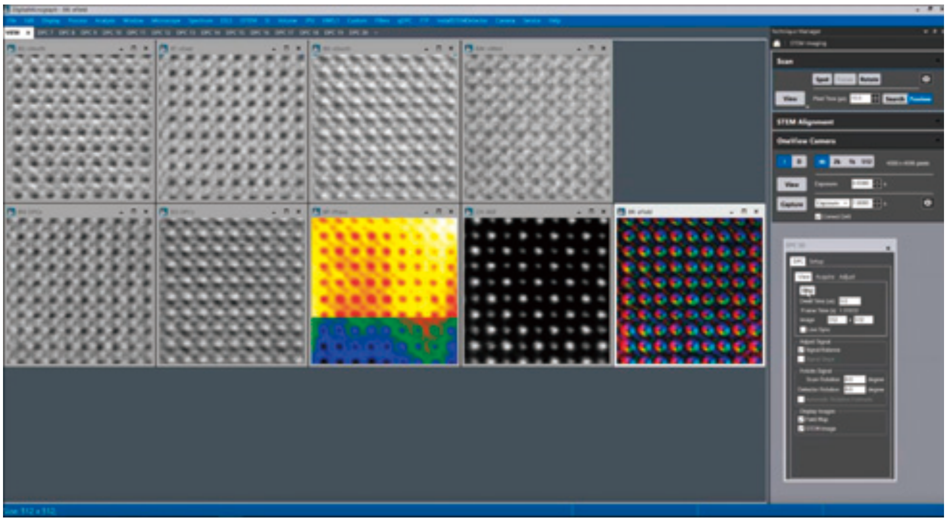

Screenshot showing the SD module in action, where the upper row shows four signals from the inner or outer quadrant detector, while the lower row (from left) shows two synthesized DPC signals, a real-time integrated phase, a HAADF image acquired simultaneously, and an electric field map displayed in color mode. The SD module palette is shown in the right. Pressing the Start button updates these images in accord with the DigiScan™ signal data update. Here, the sample is STO [SrTiO$_3$], and no contrast is seen at the oxygen position in the HAADF image, while some contrast appears in the DPC signal, phase distribution, and electric field map. Since the electric field map here is obtained by differentiating the phase distribution, random noise is reduced compared with the electric field map created by using the observed DPC signal.

amount of calculation. We introduced also the SD module that acquires the signal from a segmented detector, such as SAAF Octa, using Gatan's DigiScan™ II, calculates the DPC signals and displays the phase distribution in live mode. Furthermore, we introduced the 4D-STEM module that displays the phase distribution from the 4D-STEM data in quasi-real-time, namely immediately after the end of scanning. We expect that these online modules will accelerate DPC observation in STEM.

Finally, we have been providing a suite of plug-ins of DigitalMicrograph® (Gatan) for quantitative analysis for electron microscopy. Some of them were introduced in JEOL News [16]. We would be grateful if you could look though it also.

Acknowledgements

The authors would like to express their gratitude to Mr. Onishi and Mr. Okunishi of JEOL for evaluation of the SD module at SAAF Octa, and Mr. Sagawa, Mr. Hashiguchi, and Mr. Yasuhara of JEOL for testing the 4DCanvas™ module. In addition, Mr. Sagawa has kindly provided the raw data of single-layer graphene obtained by 4DCanvas™ and the phase image reconstructed by Ptychography. We also acknowledge JEOL for providing the opportunity to write this article.

References

[1] Okunishi E., Sawada H., and Kondo Y. (2012) Experimental study of annular bright field (ABF) imaging using aberration-corrected scanning transmission electron microscopy (STEM). *Micron*, **43**, 538-544.

[2] Dekkers N. H. and de Lang H. (1974) Differential phase contrast in a STEM. *Optik* **41**, 452-456.

[3] Waddell E.M. and Chapman J.N. (1979) Linear imaging of strong phase objects using asymmetrical detectors in STEM. *Optik* **54**, 83-96.

[4] Rose H. (1977) Nonstandard imaging methods in electron microscopy. *Ultramicroscopy* **2**, 251-267.

[5] Shibata N., Findlay S.D., Kohno Y., et al. (2012) Differential phase-contrast microscopy at atomic resolution. *Nat. Phys*. **8**, 611-615.

[6] Chapman J.N., Batson P.E., Waddell E.M. and Ferrier R.P. (1978) The direct determination of magnetic domain wall profiles by differential phase contrast electron microscopy. *Ultramicroscopy* **3**, 203-214.

[7] McGrouther D., Benitez M-J., McFadzean S., and McVitie S. (2014) Development of Aberration Corrected Differential Phase Contrast (DPC) STEM. *JEOL News* **49**, 2-10.

[8] qDPC, a DigitalMicrograph plug-in:
https://www.hremresearch.com/Eng/plugin/qDPCEng.html

[9] Pennycook T.J., Lupini A.R., Yang H., Murfitt M.F., Jones L., Nellist P.D. (2015) Efficient phase contrast imaging in STEM using a pixelated detector. Part 1: Experimental demonstration at atomic resolution. *Ultramicroscopy* **151**, 160–167.

[10] Close R., Chen Z., Shibata N. and Findlay S.D. (2015) Towards quantitative, atomic-resolution reconstruction of the electrostatic potential via differential phase contrast using electrons. *Ultramicroscopy* **159**, 124-137.

[11] Lazic I., Bosch E.G.T and Lazar S. (2016) Phase contrast STEM for thin samples: Integrated differential phase contrast. *Ultramicroscopy* **160**, 265-280.

[12] Press W.H., Teukolsky S.A., Vetterling W.T., Flannery B.P. (1988) Numerical Recipes, Cambridge Univ. Press, Cambridge.

[13] Ishizuka A., Oka M., Seki T., Shibata N., and Ishizuka K. (2017) Boundary-artifact-free determination of potential distribution from differential phase contrast signals. *Microscopy* **66**, 397-405.

[14] Cooper D., Pan CT., and Haigh S. (2014) Atomic resolution electrostatic potential mapping of graphene sheets by off-axis electron holography. *J. of Appl. Physics* **115,** 233709.

[15] Sagawa R. (2017) Development of Pixelated STEM Detector "4DCanvas". *JEOL News* **52**, 53-57.

[16] Ishizuka K. and Okunishi E. (2008) Quantitative Electron Microscopy Using Digital Data Processing. *JEOL News* **43**. 17-22.

Chemical State Analysis of Light Elements in Nuclear Fission and Fusion Reactor Materials by Soft X-ray Emission Spectroscopy in Electron Probe Microanalyzer

Ryuta Kasada[1], Keisuke Mukai[2]

[1] Institute for Materials Research, Tohoku University

[2] Institute of Advanced Energy, Kyoto University

Chemical states of light elements such as lithium, beryllium, boron and carbon, which play important roles in materials used in nuclear fission and fusion reactors, were analyzed by electron probe microanalyzer (EPMA) with soft X-ray emission spectroscopy (SXES). The high energy resolution and high sensitivity of EPMA-SXES enabled us to clarify the role of light elements in the functions and degradation behavior in lithium-lead eutectic alloy, beryllides and boron carbide.

Introduction

Light elements such as lithium (Li), beryllium (Be), boron (B), and carbon (C) which have characteristic nuclear properties, have been used in various core components of nuclear fission reactors and future fusion reactors. Since these nuclear components are required to be resistant to the extreme environments, it has been a great concern to understand the chemical state of the light elements. The soft X-ray emission spectroscopy (SXES) device developed by Terauchi et al. [1] and commercially installed to an electron probe micro-analyzer (EPMA) [2] enables us to obtain the fine structure of soft X-ray emission spectrum with the difference in the state of chemical bonding and further chemical state map, which were difficult with conventional WDS (wavelength dispersive X-ray emission spectroscopy).

Our research target is to clarify the role of light elements in the function or degradation of the nuclear and fusion reactor materials. This report focuses on our recent results of lithium (Li), beryllium (Be), boron (B), and carbon (C) in the nuclear materials obtained by EPMA-SXES which is a JEOL JXA-8500F field emission (FE) electron probe microanalyzer (FE-EPMA) equipped with the SXES device.

Li: Lithium distribution in lithium-lead eutectic alloys

Major concepts of future fusion reactor being developed around the world will use hydrogen isotopes, such as deuterium and tritium, as fuel of nuclear fusion reaction. The neutrons produced by fusion reaction are used for tritium-breeding through nuclear reactions with Li atom, which is placed in breeding blankets around the reactor core because the natural abundance of tritium is very small. Among the several breeding blanket concepts, liquid metal blanket concepts adopt a simple substance Li or Li-Pb eutectic alloy for the tritium-breeding. One of the engineering issues of Li-Pb usage is surface oxidation of ingots during storage, which may affect the subsequent physical property measurements and corrosion tests with structural materials as liquid metal. Conventional X-ray emission spectroscopy for EMPA is not available for Li because of the following difficulties: the weight concentration of Li in Pb-17at% Li eutectic alloy is only 0.65wt%, the number of valence electron in Li is only 1, oxidation of Li reduces the number of valence electron, and the emission energy of Li-K is quite low. As shown in **Fig. 1**, however, EPMA-SXES using JS50XL diffraction grating successfully detected the Li-K satellite emission peak (47-51 eV) derived from the Li oxide formed on the surface of ingot. Furthermore, a chemical map analysis by EPMA-SXES revealed that the distribution of Li oxide was not homogeneous on the surface of ingot. This result suggests that during the solidification process or storage period of the ingot, the surface oxidation of the Li-enriched phase formed by the separation of Li and Pb would be progressed and then concentrated Li was oxidized. Based on this finding, we also succeeded in the chemical state analysis of Li in the structural materials after corrosion tests in liquid Li-Pb eutectic alloy [3].

›› 2-1-1 Katahira, Aoba-ku, Sendai 980-8577, Japan | E-mail: r-kasada@imr.tohoku.ac.jp

Fig. 1

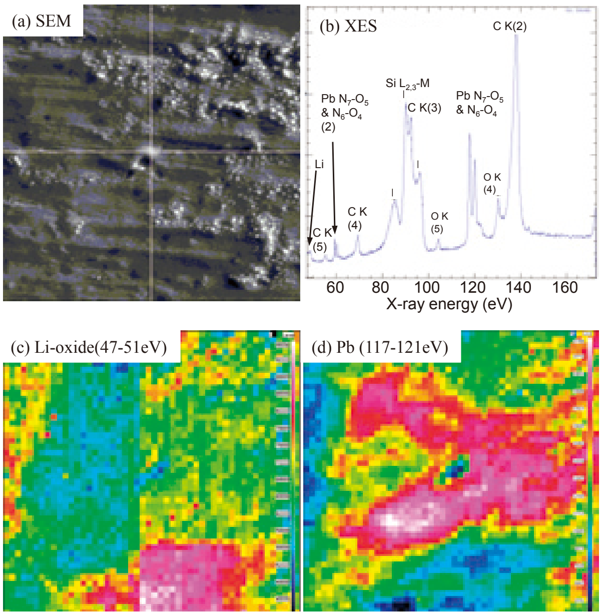

(a) Scanning electron micrograph of the surface of Pb-17at%Li ingot after storage in air, (b) X-ray emission spectrum obtained by EPMA-SXES at the center of (a), and X-ray emission map images of (c) Li-oxide obtained from a range of 47-51 eV, and (d) Pb obtained from a range of 117-121 eV including the emission peaks of N_7-$O_5$and N_6-$O_4$of Pb.

Be: Chemical bonding state analysis of beryllium in beryllide

As shown in the previous section, one tritium is produced from one Li with one neutron generated from one fusion reaction of deuterium and tritium. However, fusion neutrons are absorbed by structural materials other than Li in blanket. To avoid depletion of tritium as fuel, Be, which enables the neutron multiplication reaction (two neutrons are generated from one Be by absorbing one neutron), may be placed together with Li in the blanket. In order to achieve further safety even in the event of cooling water leakage inside the blanket, beryllides such as $Be_{12}Ti$ and $Be_{12}V$ has been developed because of their excellent high temperature steam oxidation resistance compared with a simple Be. To clarify the mechanism of their resistance to the oxidation and to develop further superior resistant beryllides, we preformed the valence state analysis by combining EPMA-SXES and DFT calculations of beryllides. **Figure 2** shows the Be-K emission spectra from a simple Be obtained by EPMA-SXES (JS200L) and conventional EPMA-WDS (LDE3H). In EPMA-SXES, the structure of the Be-K emission spectrum well reflects the partial density of state near the Fermi edge of Be. Furthermore, as shown in **Fig. 3**, in beryllium oxide (BeO), while the X-ray emission intensity decreased, the chemical shift and satellite peak of Be-K can be clearly identified. Based on these reference data, the chemical state map analysis of the oxide film after the oxidation test became possible [4]. **Figure 4** shows the Be-K emission spectra obtained by EPMA-SXES at different accelerating voltages for $Be_{12}V$ beryllide containing other minor phases such as Be_2V, Be and V phases. It is noticed that at an acceleration voltage of 5 kV, V-Ll emission peak are not seen but at an acceleration voltage of 15 kV that is excited near the higher energy side of the Be-K emission spectrum. In addition, the shape of the Be-K spectrum of beryllides agrees well with the 2p partial density of states of Be obtained by DFT calculation, and the structure of the Be valence band is changed by hybridization with the valence orbital of V. Also, EPMA-SXES has successfully showed that the V phase, where the conventional EPMA-WDS could detect V only, contains a small amount of Be with the same Be-K emission spectrum shape as the beryllide phase. We believe that such a combination of chemical state analysis by EPMA-SXES and DFT calculation can contribute to the development of superior beryllide.

B and C: Chemical state map analysis of boron and carbon in a simulated boron carbide control rod after high-temperature steam oxidation test

Control rods are used in nuclear fission reactors to achieve continuous fission reactions. The control rod in commercial boiling water reactors, including the Fukushima Daiichi Nuclear Power Station, contains boron carbide (B_4C) as neutron

Fig. 2

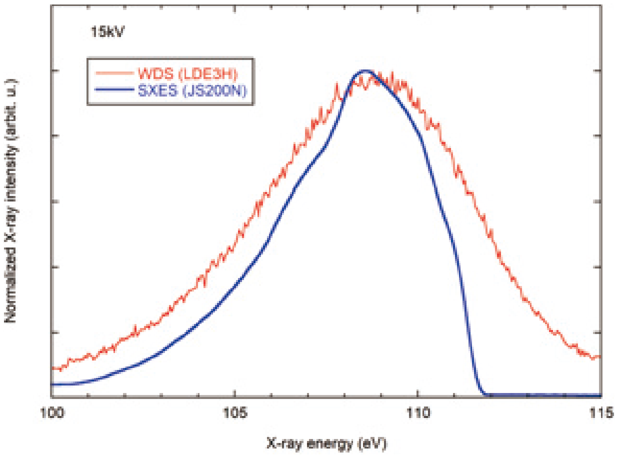

Comparison of normalized B-K spectra obtained by EPMA-WDS using LDE3H and EPMA-SXES using JS200N as spectrometer.

Fig. 3

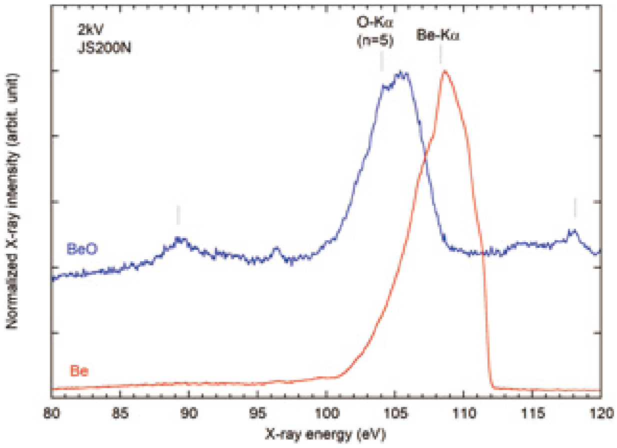

Normalized B-K spectra of Be and BeO obtained by EPMA-SXES.

absorbing material. Despite of the high melting point over 2400 °C, B_4C molt and then formed debris through eutectic reactions with metals in the surrounding stainless steel at about 1150 °C during severe accident. High-temperature steam oxidation reaction is also possible. Through these reactions, B can have various chemical forms and their mixture, which affect the types and amounts of radioactive sources released into the environment. In addition, understanding the location and chemical state of boron that absorbs neutrons well in debris are very important for further reducing the recriticality risk during the decommissioning process. In this study, EPMA-SXES analysis was performed on a B_4C control rod simulated sample after high-temperature steam oxidation test for 30 min at 1250 °C [5].

Figure 5 shows the B-K X-ray emission spectra obtained by EPMA-SXES for boron (B) and compounds containing B. B_4C shows a characteristic peak shape different from that of a simple B. Transition metal borides such as FeB and Fe_2B have a shoulder (S2) at the high energy side of the emission spectra corresponding to the vicinity of the Fermi edge of B, reflecting the metallic bonding. Boron oxide (B_2O_3) shows a chemical shift toward lower energy and has satellite peaks at the lower energy side S1 and at the higher energy side S3. The higher-energy satellite peak S3 is attributed to X-ray resonance Raman scattering, and the lower-energy satellite peak S1 is due to the transition from B 2p electron or O 2s electron to B 1s hole.

Figure 6 shows the B-K emission spectra and chemical map analysis results obtained by EPMA-SXES for a cross-sectional sample of the B_4C control rod simulated test specimen after the high-temperature steam oxidation test. The granular region where the B concentration is high shows the same peak shape with B_4C shown in Fig. 6, corresponding to the remained B_4C particles. A peak shoulder peculiar to borides is observed at the points out of the remained B_4C particles. With considering the conventional EPMA-WDS results, borides of Fe, Cr, and Ni, which are the main components of stainless steel, were formed at the region by eutectic reaction. Here, by calculating the areal ratios of the peaks P_B/P_A and P_C/P_A, where P_A is the total area of B-K in the range 178–188 eV, P_B is the area in 178–186 eV and P_C is the area in 186–188 eV, the chemical state maps shown in Fig. 6(e, f) display the existing areas of B_4C and borides separately.

Figure 7 shows the C-K emission spectra and the corresponding carbon (C) element map at the same observation position of Figure 6, together with those of graphite and B_4C as reference. The inside of the remained B_4C particle has a similar C-K spectrum shape to the reference B_4C. In contrast, the outside of the residual B_4C particle has a C-K spectrum shape close to graphite. This implies that C as the resultant element of the eutectic reaction between B in B_4C and metals in stainless steel exists as graphite as surrounding the remained B_4C.

Thus, in addition to the elemental analysis and microstructure observation at the micro- and macro-scales, which is the conventional function of EPMA, chemical state analysis by EPMA-SXES revealed the complex structure of simulated B_4C control rod after a severe accidental condition.

Conclusion

The EPMA-SXES enables us to detect soft X-ray emission of light elements in nuclear materials with high-energy resolution and sensitivity. The obtained emission spectra of Li-K, Be-K, B-K, and C-K well reflected the valence electronic structure of the corresponding chemical states of light elements in Li-Pb, beryllides and B_4C. These results were also used for

Fig. 4

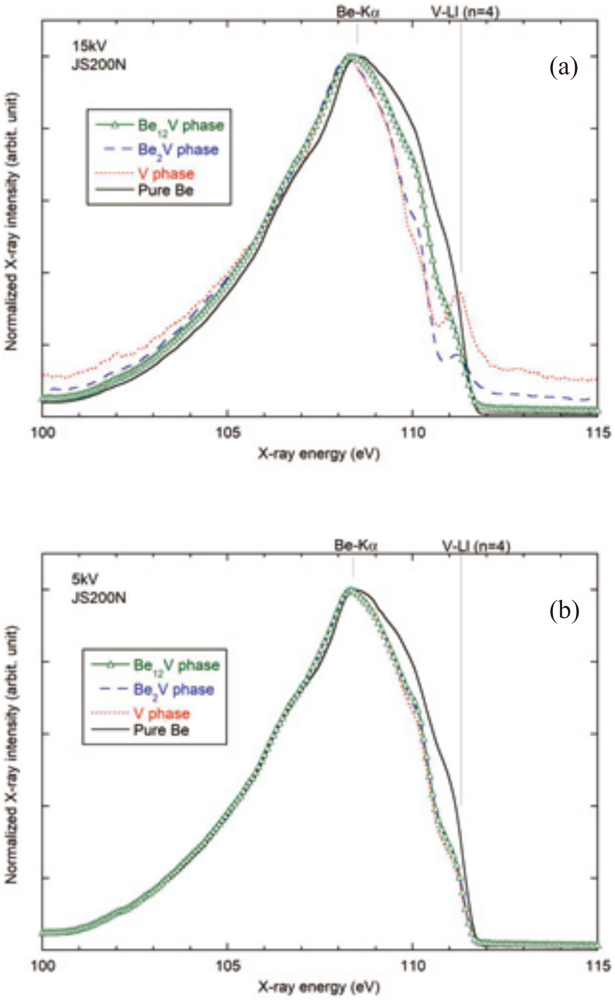

Be-K emission spectrum (normalized by peak value) obtained by EPMA-SXES for each of $Be_{12}V$, Be_2V, and V phases found in Be-V alloy. (a) and (b) were obtained at acceleration voltages of 15 kV and 5 kV, respectively. For comparison, Be-K emission spectrum obtained from a single Be sample (Pure Be) is also shown.

Fig. 5

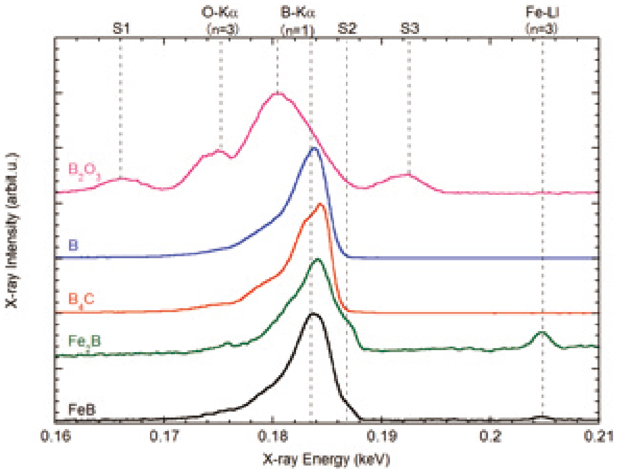

Normalized B-K emission spectra obtained by EPMA-SXES for a simple boron and boron compounds such as B_2O_3, B_4C, Fe_2B and FeB.

Fig. 6

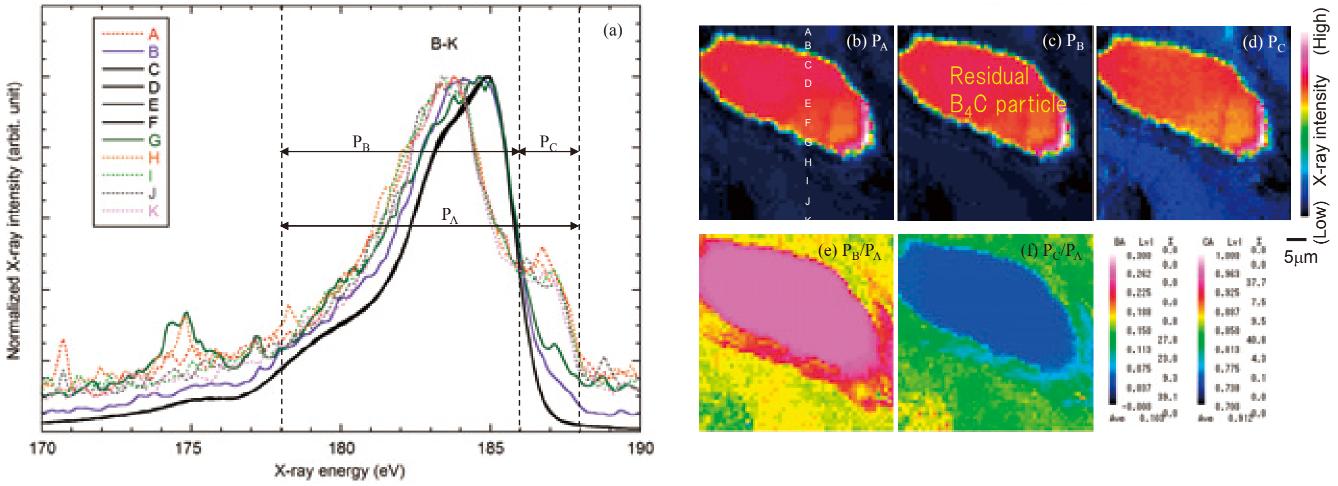

Elemental maps based on (a) P_A, (b) P_B and (c) P_C of (d) B-K spectrum, obtained by EPMA-SXES and chemical state maps calculated by peak-area ratio as (e) P_B/P_A and (f) P_C/P_A, around the residual B_4C grains of the control rod simulated material after high temperature steam oxidation test.

Fig. 7

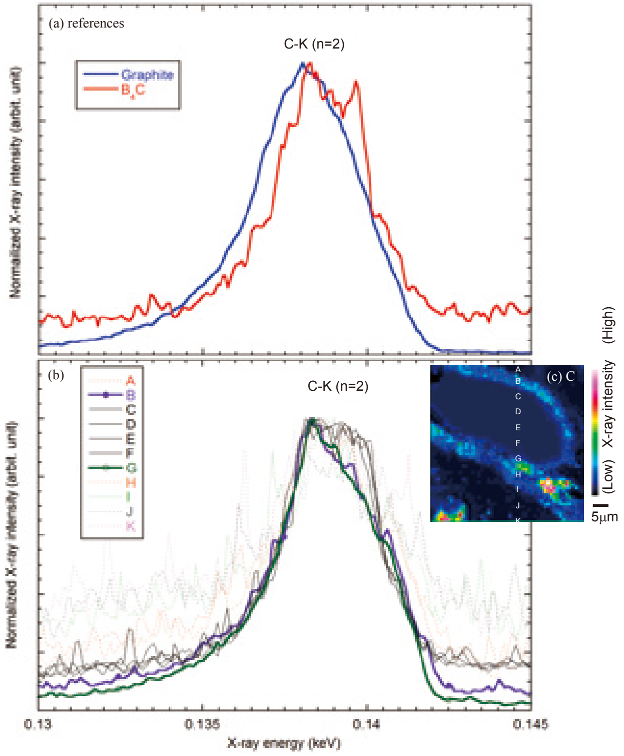

(a) C-K emission spectra (n = 2) of reference graphite and B_4C. (b) C-K emission spectra (n = 2) and (b) carbon concentration map at the same position as Fig. 6.

chemical state map analysis to understand their micro-scale local degradation with taking advantage of high availability of electron microscopes that cannot be achieved with other devices. Complementary use of the EPMA-SXES with the next-generation synchrotron radiation facility currently under construction will promise for the development of new functional materials and elucidation of the mechanism of material degradation.

Acknowledgments

The present studies were partly supported by the Zero Emission Energy Research Center (ZE), Institute of Advanced Energy (IEA), Kyoto University. In this framework, the authors cooperated with Prof. Satoshi Konishi, Dr. Changho Park, Dr. Kiyohiro Yabuuchi, Dr. Yoosung Ha of IAE; Dr. Takashi Nozawa, Dr. Masaru Nakamichi, Dr. Jaehwan Kim of the Institute for Quantum Science and Technology; and Dr. Hiroshi Sakamoto and Toru Higuchi of Japan Nuclear Fuel Development Co., Ltd.

References

[1] Masami Terauchi et al., "A New WDS Spectrometer for Valence Electron Spectroscopy Based on Electron Microscopy", *JEOL News* **47** (2012) 23-28.

[2] Hideyuki Takahashi et al., "Characteristic Features and Applications of a Newly Developed Wavelength Dispersive Soft X-ray Emission Spectrometer for Electron Probe X-ray Microanalyzers and Scanning Electron Microscopes", *JEOL News* **49** (2014) 73-80.

[3] ChangHo Park, Takashi Nozawa, Ryuta Kasada, Silvano Tosti, Satoshi Konishi, Hiroyasu Tanigawa, "The effect of wall flow velocity on compatibility of high-purity SiC materials with liquid Pb-Li alloy by rotating disc testing for 3000 h up to 900 °C", *Fusion Engineering and Design*, Volume **136**, Part A, 2018, Pages 623-627.

[4] Keisuke Mukai, Ryuta Kasada, Kiyohiro Yabuuchi, Satoshi Konishi, Jae-Hwan Kim, and Masaru. Nakamichi, "Valence Electron and Chemical State Analysis of Be12M (M = Ti, V) Beryllides by Soft X-ray Emission Spectroscopy", *ACS Applied Energy Materials*, 2019, **2** (4), 2889-2895.

[5] Ryuta Kasada, Yoosung Ha, Toru Higuchi, Kan Sakamoto, "Chemical State Mapping of Degraded B_4C Control Rod Investigated with Soft X-ray Emission Spectrometer in Electron Probe Micro-analysis", Scientific Reports 6, Article number: 25700 (2016).

Practical Workflow of CLEM – Trace of climbing fiber in cerebellar cortex of mouse –

Mitsuo Suga[1, 2], Hideo Nishioka[1, 2], Kohki Konishi[2, 3], Akira Takebe[2],
Eriko Miura[4], Keiko Matsuda[4], Michisuke Yuzaki[4]

[1] JEOL Ltd. [2] JEOL-Nikon CLEM Solution Center [3] Research and Development Division, Nikon Corporation
[4] Department of Neurophysiology, Keio University School of Medicine

Correlative light and electron microscopy (CLEM) is used to image the same position of a sample using light and electron microscopy. Light microscopy (LM) is used to identify the specific positions of interest with fluorescent markers, and electron microscopy (EM) provides the fine structures of the positions. In this study, we demonstrate a practical method for applying CLEM to the visualization of the fine structures of a climbing fiber (CF) in the cerebellar cortex of a mouse. A mouse genetically labeled with a fluorescent protein for CFs was fixed, and thick slices of its brain were imaged using confocal microscopy. The sample was further fixed with OsO_4, dehydrated, and embedded in an epoxy resin. The position imaged using LM was then trimmed, and serial sections of 45 nm in thickness were cut using an ultramicrotome. The sections were further imaged by array tomography using scanning EM (SEM), and the SEM images were analyzed including deep learning (DL). Three-dimensional (3D) reconstructed CF of the cerebellar cortex of a mouse was around the dendrite with complex branches. The positions of the boutons in the reconstructed CF corresponded well with those in the LM images, indicating that the CF observed by LM was unambiguously identified and traced by the CLEM.

Introduction

Correlative light and electron microscopy (CLEM) is used to image the same position of a sample by light and electron microscopy. CLEM is widely applied in industry, materials science, and bioscience because it improves the efficiency and provides new value by combining features of light microscopy (LM) and electron microscopy (EM) in a comprehensive manner. In industry and materials science, a foreign material is first found using LM. It is then observed using EM at high magnification, and its composition is analyzed through energy dispersive X-ray spectrometry (EDS). This process significantly improves the efficiency of the root cause analysis of the defects, and is widely applied in these fields. CLEM is becoming popular in bioscience because LM can identify the specific positions of proteins using fluorescent tags, and EM provides the fine structures of their positions [1-8].

A new trend has also appeared in bioscience using scanning EM (SEM). Because the resolution of cutting-edge SEM is better than 1 nm, contrast inverted backscattered-electron images obtained through SEM provide a similar resolution and contrast as those from a transmission EM (TEM). Automatic image acquisition is also realized by improving the automatic adjustments of the focus and stigma, as well as automatic control of the sample positions, based on improvements in computer technology. This allows SEM to be used to evaluate three-dimensional (3D) information by imaging the same positions for serial sections [9-11]. By combining 3D information obtained through SEM with confocal microscopy, 3D CLEM is also becoming a popular tool [12-14].

There are various methods for obtaining 3D information using SEM, such as focused ion beam (FIB)/SEM, serial block-face (SBF)/SEM containing ultramicrotome inside an SEM chamber, and array tomography [9-11]. Among these, array tomography, also called serial section SEM, has been widely used because, compared with SBF/SEM and FIB/SEM, array tomography has several advantages, namely, (a) a high lateral resolution; (b) wide-area imaging using a montage; (c) standard staining with uranium and lead, allowing easy comparison of images captured by SEM and TEM; (d) repetitive imaging of the samples, enabling a hierarchical analysis from low to high magnification; and (e) a low installation cost [15-18]. In particular, because wide-area imaging is possible, array tomography has been used to trace neurites in the brain, as described later [13, 19-21].

Although CLEM has been widely used as described above, various types of tips are required. Thus, the actual processes used in CLEM are described in this paper, using a trace of a climbing fiber (CF) as an example. CFs are axons of inferior

〉〉 3-1-2 Musashino, Akishima, Tokyo, 196-8558, Japan | E-mail: msuga@jeol.co.jp

olivary neurons, inducing motor learning in the cerebellum by sending teacher signals to a Purkinje cell [22]. In rodents, multiple CFs initially innervate a single Purkinje cell soma in the larva, but the “single-winner” CF translocates to the Purkinje cell dendrites at around P9, and the rest of the CFs remaining on the soma are eventually pruned by P21. It is known that cerebellar gait disorder and motor learning disorders are induced by abnormalities during the pruning process [23, 24]. The pruning process also occurs in places other than the cerebellum, and its abnormality induces various disorders in neurological functions, including developmental disorders such as autism spectrum disorder. Thus, as a model system, an accurate understanding of the CF pruning process is extremely important. Therefore, CLEM is applied using mice expressing fluorescent protein, yellow chameleon (YC), at inferior olivary neurons. First, the spreading pattern of a CF was imaged using a confocal microscope. Second, the same CF was identified by EM using CLEM. Third, the CF was traced using EM images of serial ultrathin sections. Deep learning (DL) was applied to improve the efficiency of the analysis for the EM images.

Actual workflow

Overview of the workflow

The CLEM workflow used in this study is shown in **Fig. 1**. There are various methods for applying CLEM to biological samples. In this study, after using confocal microscopy to provide optical slices of the sample, we embedded the sample into plastic, made serial ultrathin sections of 45 nm in thickness, and imaged the same position for each section using SEM. These processes provided LM and SEM images for the same position. To accomplish this, the various processes shown in Fig. 1 were used. The details of these processes are described in the following.

Sample and pre-treatment

Mice expressing fluorescent proteins (Htr5B-tTA; tetO-YC) [25, 26] were anesthetized with isoflurane, and were perfusion fixed using 2% glutaraldehyde (GA) and 4% paraformaldehyde (PFA) dissolved in phosphate buffered saline (PBS). After extracting the brains, the cerebellums were further fixed with the same fixation reagent for 12 h at 4 °C. After washing with PBS, thick slices of 100 μm were cut using a microslicer, and their nuclei were stained using 4', 6-diamidino-2-phenylindole (DAPI).

Imaging by LM

Fluorescent and transmission images were captured using an inverted confocal microscope (A1R, Nikon). To allow an identification of the captured positions after imaging, low-magnification, middle-magnification, and high-magnification images were captured. The following objective lenses were used: ×10 (NA 0.45) for low magnification, ×40 (NA 0.95) for middle magnification, and ×60 (NA 1.40) for high magnification. The laser unit was equipped with continuous wave lasers (405 nm for DAPI, 488 nm for YC). Fluorescence is filtered using the internal dichroics and band-pass filters (450/50 nm, 525/50 nm). For high-magnification imaging, the pixel size in the xy direction was 0.39 μm, z step was 0.2 μm, and 484 optical-slice images (z-stack images) were captured.

LM images of thick slices of the mouse cerebellar cortex are shown in Fig. 2. Images of the thick slices obtained using confocal microscopy after the initial fixations are shown in **Fig. 2** (a)–(d). Fig. 2 (a) shows a low-magnification fluorescent image, (b) shows a middle-magnification fluorescent image corresponding to a rectangle in (a), (c) shows a high-magnification fluorescent image corresponding to a rectangle in (b), and (d) shows a transmission image for the same field of view (FOV) of (c). Although 3D z-stacks were obtained using confocal microscopy, representative images of these stacks

Fig. 1 Workflow of correlative light and electron microscopy (CLEM) used in this study.

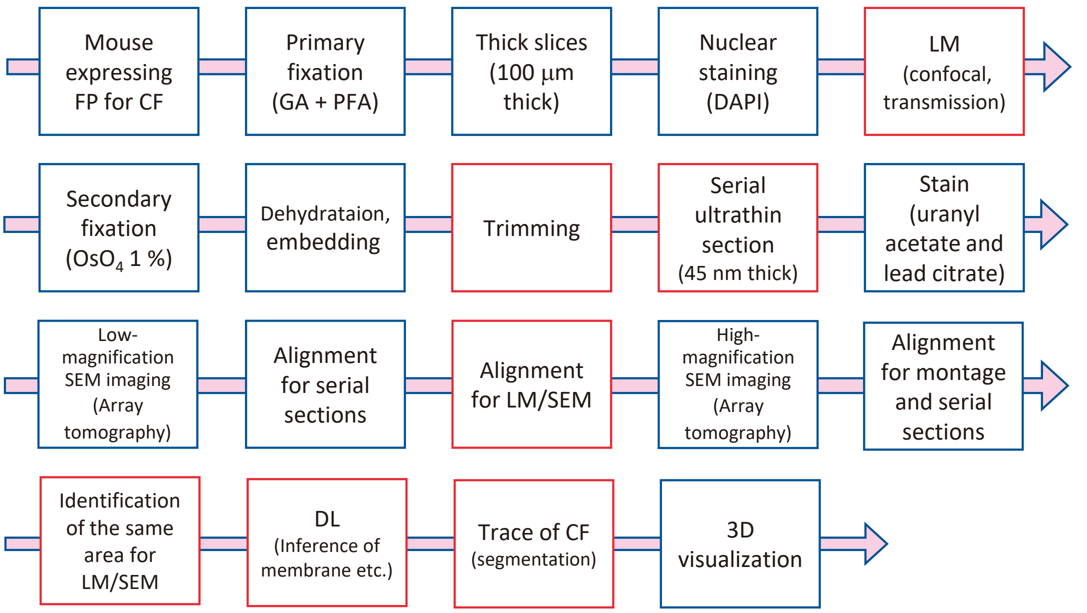

After applying confocal microscopy to provide optical slices of the sample, we embedded the sample into plastic, made serial ultrathin sections of 45 nm in thickness, and observed the same positions of the sections using SEM. These processes provided LM and SEM images for the same area. The CF was traced using these data.

are shown in Fig. 2 (a)–(d). In Fig. 2 (a)–(c), the green areas indicate CFs whereas the blue areas indicate the nuclei. The target CF by CLEM is indicated by the arrow in Fig. 2 (c), and a thick blood vessel is identified in the transmission image (arrow in Fig. 2 (d)).

Secondary fixation, dehydration, and embedding

Conventional sampling methods for TEM are applicable to these processes. After confocal microscopy, the thick samples were further fixed using 1% OsO_4 dissolved in PBS for 2 h at room temperature. After washing with water, the samples were dehydrated in a graded ethanol series later replaced with propylene oxide, and embedded in an epoxy resin (EPON812, TAAB).

Trimming

Stereomicroscopy images of the mouse cerebellar cortex after embedding are shown in Fig. 2 (e) and (f). The area of the CF in the cerebellar cortex remained, although some parts of the cortex were broken, as recognized by the comparison of the low-magnification (Fig. 2 (e)) and fluorescent (Fig. 2 (a)) images. Fig. 2 (f) shows an enlarged image of the rectangular area in Fig. 2 (e), indicating the same thick blood vessel (arrow in Fig. 2 (f)), as illustrated in Fig. 2 (d).

The target area including the CF was identified through comparisons of the fluorescent, transmission, and stereoscopic images (Fig. 2 (a)–(f)), and was marked with an oil-based magic pen. After a rough trimming with a razor, a precise trimming (320 μm × 320 μm) was applied using a trimming knife set on an ultramicrotome.

In the stereoscopic images of the embedded sample, only the surface information of the sample could be obtained, and no fluorescent information is available. Nevertheless, the target area in the embedded sample was roughly identified by evaluating the fluorescent images at low, middle, and high magnifications (Fig. 2 (a)–(c)) and the stereoscopic images (Fig. 2 (e), (f)) for the same region. In addition, the same thick blood vessel was identified in the transmission (arrow in Fig. 2 (d)) and the stereoscopic (arrow in Fig. 2 (f)) image. Using these processes, the target area can be unambiguously trimmed.

Serial ultrathin sections and post-staining

The trimmed block was sliced into serial ultrathin sections using an ultramicrotome (UC7, Leica), and the sections were mounted on silicon substrates cleaved to a size of approximately 8 mm × 50 mm (**Fig. 3** (b)). For easier mounting of the sections, a three-axis micromanipulator (M-152, Narishige) was used (Fig. 3 (a)). The silicon substrate was set at the leading edge of the arm and sunk in the water of the boat to mount the sections. The silicon substrates were cleaved again to a size of approximately 8 mm × 8 mm, while keeping the mounted area of the slices. The serial ultrathin sections were stained with uranyl acetate and lead citrate.

An LM image of the serial ultrathin sections on the silicon substrates is shown in Fig. 3 (b). Approximately 1,000 serial sections cut by an ultramicrotome were successfully mounted on the silicon substrates using the micromanipulator shown in Fig. 3 (a). The silicon substrates with the sections were stitched onto a stainless board shaped into a 3-inch wafer using double-sided tape, providing the effective handling of nearly 1,000 serial sections.

Low-magnification SEM imaging

An array supporter (JEOL), software specifically developed for automatic image acquisitions, was used for the array

Fig. 2 LM images of thick slices of the mouse cerebellar cortex.

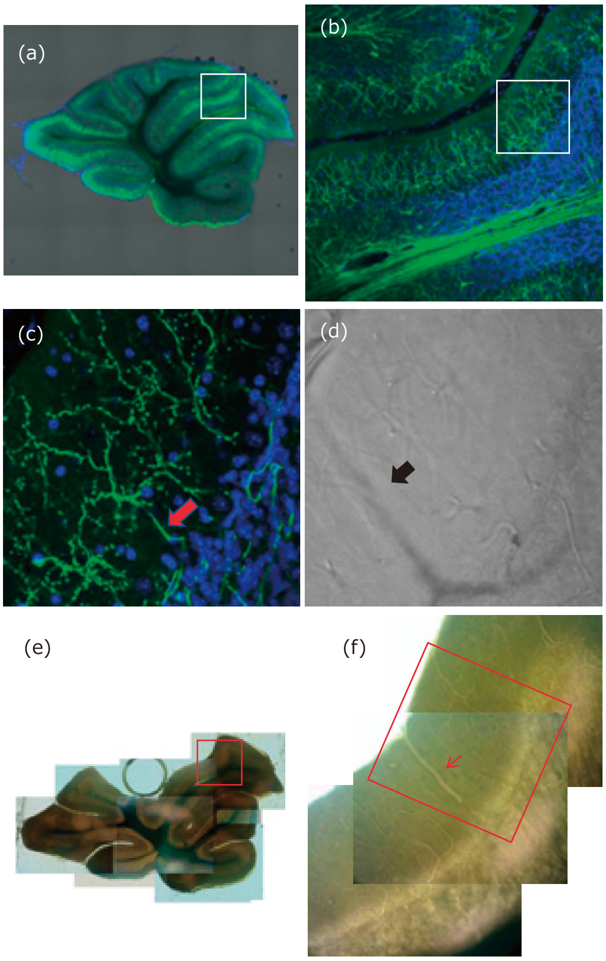

(a)–(d) Images from confocal microscopy for the thick slices after the initial fixations: (a) low-magnification fluorescent image, (b) a middle-magnification fluorescent image corresponding to the rectangle in (a), (c) a high-magnification fluorescent image corresponding to the rectangle in (b), (d) a transmission image for the same field of view (FOV) as in (c). Although 3D z-stacks were obtained using confocal microscopy, representative versions of these images are shown in (a)–(d). Green areas indicate CFs, whereas blue areas indicate nuclei in (a)–(c). Target CF by CLEM is indicated by an arrow in (c). (e), (f) Stereomicroscopy images of the mouse cerebellar cortex after embedding. The area of the CF in the cerebellar cortex remained, although some parts of the cortex were broken, as shown through a comparison of the low-magnification image in (e) and the fluorescent image in (a). Fig. 2 (f) shows an enlarged image of the rectangular area in (e), showing the same thick blood vessel (arrow in (f)) as shown in (d). The red rectangle in (f) indicates the area for trimming.

Fig. 3

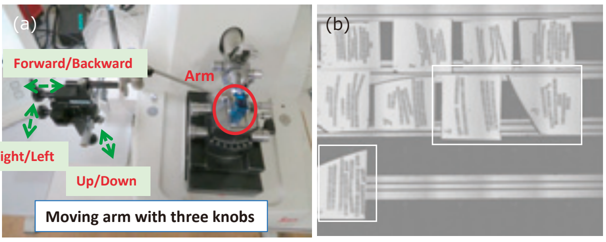

A manipulator and serial ultrathin sections. (a) A manipulator used to collect serial ultrathin sections on silicon substrates. (b) Approximately 1,000 sections placed on the silicon substrates using the manipulator. For SEM imaging, 311 sections in the white rectangles were used. The efficiency of the sample handling was improved by stitching the silicon substrates on a stainless-steel board shaped in a 3-inch wafer with double-sided tapes.

tomography. This software captures SEM images of each serial ultrathin section at the same position, using two corners of the section as the reference points of the position. The software also corrects the small displacement of the position and the differences in angles for the sections using image pattern matching for the adjacent sections. In addition, because an automatic multiple-image acquisition for the specified area is also realized, the array supporter allows wide area array tomography using a montage (composite image).

First, low-magnification (83 nm/pix) SEM images were automatically captured for 311 sections selected from all the sections. These SEM images are called z-stack images analogous to confocal microscopy. A montage was not applied for low-magnification SEM image acquisition, and only one image for each section was captured.

Alignment between adjacent sections

Alignments were needed for the low-magnification SEM images because there were slight displacements in the xy direction and variances in angle between the images of adjacent serial sections. Stacker (System in Frontier), linear stack alignment with SIFT (Fiji), and/or TrakEM2 (Fiji) were used for the alignment of 311 low-magnification SEM images.

Fig. 4 Images near the target CF.

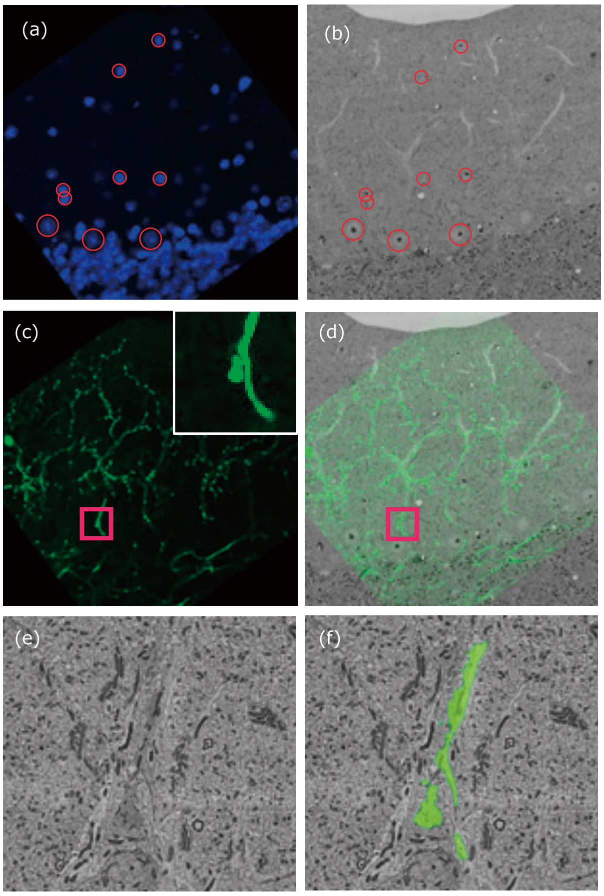

(a) Fluorescent image of nuclei. (b) a low-magnification SEM image. (c) fluorescent image of CF, where the insert shows an enlarged image corresponding to a rectangle. (d) overlay of the fluorescent image of CF (c) and a low-magnification SEM image of (b). (e) a high-resolution SEM image corresponding to a rectangle in (c). (f) the same SEM image in (e) with the CF painted in green.

Alignment of LM and Low-magnification SEM images

Fig. 4 shows the images near the target CF. Fig. 4 (a) shows a fluorescent image of the nuclei, (b) shows the low-magnification SEM image, and (c) shows a fluorescent image of the CFs. Here, the images in Fig. 4 (a) and (c) are rotated by 54° in the clockwise direction from those in Fig. 2 (a)–(d) for comparison with the low-magnification SEM images. Although the z-stack images were captured, only one representative image is shown in Fig. 4 (a)–(c).

The corresponding nuclei in the fluorescent (Fig. 4 (a)) and SEM (Fig. 4(b)) images are indicated by the red circles. As shown here, the corresponding nuclei were identified by comparing the z-stacks of the fluorescent images for the nuclei and low-magnification SEM images. The nuclei not shown in Fig. 4 were also identified by continuing the same comparisons.

The center positions of the corresponding nuclei were obtained visually for the LM and SEM images. In this procedure, orthogonal views showing the xy-, yz-, and zx-planes were used. The center positions of the corresponding nuclei for the LM and SEM images were fitted using the least squares method, and the LM and SEM images were aligned using the fitted parameters. Fig. 4 (d) shows the low-magnification SEM image overlaid on the fluorescent image of the CFs. From this overlay image, the approximate position of the target CF is known in the low-magnification SEM images.

High-magnification SEM imaging

Now, the area of the target CF is known, and high-magnification SEM images (6 nm/pix) were captured for the area. An array supporter was also used to capture the high-magnification SEM images for 311 serial ultrathin sections automatically, as used for the low-magnification SEM images. In this case, montage was used to evaluate the composite images with 32,000 × 32,000 pixels for each serial section.

The spreading area of the target CF was obtained through an overlay of fluorescent images of the CF placed on the low-magnification SEM images. Because high-magnification SEM images were captured only for this area, the image acquisition time and data processing time were significantly reduced, and the entire spreading area of the target CF was unambiguously imaged using high-magnification SEM.

Alignments for high-magnification SEM images (montage and adjacent sections)

The high-magnification SEM images for montage have small position displacements between adjacent images in the xy direction. To correct the displacements and composite the images, an array supporter (JEOL), Grid/Collection stitching (Fiji), and/or TrakEM2 (Fiji) were used. Displacements of the images for different sections were also aligned similar to the low-magnification SEM images.

Identification of the same area in LM and high-magnification SEM images

A special structure of the target CF, visible in the LM images and low-magnification SEM images, was searched to identify the target CF in the high-magnification SEM images. A special structure like a gourd, as shown in the inserted image in Fig. 4 (c) corresponding to the rectangle in Fig. 4 (c), was found. The high-resolution SEM images corresponding to the inserted image in Fig. 4 (c) are shown in Figs. 4 (e) and (f). Fig. 4 (e) shows the raw SEM image, whereas (f) shows the one overlaid on the green area indicating the target CF. As described here, the target CF was identified in the high-resolution SEM image by identifying the same special structure in both the LM and SEM images.

Inference of fine structures using DL

Tracing one specific CF requires tracing the CF cell membrane using high-magnification SEM images. A previously developed membrane tracing method utilizing DL, working with a small amount of training data, was used to improve the efficiency of tracing the membranes [27]. Because 311 high-magnification SEM images (6 nm/pix) with 32,000 × 32,000 pixels were obtained using montage, a huge computer is needed to process the images. Thus, division and binning were applied to calculate the images using a computer available in a typical laboratory. The specifications of the computer used in this work are as follows: a 3.7 GHz core i7-8700 K CPU (Intel), a GTX 1080 Ti GPU (NVIDIA), and 64 GB DRAM (Micron).

For inference of the cell membranes, high-magnification SEM images were divided into 16 images such that each divided image had 8,000 × 8,000 pixels. In addition, binning was applied such that the pixel size and number of pixels were 12 nm/pix and 4,000 × 4,000 pixels, respectively. From these images, areas of 512 × 512 pixels were cut and used as the training data. From the images with 512 × 512 pixels, 20 sets of ground truths were manually prepared (**Fig. 5** (a)). Using these SEM images and ground truth, the DL model was trained and applied to the high-magnification images binned to 12 nm/pix to infer the membranes. The results of inference were binarized using the Otsu method (Fiji).

Fig. 5 Workflow of DL used to infer membranes of neurites and Purkinje cells.

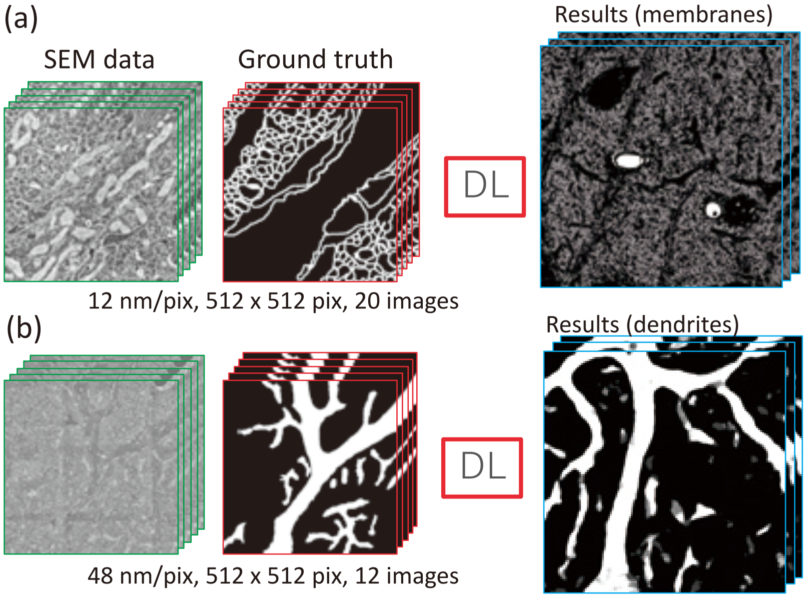

(a) SEM images of membranes of neurites, ground truth, and inferred results. (b) SEM images of Purkinje cells, ground truth, and inferred results.

Fig. 6 Example of tracing a neurite from high-resolution SEM images for serial sections. The green areas show the target neurites.

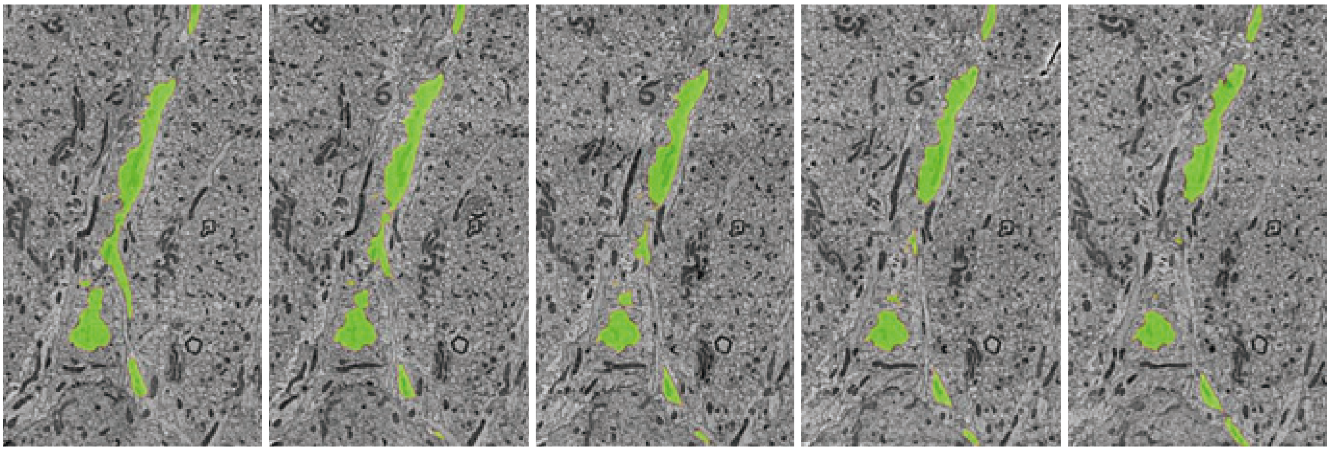

The same method was used to infer the dendrites of the Purkinje cells. The divided high-magnification images (6 nm/pix) with 8,000 × 8,000 were binned, and images with 48 nm/pix and 1,000 × 1,000 pixels were evaluated. From these images, areas of 512 × 512 pixels were cut out, and 12 were used for training data with the corresponding ground truths, which were manually prepared (Fig. 5 (b)). Using these SEM images and ground truth, the DL model was trained and applied to the binned images (48 nm/pix, 1,000 × 1,000 pixels) to infer the dendrites (Fig. 5 (b)). The results of inference were binarized using the Otsu method (Fiji).

Trace of CF using manual corrections

From the cell membranes inferred using DL, with manual corrections, the neurites were effectively traced [27]. In this way, the target CF was traced from the identified area (green area in Fig. 4 (f)).

An example of tracing the CF using high-magnification SEM images is shown in **Fig. 6**. Using high-magnification SEM images and cell membranes inferred using DL (not shown), the target neurite (green areas in Fig. 6) surrounded by cell membranes were traced. Thus, the target neurite, in this case CF, was effectively traced.

Fig. 7 Climbing fiber (CF).

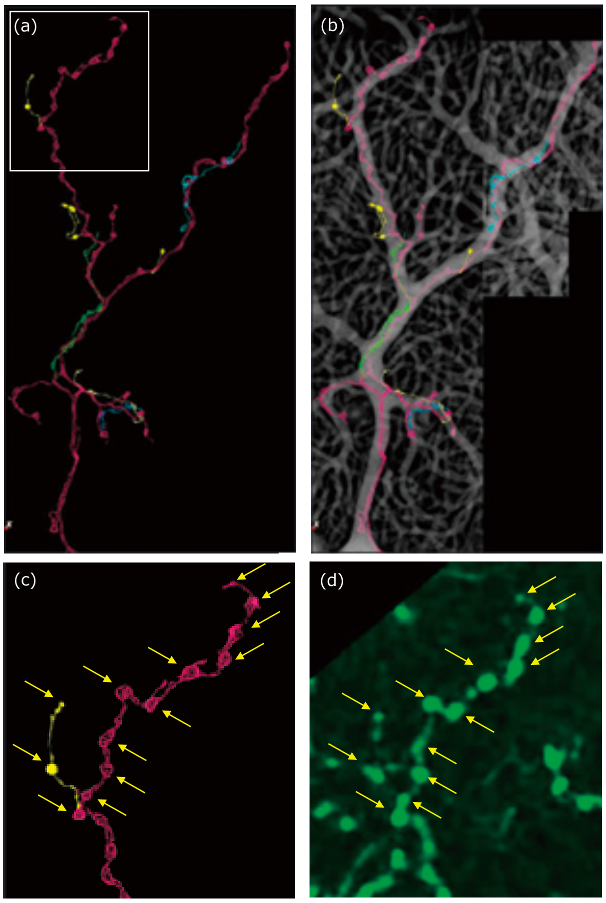

(a) CF traced from high-magnification SEM images with different colors showing different branches for clarity, (b) the same CF in (a) overlaid on the dendrites of the Purkinje cells inferred by DL, (c) enlarged image corresponding to rectangle in (a), and (d) fluorescent image of CF corresponding to (c). The traced CFs are around the Purkinje cell with complex branches ((a), (b)). The boutons in the traced CF (arrows in (c)) correspond well with those in the fluorescent image (arrows in (d)), indicating that the target CF found in the fluorescent images was unambiguously traced using CLEM.

3D reconstruction of CF

Traced CF and dendrites were already aligned in the z-direction, and 3D reconstruction was accomplished by simply stacking the high-magnification SEM images. Stacker (System in Frontier) was used for 3D reconstructions and Visualizer-evo (System in Frontier) was used for their visualization.

The traced CF is shown in **Fig. 7**. Fig. 7 (a) shows the CF traced from the high-magnification SEM images, with different colors corresponding to branches for clarity. Fig. 7 (b) shows the same CF as in (a), with the dendrites of the Purkinje cells inferred using DL. Fig. 7 (c) shows an enlarged image of the rectangle in (a), whereas (d) shows the fluorescent image corresponding to (c). The traced CF is around the Purkinje cell with several complex branches (Fig. 7 (a) and (b)). In addition, the boutons in the traced CF (arrows in Fig. 7 (c)) correspond well with those in the fluorescent image (arrows in Fig. 7 (d)), indicating that the target CF found in the fluorescent images was unambiguously traced using the CLEM.

Discussion

Initially, we attempted to trace some neurites running around the dendrites of the Purkinje cell as candidates for the CF. However, we were unable to identify the correct CF. As described in this study, we were able to successfully trace the correct CF by identifying the same area in both LM and SEM images, and by tracing the CF starting from this area (green areas in the insert of Figs. 4 (c) and Fig. 4 (f)).

In this study, we traced the CF using a structure like a gourd, identified in both LM and SEM images; however, there is a possibility that we will be unable to find such a special structure for different samples. Even in such a case, the same CF can be identified using the correspondences of the boutons, as shown in Figs. 7 (c) and 7 (d). In addition, a method to improve the accuracy of alignment between the LM and SEM images was reported using the correspondences of the boutons [13]. A method using both nuclei and blood vessels was also reported for a rough alignment of the LM and SEM images [13] whereas only the corresponding nuclei in the LM and SEM images were used in this study.

Historically, serial-section TEM has been frequently used to trace neurites [28, 29], which requires an extremely high skill level because serial sections should be placed on an extremely small grid with an inner diameter of less than 2 mm. In addition, these sections are placed on a very thin supporting film such as formvar on a hole grid, and the samples are occasionally broken owing to the breaking of the film. By contrast, it is relatively easy to place the serial sections on large substrates such as silicon using a manipulator [30]. Various methods for placing serial sections on a substrate have also been reported [16, 17, 31, 32]. In addition, because bulk substrates are robust, the possibility of breaking the sections is strongly reduced. Furthermore, the handling of samples was significantly improved by placing the silicon substrates on a single stainless board. These improvements, along with the use of automatic image-acquisition software and DL for neurite tracing, drastically improved the efficiency of this approach.

Owing to the significant improvement in the efficiency of such a method when compared with traditional serial-section TEM, variations in CF structures corresponding to a knock-out/knock-in, drug administration, and aging will be studied in the future. In addition, CLEM will be applied not only to the analysis of CF, but also for studying fine 3D structures of various organs.

Acknowledgments

We would like to thank Dr. Kenji Tanaka at Keio University for providing the mice expressing fluorescent proteins at the CFs. We would also like to thank Mr. Katsuyuki Suzuki and Mr. Motohiro Nakamura at JEOL Ltd., and Mr. Junichi Nakakobaru at System in Forntier, Inc., for collaboration of the array supporter development.

References

[1] Takizawa, T., Suzuki, K. & Robinson, J. M. Correlative microscopy using FluoroNanogold on ultrathin cryosections: proof of principle. *Journal of Histochemistry & Cytochemistry* **46**, 1097-1102 (1998).

[2] Gaietta, G. *et al*. Multicolor and electron microscopic imaging of connexin trafficking. *Science* **296**, 503-507 (2002).

[3] Sartori, A. *et al*. Correlative microscopy: bridging the gap between fluorescence light microscopy and cryo-electron tomography. *Journal of structural biology* **160**, 135-145 (2007).

[4] Nishiyama, H. *et al*. Atmospheric scanning electron microscope observes cells and tissues in open medium through silicon nitride film. *Journal of structural biology* **172**, 191-202 (2010).

[5] Shu, X. *et al*. A genetically encoded tag for correlated light and electron microscopy of intact cells, tissues, and organisms. *PLoS biology* **9**, e1001041 (2011).

[6] Lam, S. S. *et al*. Directed evolution of APEX2 for electron microscopy and proximity labeling. *Nature methods* **12**, 51 (2015).

[7] Miyazono, Y. *et al*. Uncoupled mitochondria quickly shorten along their long axis to form indented spheroids, instead of rings, in a fission-independent manner. *Scientific reports* **8**, 350 (2018).

[8] Kashiwagi, Y. *et al*. Computational geometry analysis of dendritic spines by structured illumination microscopy. *Nature communications* **10**, 1285 (2019).

[9] Denk, W. & Horstmann, H. Serial block-face scanning electron microscopy to reconstruct three-dimensional tissue nanostructure. *PLoS biology* **2**, e329 (2004).

[10] Knott, G., Marchman, H., Wall, D. & Lich, B. Serial section scanning electron microscopy of adult brain tissue using focused ion beam milling. *Journal of Neuroscience* **28**, 2959-2964 (2008).

[11] Micheva, K. D. & Smith, S. J. Array tomography: a new tool for imaging the molecular architecture and ultrastructure of neural circuits. *Neuron* **55**, 25-36 (2007).

[12] Burel, A. *et al*. A targeted 3D EM and correlative microscopy method using SEM array tomography. *Development* **145**, dev160879 (2018).

[13] Drawitsch, F., Karimi, A., Boergens, K. M. & Helmstaedter, M. FluoEM, virtual labeling of axons in three-dimensional electron microscopy data for long-range connectomics. *Elife* **7**, e38976 (2018).

[14] Fang, T. *et al*. Nanobody immunostaining for correlated light and electron microscopy with preservation of ultrastructure. *Nature methods* **15**, 1029 (2018).

[15] Wacker, I. & Schroeder, R. Array tomography. *Journal of microscopy* **252**, 93-99 (2013).

[16] Koga, D., Kusumi, S., Ushiki, T. & Watanabe, T. Integrative method for three-dimensional imaging of the entire Golgi apparatus by combining thiamine pyrophosphatase cytochemistry and array tomography using backscattered electron-mode scanning electron microscopy. *Biomedical Research* **38**, 285-296 (2017).

[17] Koike, T. *et al*. A device for ribbon collection for array tomography with scanning electron microscopy. *Acta Histochemica et Cytochemica* **50**, 135 (2017).

[18] Kubota, Y. *et al*. A carbon nanotube tape for serial-section electron microscopy of brain ultrastructure. *Nature communications* **9**, 437 (2018).

[19] Kasthuri, N. *et al*. Saturated reconstruction of a volume of neocortex. *Cell* **162**, 648-661 (2015).

[20] Wilson, A. M. *et al*. Developmental Rewiring between Cerebellar Climbing Fibers and Purkinje Cells Begins with Positive Feedback Synapse Addition. *Cell reports* **29**, 2849-2861. e2846 (2019).

[21] Hildebrand, D. G. C. *et al*. Whole-brain serial-section electron microscopy in larval zebrafish. *Nature* **545**, 345 (2017).

[22] Ito, M. Long-term depression. *Annual review of neuroscience* **12**, 85-102 (1989).

[23] Watanabe, M. & Kano, M. Climbing fiber synapse elimination in cerebellar Purkinje cells. *European Journal of Neuroscience* **34**, 1697-1710 (2011).

[24] Kakegawa, W. *et al*. Anterograde C1ql1 signaling is required in order to determine and maintain a single-winner climbing fiber in the mouse cerebellum. *Neuron* **85**, 316-329 (2015).

[25] Tanaka, K. F. *et al*. Expanding the repertoire of optogenetically targeted cells with an enhanced gene expression system. *Cell reports* **2**, 397-406 (2012).

[26] Kanemaru, K. *et al*. In vivo visualization of subtle, transient, and local activity of astrocytes using an ultrasensitive Ca2+ indicator. *Cell reports* **8**, 311-318 (2014).

[27] Konishi, K. *et al*. Practical method of cell segmentation in electron microscope image stack using deep convolutional neural network. *Microscopy* **68**, 338-341 (2019).

[28] White, J. G., Southgate, E., Thomson, J. N. & Brenner, S. The structure of the nervous system of the nematode Caenorhabditis elegans. *Philos Trans R Soc Lond B Biol Sci* **314**, 1-340 (1986).

[29] Ichikawa, R. *et al*. Distal extension of climbing fiber territory and multiple innervation caused by aberrant wiring to adjacent spiny branchlets in cerebellar Purkinje cells lacking glutamate receptor δ2. *Journal of Neuroscience* **22**, 8487-8503 (2002).

[30] Spomer, W. *et al*. Advanced substrate holder and multi-axis manipulation tool for ultramicrotomy. *Microscopy and Microanalysis* **21**, 1277-1278 (2015).

[31] Hayworth, K., Kasthuri, N., Schalek, R. & Lichtman, J. Automating the collection of ultrathin serial sections for large volume TEM reconstructions. *Microscopy and Microanalysis* **12**, 86-87 (2006).

[32] Schalek, R. *et al*. Development of high-throughput, high-resolution 3D reconstruction of large-volume biological tissue using automated tape collection ultramicrotomy and scanning electron microscopy. *Microscopy and Microanalysis* **17**, 966-967 (2011).

Development of JEM-ARM300F2: an Aberration Corrected 300 kV Microscope Capable of Both Ultrahigh Spatial Resolution Imaging and Highly Sensitive Analysis over a Wide Range of Acceleration Voltage

Yu Jimbo, Hiroki Hashiguchi and Ichiro Ohnishi
EM Business Unit, JEOL Ltd.

We have developed a new model of an aberration corrected 300 kV transmission electron microscope named JEM-ARM300F2 (GRAND ARM™2). A newly designed objective lens pole-piece, named FHP2, for this microscope can realize both ultrahigh spatial resolution imaging and highly sensitive X-ray analysis over a wide range of acceleration voltages. Enclosure cover and enhancement of resistance to various disturbances have more improved electrical and mechanical stability than the previous model. They can be independent of changes in external environments and provide high performance in various regions around the world. A variety of new and auto functions enable to conduct atomic resolution observation and analysis for a wide range of users from beginners to experts. It is expected that the new microscope gives us a chance to conduct observation and analysis of the specimens that were previously difficult.

Introduction

Recent progress of aberration correctors has significantly improved spatial resolution of Transmission Electron Microscopy (TEM) and Scanning TEM (STEM). Realization of angstrom to sub-angstrom resolution has become common with the correctors. Recently, in addition to the high resolution imaging, chemical analysis in atomic level with Energy Dispersive X-ray Spectroscopy (EDS) and/or Electron Energy Loss Spectroscopy (EELS) has been realized, owing to the correctors.

In 2014, we have developed an aberration corrected 300 kV microscope, named JEM-ARM300F (GRAND ARM™) [1]. This microscope has been developed based on various technologies, both the JST CREST R005 project and our first commercial aberration corrected 200 kV microscope, JEM-ARM200F. The development concept of GRAND ARM™ was ultimate atomic resolution microscope to realize ultrahigh spatial resolution imaging. As a result, in 2015, this microscope in the University of Tokyo, achieved a STEM image resolution of 45 pm in combination with a 3rd order spherical aberration corrector (Expanding Trajectory Aberration corrector: ETA corrector) [2]. In 2017, the microscope successfully upgraded the resolution to 40.5 pm in combination with a 5th order spherical aberration corrector (DELTA corrector) [3]. Both of those results set accomplished a best-in-class resolution at that time, and they were achievements not be ashamed of the name of ultimate atomic resolution microscope.

However, the market requests for aberration corrected microscopes have dramatically changed over the past few years. We need the aberration corrected microscope capable of highly sensitive analysis as well as high spatial resolution imaging over a wide range of acceleration voltages from low kV to high kV in order to study various specimens including not only hard materials such as semiconductor device, metal and ceramics but also soft materials such as carbon, polymer and organic materials. In addition, the next aberration corrected microscope needs high stability keeping the same high performance at any place and any environments because it becomes popular that in many countries other than Japan, Europe and USA have the opportunity for such microscopes to be installed there. Moreover, the next aberration corrected microscope needs high usability which enables us to operate easily and safety not only for experts but also for beginners because it becomes common and is used by many users worldwide.

In order to respond to these changes, in 2020, we have newly developed JEM-ARM300F2, called GRAND ARM™2 (**Fig. 1**).

〉〉 3-1-2 Musashino, Akishima, Tokyo 196-8558, JAPAN | E-mail: yjimbo@jeol.co.jp

The GRAND ARM$^{\mathrm{TM}}$2 is a new model of GRAND ARM$^{\mathrm{TM}}$ with addition of various new functions and improvement of performance. The development concept is GRAND ARM$^{\mathrm{TM}}$ beyond GRAND ARM$^{\mathrm{TM}}$. Major additions and improvements are the following three points; (1) newly designed objective lens pole-piece named FHP2, (2) enclosure cover and enhancement of resistance to various disturbances, and (3) new functions to improve usability. In this paper, we will explain the features of GRAND ARM$^{\mathrm{TM}}$2, mainly focusing on the above three points.

Features of GRAND ARM$^{\mathrm{TM}}$2

(1) Newly designed objective lens pole-piece FHP2

The previous model, GRAND ARM$^{\mathrm{TM}}$, can be equipped with one of two kinds of objective lens pole-piece; WGP (Wide Gap Pole-piece) and FHP (Full High resolution Pole-piece). WGP has a large gap between the upper and lower parts of the pole-piece and has a shape optimized to Silicon Drift Detector (SDD) with a large-sized sensor. It can make a shorter distance between the specimen and the SDD compared to other pole-piece configurations. Then, the microscope with WGP can provide ultra-high sensitivity X-ray analysis with two windowless SDDs (Dual SDDs) whose sensor sizes are selectable to be 100 or 158 mm^2 in area. The total X-ray collection angle of Dual SDDs reaches 1.6 sr with 100 mm^2-sized SDD [4] and 2.2 sr with 158 mm^2-sized SDD [5]. The GRAND ARM$^{\mathrm{TM}}$2 with WGP can also realize ultra-high sensitivity X-ray analysis. In addition, WGP enables various in-situ experiments in combination with thick special specimen holders for heating, cooling, liquid, gas and so on, because the WGP has a large space to insert them.

On the other hand, FHP is dedicated to ultra-high spatial resolution imaging because it has very small spherical and chromatic aberration coefficients. As mentioned above, the microscope with FHP can achieve resolution of 45 pm with the Expanding Trajectory Aberration (ETA) corrector [2] and 40.5 pm with DELTA corrector [3] in STEM. However, the highly sensitive EDS analysis has not been attained for the FHP configuration. The main reason is that the gap of the FHP is narrow and thick to avoid saturation of magnetic flux, and the distance between the specimen and the large-sized SDD is longer than that with use of an analytical pole-piece. The X-ray detection efficiency of the microscope with FHP is much lower than that with WGP, and its collection angle is only 0.7 sr even when using 100 mm^2-sized Dual SDDs.

In order to improve this situation, we have developed a new objective lens pole-piece named FHP2 for GRAND ARM$^{\mathrm{TM}}$2 to realize both ultra-high spatial resolution imaging and highly sensitive EDS analysis (**Fig. 2**). The FHP2 has the same gap width as FHP, but its shape changes to be optimized to the 158 mm^2-sized SDD. Then, it allows to attach 158 mm^2-sized Dual SDDs. Finally, the total X-ray collection angle reaches to be 1.4 sr (0.7 sr for each) with the 158 mm^2-sized Dual SDDs. The value is 2 times larger than that of FHP with 100 mm^2-sized Dual SDDs (0.7 sr) and approaches to that of WGP with 100 mm^2-sized Dual SDDs (1.6 sr). And the elevation angle of both detectors reaches to be 26 degrees. It can minimize the shadowing effects of the specimen holder to increase the effective X-ray intensity. **Figure 3** shows a comparison of X-ray intensities of Ni K line from a NiOx thin film obtained by using 3 kinds of pole-piece configurations under the same conditions. The X-ray intensity with FHP2 and the 158 mm^2-sized Dual SDDs reaches ~1.4 times higher than that with UHR and the 100 mm^2-sized Dual SDDs. In addition to high X-ray intensity, background noise and system peaks in EDS spectrum were

Fig. 1 Appearance of JEM-ARM300F2 (GRAND ARM$^{\mathrm{TM}}$2).

Fig. 2 Schematic illustration of a cross-sectional view for comparison between FHP and FHP2.

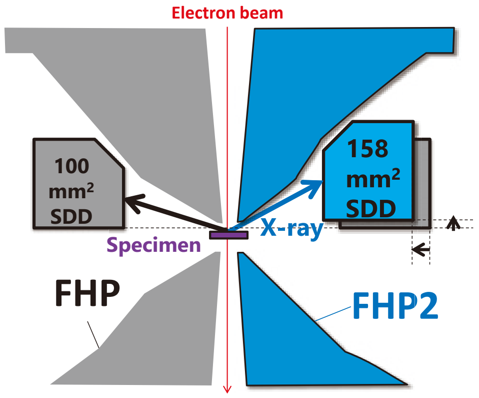

Fig. 3

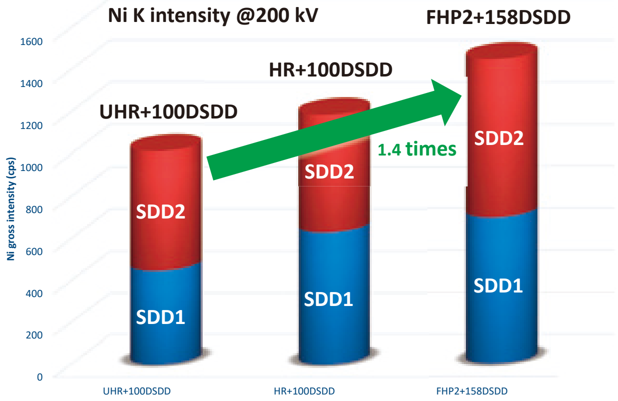

Comparison of X-ray intensity of Ni K line from NiOx thin film specimen taken by using three kinds of objective lens pole-piece configurations (UHR, HR, and FHP2).

improved with the FHP2 configuration because high elevation angle of the SDDs can reduce the effect of Bremsstrahlung X-ray. With NiOx thin films, we estimated the system peaks with accuracy of less than 0.5% and the Fiori P/B ratio of more than 4,000 using FHP2 and 158 mm^2-sized Dual SDDs.

The capability of EDS analysis was improved, while the FHP2 can keep the performance of ultra-high spatial resolution. **Figure 4** shows atomic resolution High Angle Annular Dark Field (HAADF) STEM images (one shot & raw image) for Si [110] and GaN [211] and their Fast Fourier Transform (FFT) patterns obtained by using the microscope with the FHP2 and the ETA corrector at 300 kV. In the HAADF image shown in Fig. 4c, the Ga-Ga dumbbell with a projected spacing of 63 pm is clearly resolved. In its FFT pattern shown in Fig. 4d, spots with spacing less than 50 pm are observed. **Figure 5** shows a HAADF STEM image (overlay of 20 images) and its FFT pattern for GaN [211] at 300 kV. In this case, even spots of 45 pm separation are observed in FFT pattern (Fig. 5b). These results suggest that the FHP2 has the same or higher performance in spatial resolution compared to FHP.

In addition, the FHP2 configuration enables us to take EDS maps at sub-angstrom levels, which was previously difficult. **Figure 6** shows a comparison of atomic resolution HAADF, Annular Bright Field (ABF) STEM images and EDS elemental map (Wiener filtered) for GaN [211] obtained by using the FHP2 configuration and 158 mm^2-sized Dual SDDs at 300 kV. In the HAADF image, only the Ga atomic column is visible. On the other hand, in both ABF image and EDS map, not only Ga but also N atomic column is clearly observed. In addition, even EDS map resolves the Ga-Ga dumbbell. The result suggests that the spatial resolution of the EDS map reaches better than 63 pm with the FHP2 configuration and 158 mm^2-sized Dual SDDs.

Even at low accelerating voltage, the FHP2 can keep the performance of ultra-high spatial resolution imaging because the pole-piece has a small chromatic aberration coefficient, similar to FHP. **Figure 7** shows HAADF, ABF STEM images and the FFT pattern of HAADF image for GaN [110], obtained by the microscope with FHP2 at 60 kV. The Ga atomic column is observed in HAADF image, while both the Ga and N atomic

Fig. 4

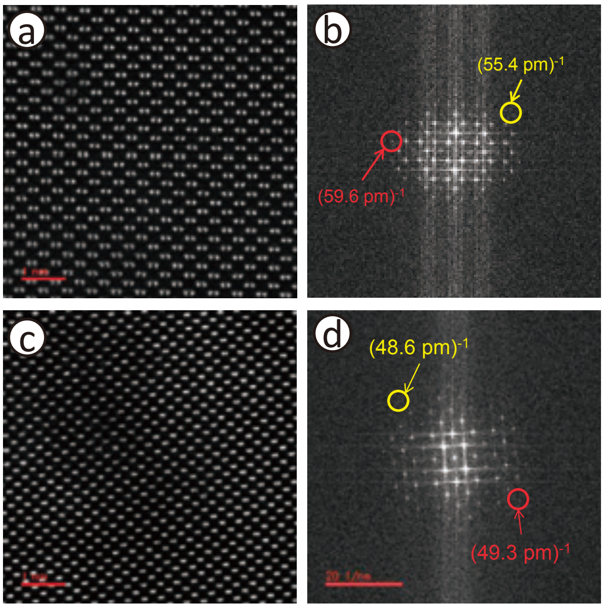

Atomic resolution HAADF STEM images (single shot & raw image) and their FFT patterns for Si [110] (a, b) and GaN [211] (c, d) taken by using GRAND ARM™2 (FHP2) with Expanding Trajectory Aberration (ETA) corrector at 300 kV.

Fig. 5

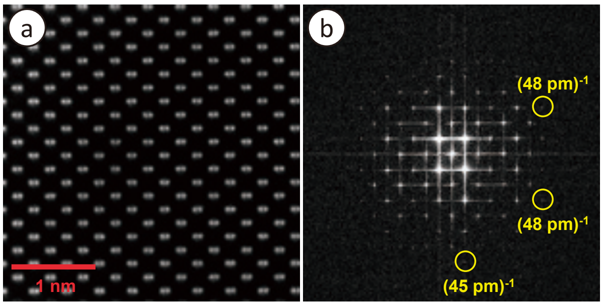

Atomic resolution HAADF STEM image (overlay of 20 images) (a) and its FFT pattern (b) for GaN[211] taken by using GRAND ARM™2 (FHP2) with ETA corrector at 300 kV.

Fig. 6

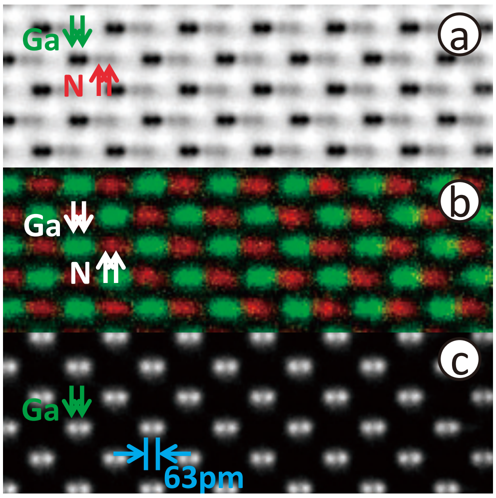

Comparison of atomic resolution ABF-STEM image, EDS elemental map (Wiener filtered) and atomic resolution HAADF-STEM image for GaN [211] (from top to bottom) obtained by using GRAND ARM™2 (FHP2) with 158 mm^2-sized Dual SDDs at 300 kV.

Fig. 7

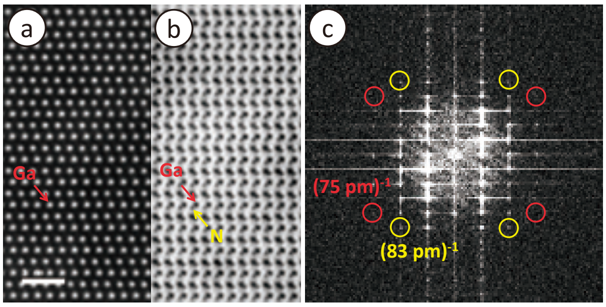

Atomic resolution HAADF and ABF STEM images (a, b) and FFT pattern (c) for GaN [110] taken by using GRAND ARM™2 (FHP2) with ETA corrector at 60 kV.

columns are clearly resolved in ABF image. In the FFT pattern of HAADF image, not only 83 pm but also 75 pm spots are recognized. These results suggest that the FHP2 configuration can take sub-angstrom level imaging even at 60 kV. **Figure 8** shows EDS maps for a monolayer WS_2 sheet obtained by the FHP2 configuration and 158 mm^2-sized Dual SDDs at 80 kV. Each atom of sulfur and tungsten can be clearly recognized. The FHP2 can take atomic resolution elemental maps from even such 2D monolayer materials, which was previously difficult to take.

As described above, the FHP2 is all-purpose type pole-piece capable of both ultra-high spatial resolution imaging and highly sensitive analysis over a wide range of acceleration voltage. The GRAND ARM^{TM}2 with FHP2 configuration has high versatility and is expected to enable observation and analysis for a wide variety of specimens, including not only hard materials but also soft materials.

Fig. 8

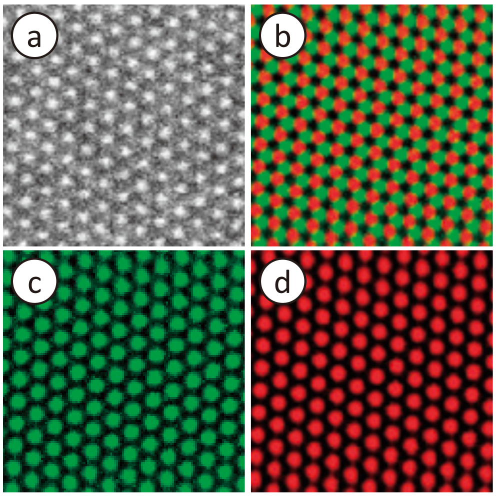

Atomic resolution HAADF image (a) and EDS elemental maps (Wiener filtered) (b-d) of a monolayer WS_2 sheet (b: overlay, c: S Kα, d: W Mα) taken by using GRAND ARM^{TM}2 (FHP2) with 158 mm^2-sized Dual SDDs at 80 kV.

(2) Enclosure and enhancement of resistance to various disturbances

The appearance of GRAND ARM^{TM}2 has been significantly re-designed from that of GRAND ARM^{TM}. The TEM column is covered by a box-type enclosure mainly composed of metallic frames and panels (Fig. 1). The enclosure reduces the effect of environmental changes such as temperature, air flow, acoustic noise and so on, and then it improves the stability of microscope. **Figure 9** shows the results of information limits of GRAND ARM^{TM} and GRAND ARM^{TM}2 estimated from TEM images when the artificial noises of 65 to 95 dB were applied to both instruments. A larger amount of information loss occurs in the FFT pattern of the TEM image due to higher vibration noise along with higher level of artificial noise. In GRAND ARM^{TM}, spots of better than 1 angstrom disappear at >75 dB, while in GRAND ARM^{TM}2, most of those spots continue to appear even at ~90 dB, suggesting that the loss rate of information to the noise in GRAND ARM^{TM}2 is less than that in GRAND ARM^{TM}. The comparison of results at 75 dB, which is noise level corresponding to the sound of TV and running cars, indicates that the information limit of GRAND ARM^{TM}2 (~60 pm) has 2 times as much information as that of GRAND ARM^{TM} (~118 pm). These results suggest that GRAND ARM^{TM}2 has 2 times higher resistance to external noise compared to GRAND ARM^{TM}. Meanwhile, the enclosure contains a crane as standard equipment. By using the crane, we can swap the electron gun, lens etc., so we do not need an additional crane in the microscope room. The crane inside the enclosure improves work efficiency of maintenance for microscope.

In addition to the enclosure, many modifications to the microscope itself were applied, which improve the stability and resistance to various disturbances for GRAND ARM^{TM}2. The first modification is about Sputter Ion Pump (SIP) in a Cold Field emission Electron Gun (CFEG). We newly adopted

Fig. 9 Summary of the TEM information limits when the artificial noise from 65 to 95 dB was applied to GRAND ARM^{TM} and GRAND ARM^{TM}2.

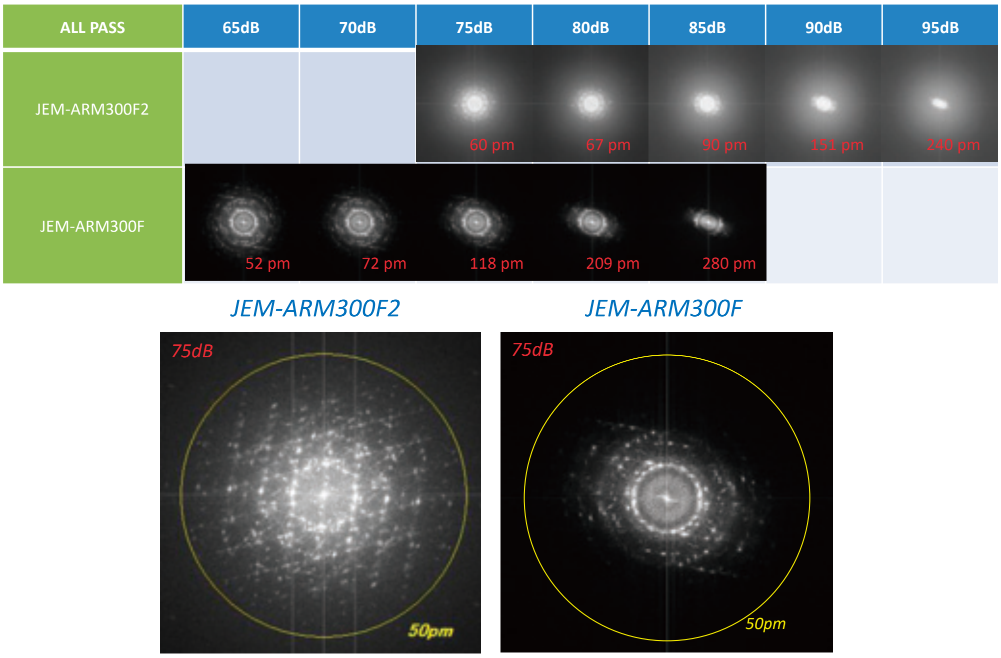

a smaller SIP with a larger evacuation volume than before for CFEG in GRAND ARM$^{\text{TM}}$2. Enhancement of evacuation volume of SIP improves the degree of vacuum near the emitter inside CFEG, and also improves the stability of emission and probe currents (**Fig. 10**). The miniaturization of SIP can reduce the total mass of CFEG by ~100 kg. The weight saving of CFEG improves resistance to vibration for the microscope. The second modification is in the design of the ETA corrector. The Bore diameter of the corrector was optimized and cooling efficiency of the corrector was improved. They reduce electrical noise inside the corrector and improve its stability. The third modification concerns the electronics of lens and vacuum pump. Enhancement of electrical stability of the illumination lens and optimization of the electrical ground of vacuum pump reduce the electrical noise for the microscope. Moreover, modification of the hoses for cooling lens and optimization of fixing method to the illumination lens, objective lens pole-piece and cryo fin reduce vibration noise of the microscope.

As a result, the adoption of enclosure and many modifications of microscope itself enhance electrical and mechanical stability of GRAND ARM$^{\text{TM}}$2 and then they significantly improve image quality and spatial resolution of, in particular, STEM (**Fig. 11** and **Table 1**), compared to GRAND ARM$^{\text{TM}}$. Figure 11 shows HAADF STEM images and FFT patterns for Si [110] and GaN [211] obtained by using GRAND ARM$^{\text{TM}}$2 with WGP and ETA corrector. In FFT patterns, spots close to 50 pm are clearly observed even with WGP configuration, indicating that the spatial resolution of GRAND ARM$^{\text{TM}}$2 has been significantly improved than that of GRAND ARM$^{\text{TM}}$ (Table 1).

Moreover, the stability of high resolution observation by using heating or 3rd vendor special specimen holders was also improved for GRAND ARM$^{\text{TM}}$2. In the previous model, the gonio cover

Fig. 10 Comparison of probe current stability between old and new CFEG.

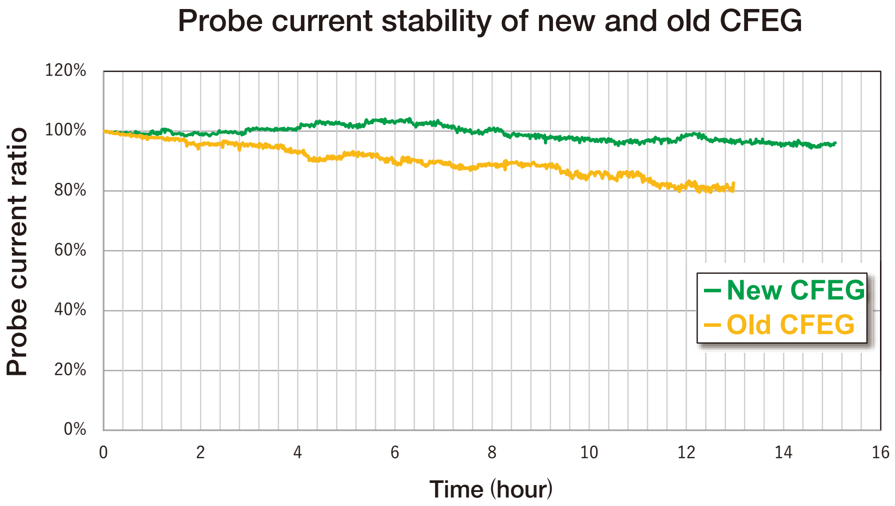

Fig. 11

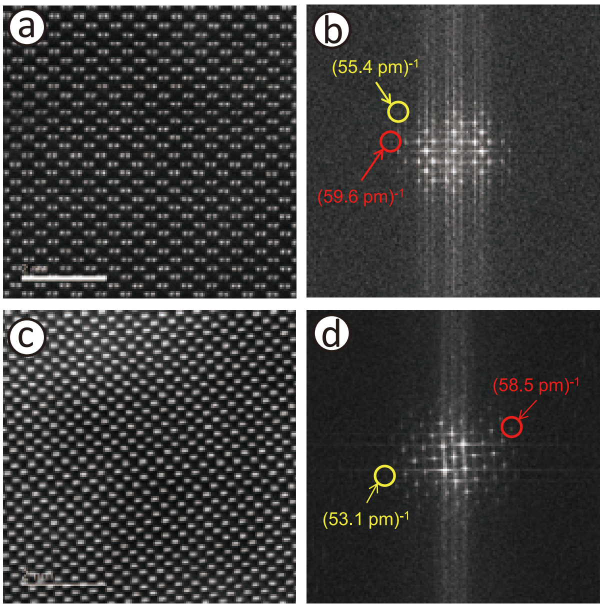

Atomic resolution HAADF STEM images (single shot & raw image) and their FFT patterns for Si [110] (a, b) and GaN [211] (c, d) taken by using GRAND ARM$^{\text{TM}}$2 (WGP) with ETA corrector at 300 kV.

Table 1

Acceleration voltage	GRAND ARM™ (FHP)	GRAND ARM™2 (FHP2)
300 kV	63 pm	53 pm
200 kV	78 pm	63 pm
80 kV	136 pm	96 pm
60 kV	136 pm	96 pm
40 kV	192 pm	136 pm

Acceleration voltage	GRAND ARM™ (WGP)	GRAND ARM™2 (WGP)
300 kV	82 pm	59 pm
200 kV	105 pm	82 pm
80 kV	136 pm	111 pm
60 kV	192 pm	136 pm
40 kV	313 pm	192 pm

Guaranteed STEM image resolution with STEM ETA corrector for GRAND ARM$^{\text{TM}}$ and GRAND ARM$^{\text{TM}}$2.

must be opened to use such a special specimen holder because the holder needs to be connected to a control/monitor unit with a cable. Then it generates noise in the image and reduces the spatial resolution due to external disturbances. On the other hand, GRAND ARM™2 has a new connector for a cable of special specimen holder inside the gonio cover. This allows us to close gonio cover when we use such a special specimen holder. The connector inside the gonio cover is connected to an external connector on the side of the enclosure, and the holder control/monitor unit can be used outside the enclosure by using the external connector. Since the special specimen holder can be used with the gonio cover closed, it is more resistant to disturbances, and can be expected to improve the stability and spatial resolution for heating or other environment experiments.

As described above, GRAND ARM™2 has higher resistance to external disturbances due to adoption of enclosure cover and enhancement of electrical and mechanical stability compared to the previous model. Then it is expected that the microscope can respond to various environments and installation conditions and can always provide high performance and high stable operation in various countries and regions other than Japan, Europe and USA.

(3) New and auto functions to improve usability:

For GRAND ARM™2, a digital camera is provided as a standard equipment inside the viewing chamber of the TEM column. Images taken with the camera can be observed by operating the microscope using the camera software “Sight-X”. There are two types of camera in the viewing chamber. One is a CCD camera for observing a large fluorescent screen, while the other is a CMOS camera for observing a small fluorescent screen. You can easily switch between each camera with just one button on the control panel. “TEM Center” software for controlling the TEM main unit, the “JEOL COSMO™” software for aberration corrector, and Sight-X are integrated into a single PC and a single large-sized monitor of 43 inches as standard. Since all the software can be simultaneously displayed on one monitor, the usability has been significantly improved. Remote operation with a maximum distance of 15 m from the microscope can be performed by using an USB extinction cable to connect with control panels. In addition, remote operation of the microscope from location over 15 m using a network is optionally available.

Various auto functions were added or enhanced in TEM Center and JEOL COSMO™. For instance, in the previous model, we need complicated operations for switching the acceleration voltage, while, in GRAND ARM™2, we just need to set the target acceleration voltage and press the start button, and then the target voltage is automatically loaded. We do not need other operation. The alignment data of the microscope itself and the aberration corrector for target voltage were automatically restored. In addition, short circuit mechanism at low acceleration voltage is also automatically worked. Any user can switch the acceleration voltage arbitrarily without complicated operations. In addition, auto loading of the acceleration voltage after conditioning, which is conducted after baking, can be performed by simply setting the target acceleration voltage and pressing the start button before conditioning. It improves work efficiency of maintenance for the microscope. Moreover, an auto function of beam shower, which is one of the methods to suppress a specimen contamination, is newly available for GRAND ARM™2. The user simply presses the start button, and then the beam shower is automatically performed at the preset conditions of electron beam intensity and defocus value. After the set time has elapsed, the electron beam is automatically restored to its original state before starting the shower. It can provide easy operation for conducting beam shower under constant conditions. Aberration correction using JEOL COSMO™, which was well-established in GRAND ARM™, has also been enhanced by optimizing parameters for auto cyclic script program of aberration correction. It enables semi-automatic correction and makes it easy even for beginners to adjust aberrations.

In addition to various auto functions, a variety of new functions improving usability are also added to GRAND ARM™2. In the previous model, unfortunately, there was a discrepancy between the operation direction on the operation panel/GUI and the direction of movement of the aperture. But this was overcome by renewal of the optical system and performing rotation correction for GRAND ARM™2. The aperture moves upward in the TEM image, if commanded to move it up in the operation panel/GUI. It moves right side in the TEM image, if commanded to move to the right on the operation panel/GUI. Similarly, the direction of movement of the stage and the direction of movement of the TEM and STEM images were matched by performing rotation correction. In particular, in the case of STEM images, the angle of the scanning image changes by the scan ratio in some cases. But even if so, the direction of movement of the scanning image on the PC monitor does not change. Then, the scanning image moves upward on monitor, if commanded to move it up on the trackball/GUI. It moves right side on the monitor, if commanded to move right on the trackball/GUI. With the addition of functions that were often overlooked in the previous model for performance emphasis, the operability and throughput have been significantly improved in GRAND ARM™2 and they allow us to use the aberration corrected microscope safely for a wide range of users from experts to beginners.

Summary

We have upgraded the model of the aberration-corrected 300kV microscope (GRAND ARM™) to the newly developed GRAND ARM™2. For the GRAND ARM™2, a newly designed objective lens pole-piece named FHP2 can be equipped, and the electrical and mechanical stability of the microscope were enhanced by adopting enclosure cover and so on, and new various functions were added to improve the usability of the previous model. The GRAND ARM™2 with these new technologies and new functions can provide both ultra-high spatial resolution imaging and highly sensitive X-ray analysis of any specimen by any user in any environment. Our new microscope is expected to be useful for studying the latest novel nanomaterials now and in the future.

Acknowledgments

We thanks Tomohisa Fukuda, Kimitaka Hiyama, Naoki Fujimoto, Syunsaku Waki, Yuji Yamazaki, Kyohei Terasaki, Arimasa Hanawa, Hiroyuki Tanaka, Katsuhiro Toyama, Sinichi Tanba, Takahiro Sasase, Takeshi Iwama, Takahiro Simazaki, Fumihiro Koba, Naoki Shimura, Junichi Morimoto, Yorinobu Iwasawa, Kouji Miyatake, Yusuke Toriumi, Shigeyuki Morishita, Norikazu Arima, Yoshifumi Hamada, Akihiro Ikeda, Yuta Sano, Yuji Kawano, Masaki Mukai, Hidetaka Sawada, and other project members for many corporations and helps for development of GRAND ARM™2.

References

[1] H. Sawada *et al*., JEOL News **49**. (2014) p.51-58.
[2] H. Sawada *et al*., Microscopy **64** (2015) p.213-217.
[3] S. Morishita *et al*., Microscopy **67**. (2017) p.46-50.
[4] E. Okunishi *et al*., JEOL News **50**. (2015) p.58-63.
[5] I. Ohnishi *et al*., e-J. Surf. Sci. Nanotech. **16** (2018), 286-288.

Various Analyses of Fine Structures using Multipurpose High Throughput Analytical FE-SEM: JSM-IT800

Osamu Suzuki, Noriyuki Inoue, Yuuki Yamaguchi
EP Business Unit, JEOL Ltd.

Scanning electron microscope (SEM) is widely utilized because its electron beam irradiation to a specimen enables us to know fine structure, composition, elemental distribution, chemical state, and crystal orientation information of the specimen, by detecting signal electrons, X-rays and cathodoluminescence from the specimen. JEOL's SEM with inlens-Schottky electron gun introduced in 1999, has earned a lot of achievements in the fields of R&D and quality assurance etc., that require a highly stable and a large probe current electron beam for various analysis techniques. In this paper, we present some examples of high throughput and various analyses of specimens using the latest field emission (FE) SEM JSM-IT800.

Introduction

A SEM irradiates a specimen with an accelerated electron beam by an electrical field, and detects secondary electrons emitted from the vicinity of the surface, or backscattered electrons in the vicinity of the surface. Electromagnetic waves such as X-rays and cathodoluminescence are also emitted from the specimen by the irradiating electron beam. By measuring them, we obtain surface morphology, composition information, crystal information, and element information.

JSM-IT800 is provided with a variety of detectors enabling to sort electrons by emitted angle and energy. And various analyzers are available, an energy dispersive X-ray spectrometer (EDS), a wavelength dispersive X-ray spectrometer (WDS), a soft X-ray emission spectrometer (SXES), a cathodoluminescence detector (CL) and a crystal orientation analyzer (Electron Backscattered Diffraction: EBSD). Especially, the EDS system is fully integrated with the SEM control system, and is an unparalleled feature of JSM-IT800. In recent years, there has been a strong demand for easy-to-operation and high-throughput analysis. JSM-IT800 can answer these user's demands.

1. JSM-IT800 Features

JSM-IT800 provides high-throughput analysis by using a field emission type electron gun that JEOL has established and operated for many years. The SEM also has various electron detection systems, a newly developed EDS integration system and an integrated data management system. Here, we present the features of both the hardware and the software of JSM-IT800.

1.1 FE electron gun

JSM-IT800 has inlens-Schottky Plus electron gun with an improved thermal field emitter (TFE). This gun provides a large probe current of 300 nA or more [1]. In addition, we have optimized the design for the large probe current and low incident energy for the SXES analysis. The condition is, for example, the probe current of 100 nA or more and the acceleration voltage of 5 kV.

1.2 Electrostatic/magnetic field superimposed lens

JSM-IT800 uses a hybrid lens (HL) which has a superimposed electrostatic and magnetic field. Its leakage magnetic field reaching the specimen surface is made to be nearly zero, and its electrostatic field accelerates a primary electron beam at the top of the lens, and rapidly decelerates near the exit of the lens. A schematic diagram of the hybrid lens is shown in **Fig. 1**.

HL reduces chromatic aberration compared to conventional objective lenses and provides high spatial resolution observation. In addition, it does not generate a magnetic field of the objective lens near the specimen, and the trajectories of backscattered electrons are not affected by the objective lens. Therefore, it enables crystal orientation analysis by the EBSD.

1.3 Detectors

JSM-IT800 is equipped with a variety of detectors as shown in Fig. 1. Secondary electron detector (SED) which is most common in the FE-SEM, backscattered electron detector (BED), upper electron detector (UED) and upper secondary electron detector (USD) can be equipped in JSM-IT800. By using these detectors, emitted electrons are sorted by emission angle and energy [1].

〉〉 3-1-2 Musashino, Akishima, Tokyo, 196-8558, Japan | E-mail: osuzuki@jeol.co.jp

1.4 Optimization of probe diameter by aperture angle control lens (ACL)

In JSM-IT800, the convergence angle control lens is introduced to achieve both high-throughput analysis and high spatial resolution. The convergence angle α of the electron beam contributes to the probe diameter of the electron beam in the form shown in **Fig. 2**. In JSM-IT800, NeoEngine, which is installed in the control system, constantly calculates the optimum convergence angle [1], and provides high spatial resolution and high-throughput analysis.

1.5 Zeromag

In the SEM observation, the process of locating ROI (region of interest) occupies a large proportion of the time. Previously, the users must use a manual step such as recording the shape of the specimen and the points to be observed in a note or marking the specimen before introducing the specimen into the SEM, and then moving the specimen stage while observing the SEM images to search for the ROI. These operations are inefficient, especially when the specimen size is large.

In order to improve the throughput of the locating ROI process, we incorporated Zeromag function into JSM-IT800. Zeromag superimposes the optical camera image photographed beforehand and the SEM image of the specimen on the same screen. The SEM image is displayed at a high magnification observation, and in other places, the optical image is displayed at a low magnification. They are seamlessly switched each other. An example of Zeromag function is shown in **Fig. 3**. The users can complete locating ROI in the shortest time using intuitive operation only by clicking the point to be observed with the mouse and setting to the proper magnification, without thinking that it is the optical image or the SEM image.

1.6 EDS integration system

We have developed "EDS Integration System" which integrates the EDS system into the SEM system to improve the throughput of analytical work in the SEM. In a conventional EDS system, an EDS is generally operated on a different PC than the SEM PC. In such a system, users have to operate two PCs.

In the EDS integration system, the SEM system takes in the

Fig. 1 Lenses configuration of JSM-IT800.

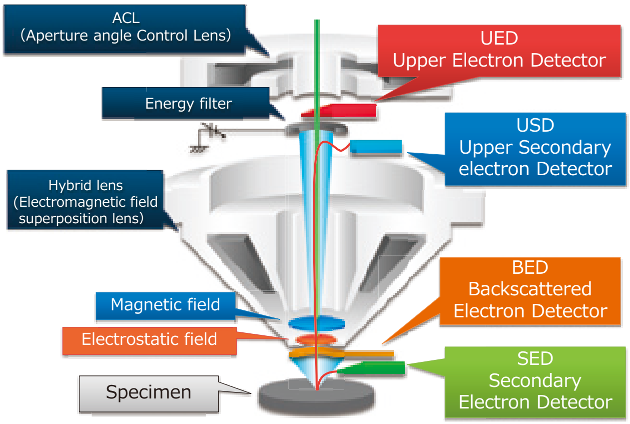

Fig. 2 Probe diameter as a function of convergence angle.

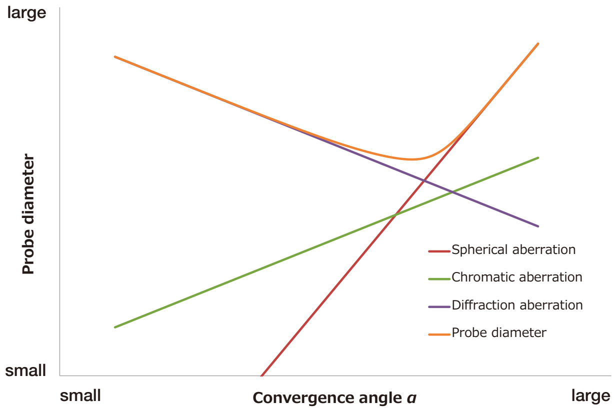

There exists an optimum convergence angle which minimizes the probe diameter under conditions of various electron optical aberrations.

Fig. 3 An example of Zeromag function.

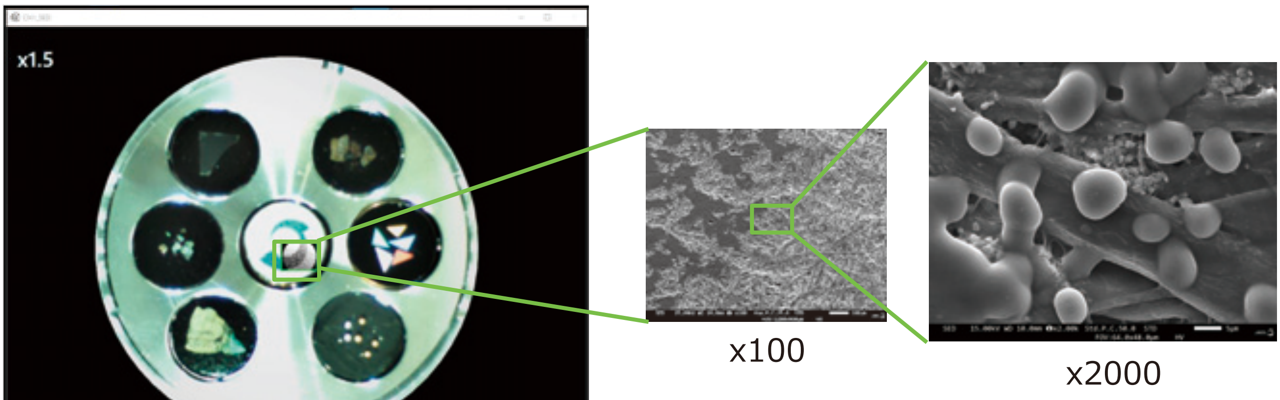

Specimen: Printed Paper
The inside of the frame of the central portion displays the SEM image, and the surrounding area displays the optical camera image acquired in advance. Seamlessly shift to the high magnification observation of the SEM can be done only by the magnification change.

EDS control system which is subdivided into functions such as spectral function and map function. As shown in **Fig. 4**, a group of buttons for the EDS operation are arranged in the immediate vicinity of the SEM operation screen so that the EDS analysis can be performed immediately after the SEM observation. In addition, the EDS integration system realizes the function which simultaneously carries out SEM observation and EDS mapping and spectrum acquisition. This function is called "live analysis", and it is useful as a tool to drastically improve the locating ROI process with Zeromag, because users can instantaneously know the elemental information which exists in the field of view of the SEM in real time.

1.7 Integrated Data Management System SMILE VIEW™ Lab

In considering the throughput of the entire SEM/EDS operation, the time required for the analysis and output of the data should also be considered. JSM-IT800 has adopted the integrated data management software called SMILE VIEW™ Lab, which reduces the time from data analysis to report preparation.

In conventional SEM/EDS system, each control system is independent as described in the previous section, and the data-management systems are also independent. Users have been forced to use two individual data systems when handling the SEM data and the EDS data.

In the data management system of SMILE VIEW™ Lab adopted in JSM-IT800, the SEM data and the EDS data are linked to the stage coordinate where the data was acquired. In other words, when the SEM image acquisition and the EDS analysis are performed at a certain position of the specimen, each data is stored in the same data folder on SMILE VIEW™ Lab. In addition, the stage coordinate of acquisition position is represented on Zeromag image and stored in the same folder. Users can manage stage coordinate data linked with Zeromag, the SEM data, and the EDS data on a single PC.

One-click report is also a unique feature of SMILE VIEW™ Lab. As shown in **Fig. 5**, we can create a report that summarizes the analysis data and information by simply selecting the desired data and pressing the report creation button.

2. Analysis of steel materials by using JSM-IT800

As has been described so far, JSM-IT800 is able to perform elemental analysis seamlessly by the EDS integration system not only observation of secondary electron images (SEI) and backscattered electron images (BEI). Furthermore, JSM-IT800 has the performance of various analytical methods such as high-speed particle analysis with high spatial resolution, elemental analysis and chemical state analysis by SXES and crystal orientation analysis by EBSD because the diameter of a primary

Fig. 4 An example of GUI when using EDS integration.

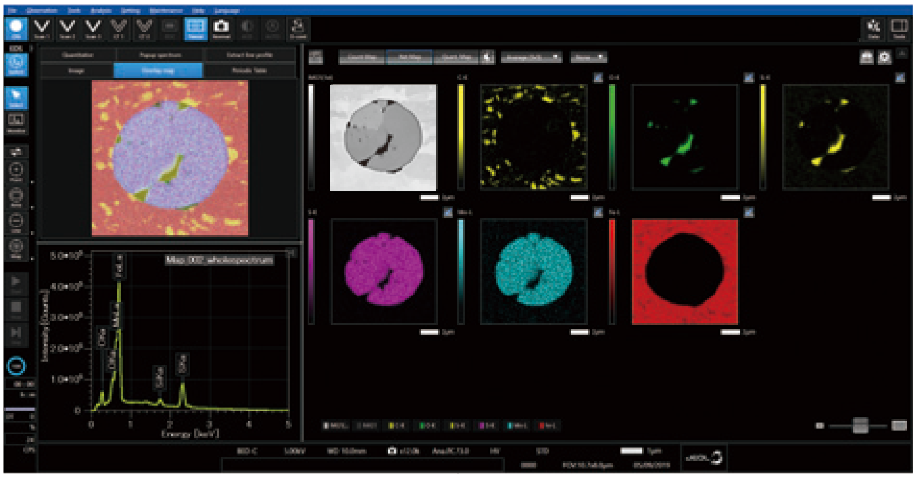

Specimen: Cross section of cast iron
Buttons arranged at the left side of the screen are tools for the EDS analysis, and the SEM operation and the EDS analysis operation can be completed in one screen.

Fig. 5 An example of one-click report.

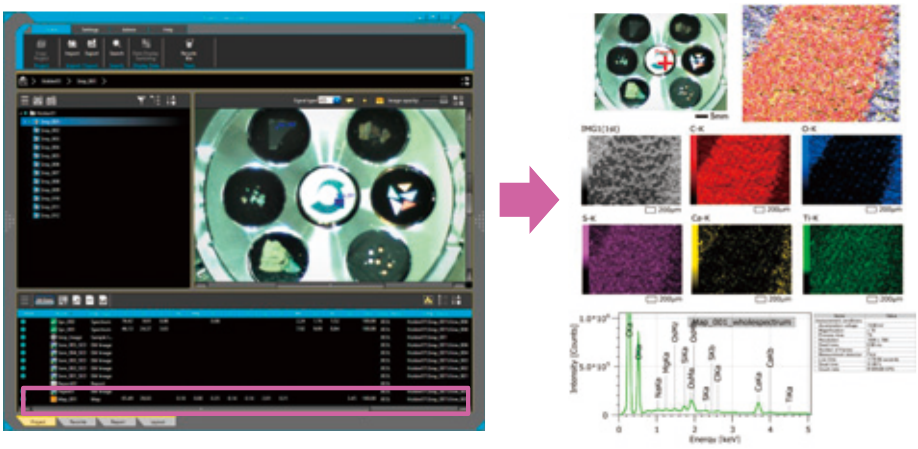

Specimen: Printed Paper
In SMILE VIEW™ Lab, the acquired data are managed together with the stage position and other information in a single data folder. A report with the acquired SEM and EDS data and other information is summarized by a simple operation of selecting arbitrary data and simply pressing the report preparation button.

electron beam is kept small even at a large probe current. In this chapter, we introduce applications of the analysis for quality control of steel materials by using these various methods.

Steel materials are used such as automobile frames and engines, parts of home electric appliances and materials of buildings. Therefore, steel materials are indispensable for our life. The characteristics of steel materials can be changed by manufacturing process, so various kinds of steel materials are produced. The steel-making process first involves the chemical reaction of iron ore and coke as raw materials under high temperatures to produce pig iron. Pig iron contains a lot of carbon so that it is not viscous and is brittle. Furthermore, impurities such as phosphorus (P), sulfur (S) and silicon (Si) also cause brittleness. Therefore, steel materials can be made by reducing the carbon content and removing the impurities from pig iron with the converter process. After that, various kind of steel materials are produced by using processes such as rolling and plating. It is possible to obtain a variety of properties by precisely controlling the size and content of inclusions such as oxides and sulfides and the crystal grain size of the iron in this steel-making process. Therefore, quality control is very important, and structural evaluation at micro and nano size which governs the characteristics becomes important.

There are various characterization methods of steel materials such as X-ray diffraction for understanding macroscopic crystal orientation, atomic-level structure analysis by transmission electron microscope (TEM) and crystal orientation analysis and elemental analysis in micro and nano size by SEM. Especially, SEM is a powerful technique for quality control in steel manufacturing because specimen preparation is relatively easy, topographic information is able to be obtained as seen with eyes and elemental analysis for fine structures is able to be carried out. JSM-IT800 is suitable for analysis of steel materials in the following reasons. 1st : EDS integration system enables seamless observation and elemental analysis of inclusions. 2nd : the leakage magnetic field of hybrid lens equipped in JSM-IT800 is nearly zero at the observation position. Thus, magnetic materials such as steels have almost no effect during observation and analysis. 3rd : hybrid lens does not generate a magnetic field that interferes with backscattered electrons from highly crystalline specimens, and therefore, crystal orientation analysis is possible with angular resolution of around 0.1 degrees by EBSD. Finally, a large probe current (more than 300 nA) is able to be obtained by inlens-Schottky Plus electron gun. It is possible to maximize the performance of analyzers such as SXES and EBSD.

SEM observation and various analysis of EDS for both elemental mapping and particle analysis, SXES and EBSD were carried out for mechanical polished cross sections of casted iron steel.

2.1 Observation of inclusions

First, SEI by SED and BEI by BED of one inclusion in the steel were obtained. The inclusion was observed at an incident voltage of 2 kV in order to obtain SEI and BEI of the specimen surface (**Fig. 6** (a)(b)). Both SEI and BEI show tiny black spots around the inclusions (arrows in Fig. 6 (a)(b)). Therefore, these black spots are regarded as holes which have topographic contrast, not compositional contrast. Thus, it is possible to reveal topographic contrast or compositional contrast by comparison of SEI and BEI in the same field of view. On the other hand, UED which is able to detect electrons with low energy enables us to obtain charging contrast in an insulator. This inclusion can be presumed an insulator because contrast due to charging was observed in UED. Next, the inclusion was observed at an incident voltage of 15 kV in order to obtain information for the depth of the specimen (Fig. 6 (c)(d)). Then, it was possible to obtain the compositional contrast of the deep part of the specimen, which was not visible in the specimen surface. This is the difference in penetration depth of the incident electron beam into the specimen. For example, the penetration depth of the incident electron beam in a bulk specimen of silicon oxide (SiO_2) was simulated to be around 90 nm at an incident voltage of 2 kV and around 2.8 µm at 15 kV by Electron Flight Simulator (Small World LLC Co.) (**Fig. 7**). Thus, changing the incident voltage enables us to reveal whether the information is of surface or depth.

Fig. 6 Observation images of steel inclusion.

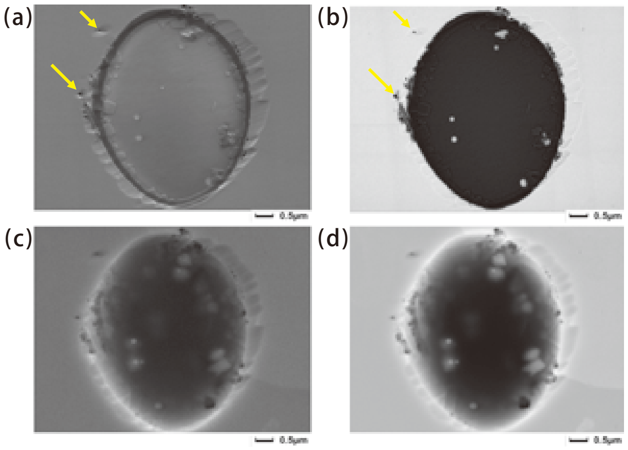

(a) Secondary electron image and (b) backscattered electron image at an incident voltage of 2 kV. (c) Secondary electron image and (d) backscattered electron image at an incident voltage of 15 kV.

Fig. 7

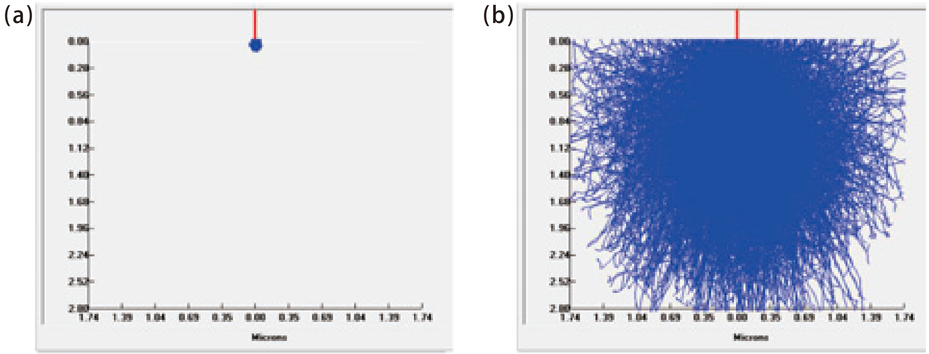

Simulations of penetration depth of an incident electron beam in a bulk specimens of silicon oxide (SiO_2) acquired at calculated at an incident energies of (a) 2.0 kV and (b) 15 kV.

2.2 EDS elemental mapping of inclusions

Elemental mapping was performed using EDS in order to clarify the relationship between the composition contrast in BEI and constituent elements. The JSM-IT800 enables us to obtain elemental mapping with easy operations after observation because EDS systems are integrated into SEM systems as described in chapter 1.6. EDS elemental mapping was acquired at an incident voltage of 15 kV, a probe current of 0.8 nA, a magnification of ×17,000 and acquisition time of around 8 minutes. An EDS spectrum and elemental maps are shown in **Fig. 8**. In the inclusions, since magnesium (Mg), aluminum (Al), silicon (Si), calcium (Ca) and manganese (Mn) are detected at the same areas of oxygen (O), it can be estimated that they are oxides of each element. Furthermore, since manganese (Mn) is also segregated in the segregation of sulfur (S), this segregation can be estimated that to be the manganese sulfide (MnS). In addition, segregation of titanium (Ti) and nitrogen (N) also exists. This segregation may be titanium nitride (TiN). However, it is difficult to separate the peaks of N-Kα and Ti-Ll because the energies of the N-Kα (0.392 eV) and the Ti-Ll (0.395 eV) are very close. In order to prove that, the segregation of titanium and nitrogen was analyzed by SXES.

2.3 SXES analyses

Recently, SXES has been developed that can be incorporated into FE-SEM. It is possible to analyze characteristic X-rays in soft X-ray region (low-energy region below 1 keV) by SXES [2]. SXES has diffraction gratings with unequally spaced grooves. Thus, characteristic X-rays can be simultaneously analyzed in a wide range of energies, despite being a wavelength dispersive detector. In addition, the energy resolution is higher compared to EDS and WDS, achieving 0.3 eV at the Fermi edge in the Al-L line of metallic Al. Therefore, even closely spaced peaks that must be spectrum-deconvoluted by EDS are able to be directly analyzed by SXES [3].

SXES measurement was performed with the nitrogen-titanium segregation shown in chapter 2.2 at an incident voltage of 2 kV, a probe current of 35 nA and an acquisition time of 30 minutes. As a result, a peak of the N-Kα secondary order was obtained around 196 eV and a peak of the titanium Ti-Ll secondary order was obtained around 198 eV (**Fig. 9**). It was revealed that this segregation was TiN because this spectrum is similar to the standard spectrum of TiN.

Fig. 8 EDS elemental maps of steel inclusions.

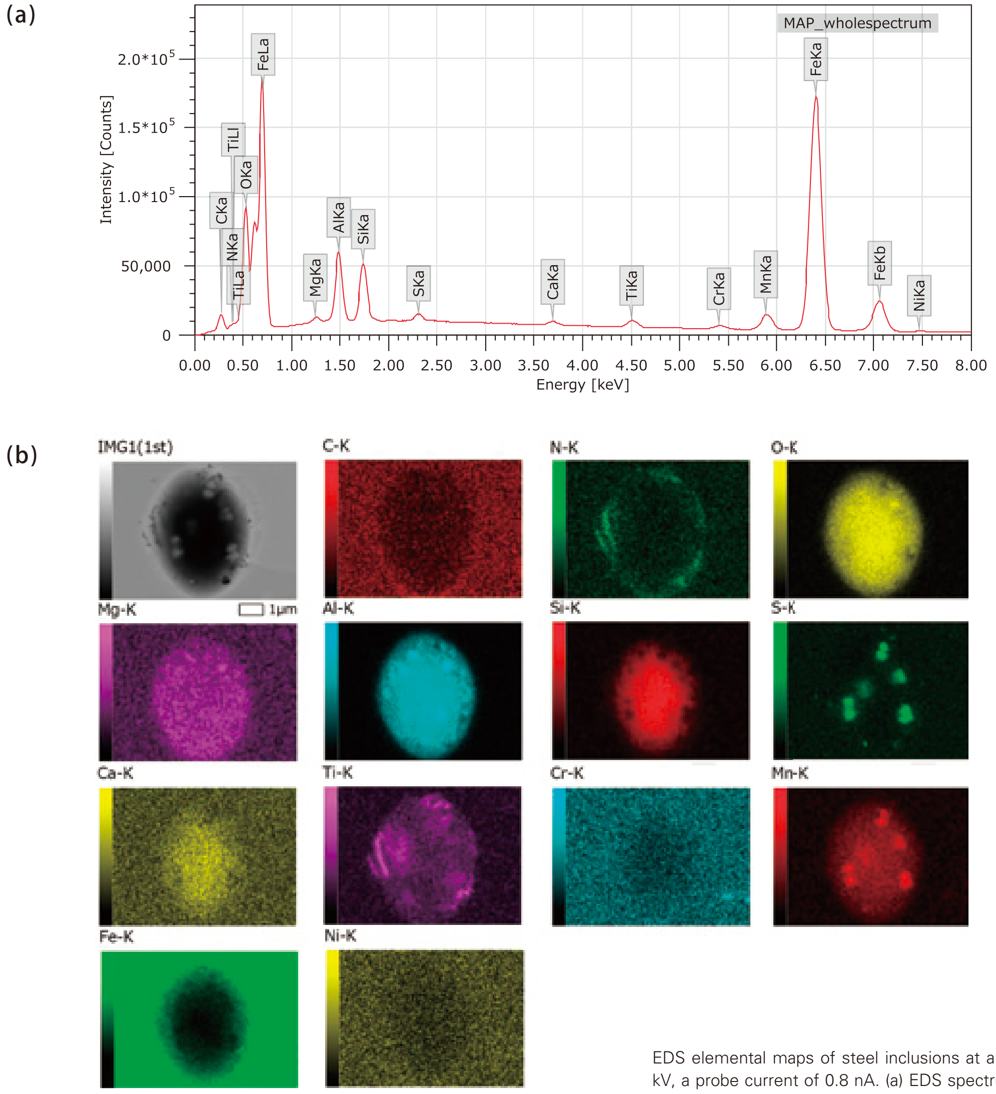

EDS elemental maps of steel inclusions at an incident voltage of 15 kV, a probe current of 0.8 nA. (a) EDS spectrum of the entire field of view. (b) Elemental maps.

2.4 Particle analysis

Particle analysis is a method that automatically identifies particles in the field of view based on the BEI compositional contrast and performs elemental analysis by EDS for each identified particle. After a number of particles in a field of view is are acquired, each particle is classified by the size, shape and elemental composition. It is also possible to automatically analyze in a large area by stitching many fields of view using stage movement.

In chapter 2.2, the elemental analysis of one inclusion was discussed in detail. However, there are a lot of tiny inclusions in the steel. Thus, it is needed to statistically analyze these inclusions. Particle analysis was demonstrated at an incident voltage of 15 kV and a probe current of 1.8 nA in a large area of 256 μm × 192 μm which was stitched by 10 × 10 fields of view. EDS spectrum of each inclusion was automatically acquired for 1.0 second and total acquisition time for all inclusions was 56 minutes. As a result, it was possible to calculate the size and element composition for 775 inclusions. Each inclusion was classified by the following conditions. First, the inclusion containing more than 0.1 mass% of Ti is Ti-class. Next, the inclusion containing more than 0.1 mass% of Al or calcium is Al and Ca-classes. The inclusion containing more than 0.1 mass% of S is S-class. The inclusion containing more than 5.0 mass% of Mn is Mn-class. Finally, the inclusion containing more than 0.1 mass% of Si is Si-class. The distribution of inclusions in the whole field of view is shown in **Fig. 10**(a). There are 2 inclusions of Ti-class, 3 inclusions of Al,Ca-class, 40 inclusions of S-class, 245 inclusions of Mn-class and 485 inclusions of Si-class. Average size of inclusions is 1.3 μm^2 of Ti-class, 5.1 μm^2 of Al,Ca-class, 0.02 μm^2 of S-class, 0.03 μm^2 of Mn-class and 0.008 μm^2 of Si-class (Fig. 10(b)).

Fig. 9 SXES spectra of steel inclusions.

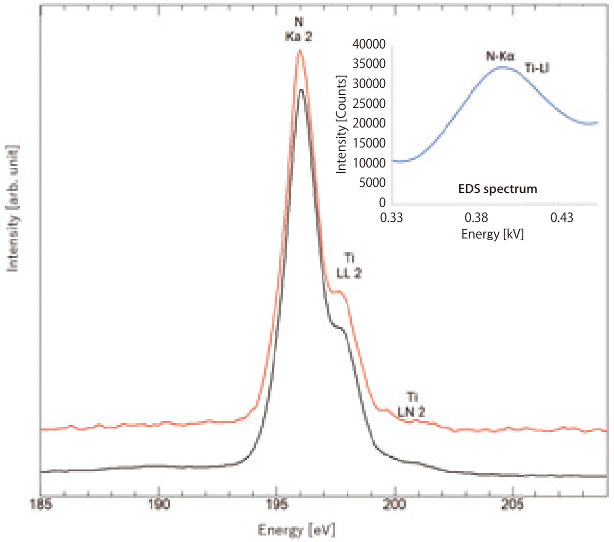

SXES spectrum of titanium (Ti) and nitrogen (N) segregated portions is displayed with red line, and the standard spectrum of TiN is displayed with black line. When compared with the EDS spectrum, it can be seen that the energy resolution is high and the N-Kα line and Ti-Ll line can be separated.

2.5 EBSD analyses

EBSD is one of the analytical methods for crystalline structures using SEM. EBSD patterns are able to be obtained by projecting backscattered electrons diffracted by the crystal planes of the specimen crystal onto the screen (**Fig. 11**) [4]. It is possible to obtain the crystal orientation map by scanning the specimen surface with an electron beam because the information of the crystal orientation is obtained from EBSD patterns. In addition, EBSD enables us to acquire not only crystal orientation but also crystal species, crystal grain size, shape and distortion. Therefore, it is widely used for analysis of metals, ceramics as well as steels.

Recently, CMOS sensors have been used instead of CCD sensors for capturing EBSD patterns. By CMOS sensors, the acquisition time is dramatically improved because the count rate for capturing EBSD patterns has been raised. On the other hand, a large probe current of several 10 nA to 100 nA is required in order to obtain clear EBSD patterns in high-speed acquisition.

EBSD crystal orientation mapping in the steel was carried out by using Symmetry (Oxford Instruments) which is equipped with CMOS sensors at an incident voltage of 15 kV and a probe current of 100 nA. First, a large area crystal orientation map of 2.35 mm × 2.64 mm was acquired, which automatically stitched 6 × 4 fields of view with a step size of 1 μm. EBSD patterns were obtained at high-speed with around 2600 patterns per second, and the acquisition time for total number of acquisition points (6,253,709 points) was for 54 minutes (**Fig. 12**(a)). High spatial resolution crystal orientation map of 130 μm × 95.4 μm was acquired with a step size of 50 nm. EBSD patterns were also obtained at high-speed with around 2,600 patterns per second, the acquisition time for total number of acquisition points (4,853,952 points) was 31 minutes (Fig. 12(b)). The combination of the latest EBSD system and JSM-IT800 enables us to acquire the crystal orientation maps of the steel in a large area or with high spatial resolution at high-speed.

Fig. 10 Particle analysis results of steel inclusions.

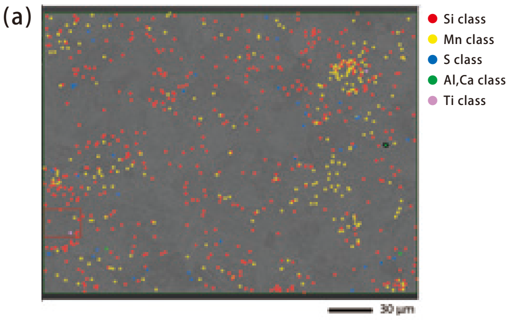

(b)

Class	Color	Number of particles	Average of size [μm^2]
Si	Red	485	0.008
Mn	Yellow	245	0.03
S	Blue	40	0.02
Al,Ca	Green	3	5.1
Ti	Purple	2	1.3

(a) Distribution of inclusions. (b) The number and size of inclusions.

Fig. 11 Positional relation between a specimen and an EBSD detector in a SEM chamber.

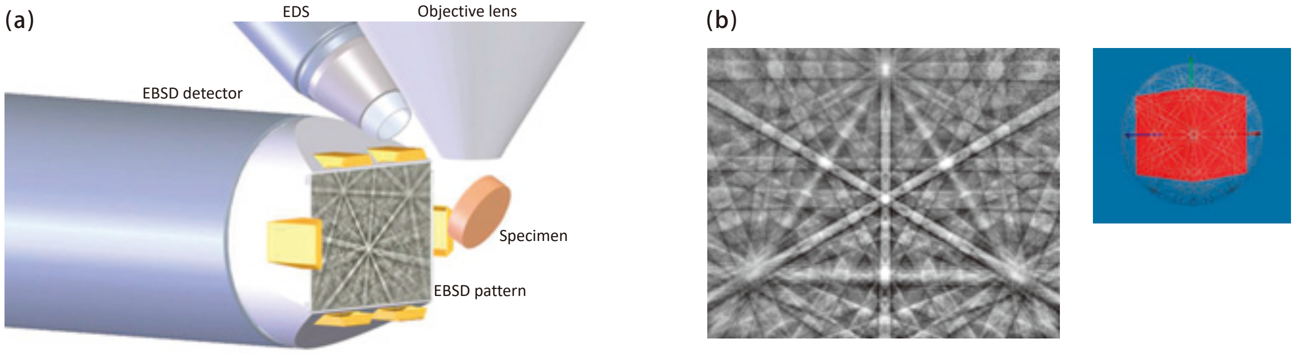

(a) The positional relation between a specimen and an EBSD detector in a SEM chamber. EBSD patterns are projected onto the screen of the EBSD detector.
(b) EBSD patterns of silicon single-crystal (111) plane.

Fig. 12 Crystal orientation maps of iron matrix grains in a steel material.

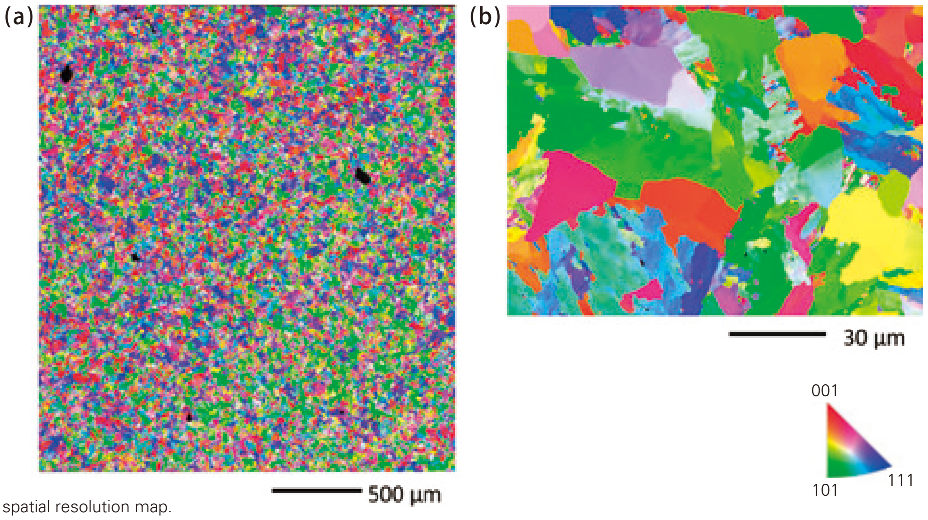

(a) Large area map. (b) High spatial resolution map.

Summary

In this paper, we showed the features of the new FE-SEM, JSM-IT800, and analysis examples using this SEM, which has capability of the diverse and high-quality high-throughput analysis.

Especially, about the EDS which has high affinity with the FE-SEM, we constructed the "EDS integration system" which integrates the control systems and GUI of the EDS with the FE-SEM. In addition, we showed that the time for the whole SEM operation can be greatly and efficiently improved by using together with Zeromag function for quick positioning and function of the SMILE VIEW™ Lab which enables users to prepare reports with minimum operation.

We showed some analysis examples of the JSM-IT800 using various analysis techniques for a steel specimen. Because the newly developed EDS integration system enables us to perform the SEM observation and the EDS analysis more easily and quickly, we can expect that there will be more opportunities for measurements using the SXES, the particle analysis and the EBSD. The JSM-IT800 is suitable not only for observations but also for various analyses such as the EDS, the SXES, the particle analysis, and the EBSD. Therefore, it is a high-performance multipurpose SEM which can satisfy the demands of not only the quality control mentioned in this paper but also other many applications.

Acknowledgments

We would like to thank Mr. Makoto Ikarashi of Oxford Instruments for their great cooperation in the provision of data.

References

[1] "Observation and Analysis at Low Accelerating Voltage Using Ultra High Resolution FE-SEM JSM-7900F", Hironobu Niimi, Yusuke Sakuda, Natsuko Asano, Shunsuke Asahina, *JEOL News*, vol.**54**, no.1, July, (2019).
[2] "Development of a sub-eV resolution soft-X-ray spectrometer for a transmission electron microscope", M. Terauchi, H. Yamamoto and M. Tanaka, *Journal of Electron Microscopy*, **50**(2), pp101-104, (2001).
[3] "Newly Developed Soft X-ray Emission Spectrometer, SS94000SXES", M. Takakura, T. Murano, and H. Takahashi, *JEOL News*, vol. **50**, no. 1, July, (2015).
[4] "Orientation imaging: The emergence of a new microscopy", B. L. Adamus, S. I. Wright and K. Kunze, *Metall. Trans*. A, **24A**, 819-831, (1993).

Introduction of Newly Developed Electron Probe Micro Analyzers

Kazunori Tsukamoto, Yuma Tanaka, Shinya Fujita,
Norihisa Mori, Takaomi Yokoyama, Shiori Kamijo
SA Business Unit, JEOL Ltd.

An electron probe microanalyzer (EPMA) is widely famous for a high-sensitive analytical instrument to detect some trace elements at about the 10 ppm level with a wavelength dispersive spectrometer (WDS), which can provide higher signal-to-noise ratio with about 100 times superior detection limit than an energy-dispersive X-ray spectrometer (EDS). To obtain such a higher performance of EPMA, all users have needed a basic and advanced training and had to learn all crystal properties (detectable energy ranges, energy resolution and sensitivity) in all WDSs. So, we have developed a new EPMA based on the concept of "provide easier and faster high-precision trace microanalysis" for all analysists who need higher quality/quantity analysis than EDS in all over the world. This paper introduces the JXA-*i*SP100 (integrated Super Probe) and the JXA-*i*HP200F (integrated Hyper Probe) in which high-precision trace microanalysis can be made easier and faster with various integrated functions, as we allude to in the equipment nickname "*i*".

Introduction

An electron probe microanalyzer (EPMA) is an analytical instrument to provide qualitative/quantitative analysis by detecting characteristic X-rays emitted from elements in a small (micro) surface area excited by a focused electron beam [1]. EPMA is one of the important tools to analyze elemental distribution of industrial materials and to evaluate its physical/chemical properties with elemental maps in scale of sub-micrometers to over several centimeters.

JEOL started developing EPMAs in the late 1950s, which was not so long time after the R. Castaing's thesis was issued [2]. Since then, we have continued with the development of many revolutionary technologies, such as the stage scan mapping analysis, synthetic layered dispersion elements (LDE), larger crystals, and Field Emission Electron Probe Microanalyzer (FE-EPMA). For example, it has become common for people to use the stage scan mapping function to analyze large areas today. But this method was developed by JEOL in 1970s for trace element mapping of centerline segregation in continuous casting steel, which required a few square cm analysis areas with a fast driving specimen stage [3]. In 1986, JEOL developed the first practical layered dispersion element crystals (LDE) which is a layered synthetic microstructure (LSM) for EPMAs. The LDE series dramatically improved the sensitivity of light element analysis [4]. The FE-EPMA was developed in the early 2000s collaborating with National Institute for Materials Science. Many people had long believed that the 1-micron scale was the limit of spatial resolution in an EPMA since we achieved sub-micron scale spatial resolution analysis by equipping the EPMA with a Schottky electron gun which can provide high brightness and high probe current even at lower kVs [5].

In this article, we introduce the newly developed EPMA series, the JXA-***i***SP100 (integrated Super Probe) and the JXA-*i*HP200F (integrated Hyper Probe). It is realized that both instruments have excellent features, ultimate performance with "ease of use" and expandability with various kinds of "integrated functions" such as integration of SEM observation and analysis, WDS and EDS analysis for which the "***i***" in the model name refers to.

Outline of Instrument

Regarding the newly developed EPMAs; JXA-***i***SP100 and ***i***HP200F, the external appearance is shown in **Fig. 1** and the specifications in **Table 1**, respectively. JXA-***i***SP100 attaches the high-quality electron gun with LaB_6 or W filament emitters as a general use EPMA. JXA-***i***HP200F, as a higher performance EPMA, allows more stable and higher spatial resolution using JEOL original designed "in-lens" Schottky-type field emission gun and always optimum aperture angle control system (ACL) corresponding to the probe currents.

These EPMAs are controlled by one PC system which provides various integrating functions EDS, WDS, cathodoluminescence detector and external JEOL XRF system. These data are easily output into an accomplished format. First new function; "Easy EPMA" makes it possible to take WDS results with the standardized measuring condition as little as 4 steps. Second new function, reasonable WDS setting procedure is sequentially supported by quicker EDS and XRF results. This combination method provides a reasonable accurate result in a limited time. Third new function; WDS trace analysis program supports to efficiently set the optimum WDS measurement conditions corresponding to the required trace contents.

〉〉 3-1-2 Musashino, Akishima, Tokyo, 196-8558, Japan | E-mail: ktsukamo@jeol.co.jp

These EPMAs are equipped with convenient handling functions such as; auto loading of the specimen holder, a stage navigation system in which the colored image of mounted specimen is taken by the inserted CCD camera, JEOL SEM's IT-series original function; "Zeromag" where the interesting analyzing point of view is smoothly searched from CCD to SEM images without switching, and "EDS live analysis" function which provides an elemental information with observing SEM image. These new handling functions kindly help from sample installation to searching the interesting analysis area. Moreover, in order to maintain the optimum calibration condition for WDS, newly designed built-in lump of 18 standards and new calibration procedure makes it possible to perform the steady and correct periodic calibration.

Improvements in basic performance

The JXA-*i*HP200F provides 3 µA as a maximum probe current. The stability of probe current is guaranteed under ± 0.3%/hr. and ± 1.0%/12 hrs. This performance is improved by a newly designed electron gun chamber attached with a getter pumping system for ultra-high vacuum quality. Regarding the electron optical control system, new engine has been developed so that the spatial resolution for secondary electron image has been improved to 2.5 nm at 30 kV.

EPMA control system

EPMA control system is constructed by two kinds of interface windows so-called "SEM Center" (**Fig. 2**) and "PC-EPMA2". "SEM Center" is popularly used for recent JEOL SEM's series, which provides various kindly handling functions. Including the recent "SEM Center" functions, EPMA can be utilized for easy operating functions such as "automatic specimen loading", kindly operating functions for electron images, JEOL EDS analysis such as real time "Live analysis", "Live map" intuitively provide elemental information with distribution, as well as an instant and quick WDS results are performed by the standardized procedure so-called "Easy EPMA" function. For fully fledged and flexible EPMA applications; qualitative, quantitative, line scan, mapping analyses, etc., PC-EPMA2 is performed for accurate and reliable data.

Fig. 1 External view of the JXA-*i*SP100 and the JXA-*i*HP200F

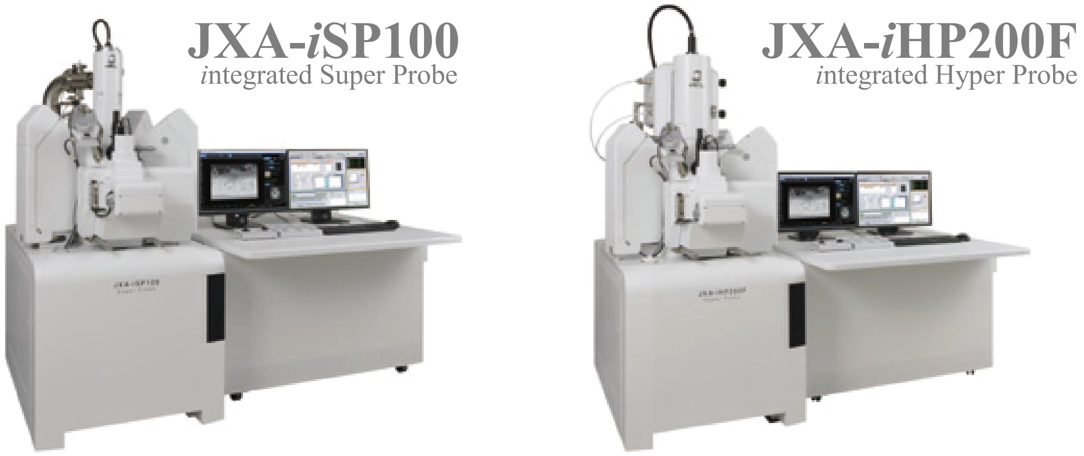

Table 1 Principal specifications of JXA-*i*SP100 and JXA-*i*HP200F

	JXA-*i*SP100	JXA-*i*HP200F
Electron GUN	W/LaB$_6$	In-lens Schottky Plus FEG
Elemental Analysis Range	WDS: Be/B to U, EDS: Be to U	
Number of X-ray Spectrometers	WDS: 1 to 5 EDS: 1	
Accelerating voltage	0.5 kV to 30 kV	
Probe Current	1 pA to 10 µA	1 pA to 3 µA
Current Stability	± 0.05%/hour, ± 0.3%/12 hours	± 0.3%/hour, ± 1.0%/12 hours
SEI Resolution at Analytical WD	6 nm (30 kV) (W) 5 nm (30 kV) (LaB$_6$)	2.5 nm (30 kV) 20 nm (10 kV, 10 nA) 50 nm (10 kV, 100 nA)

Instrument Features

Features of the JXA-*i*SP100/JXA-*i*HP200F are introduced in the order of:
"Setting", "Analysis", and "Self Maintenance".

Setting - Processes from specimen exchange to screening for areas of interest for analysis can be performed quicker and easier.

- Automated Specimen Loading and Stage Navigation System functions

The automated specimen loading function (**Fig. 3**) automatically drives the stage to the sample exchange position, evacuates the sample exchange chamber, captures a stage navigation image of the specimens in the holder, and loads the specimen holder onto the stage with a single click.

With the Stage Navigation System (SNS), the whole sample holder is imaged automatically at the time of sample exchange. This provides an optical image to navigate stage movement for finding the sample or area of interest, so that the time required to search and find the field of view can be shortened. In addition, with the Zeromag function (**Fig. 4**), which superimposes and displays the specimen holder optical image and SEM image, it becomes possible to seamlessly observe the specimen holder optical image at low Mag and the SEM image at higher Mag only by changing the observation magnification.

- Live Analysis / Live Map functions

The Live Analysis function of the EDS enables real-time screening of major elements contained in the field of view while observing the live SEM image (**Fig. 5**). Searching for the field of view of interest is now easier, as major elements appear in real time along with the secondary electron images and/or backscattered electron images.

It also has the Live Map function which can confirm the distributions of major elements in real time as an image (**Fig. 6**). In the Live Map window, the elemental distributions are always an overlay on the SEM image.

Since not only the secondary electron image and backscattered electron images, but also the main elements and maps can be displayed in real time, the efficiency of the searching for analysis areas is greatly improved.

- New Electron Optical System control engine

The implementation of the new electron optical system control engine improves the accuracy and speed of the auto focus function. High-resolution images can be acquired simply by using the "Auto" button. Any point specified by the

Fig. 2 "SEM Center" GUI of the JXA-*i*HP200F/JXA-*i*SP100

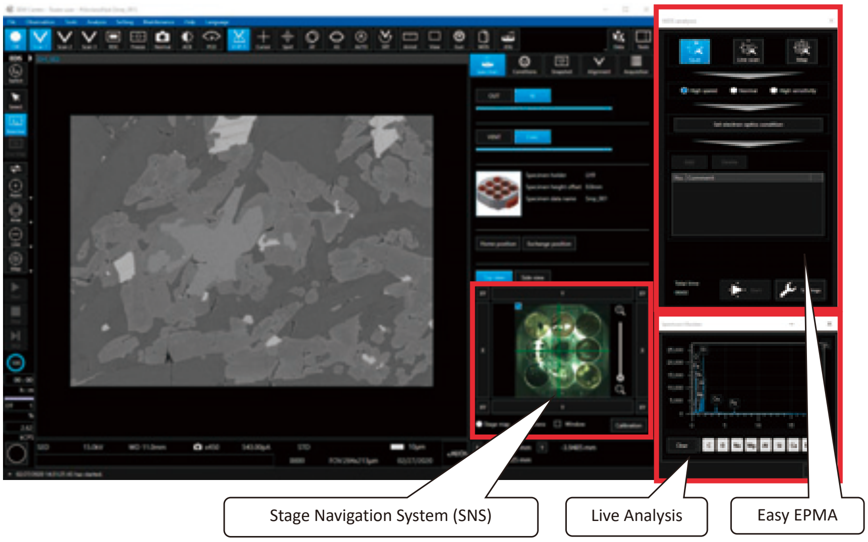

Fig. 3 Auto-Sample Loading + Stage Navigation System

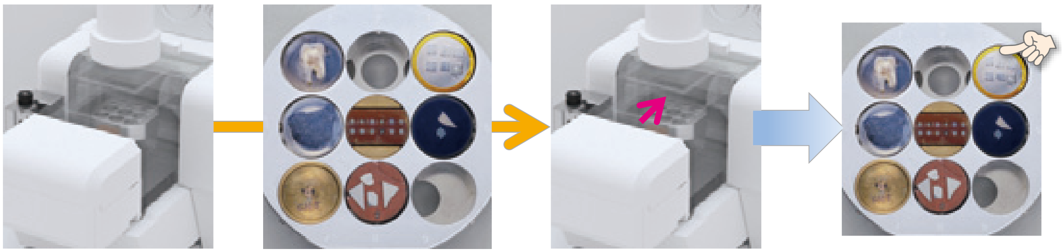
Automatic evacuation
Automatic acquisition of the holder image
The holder is automatically loaded onto the stage
Move to the desired sample or field of view

Fig. 4 Zeromag function

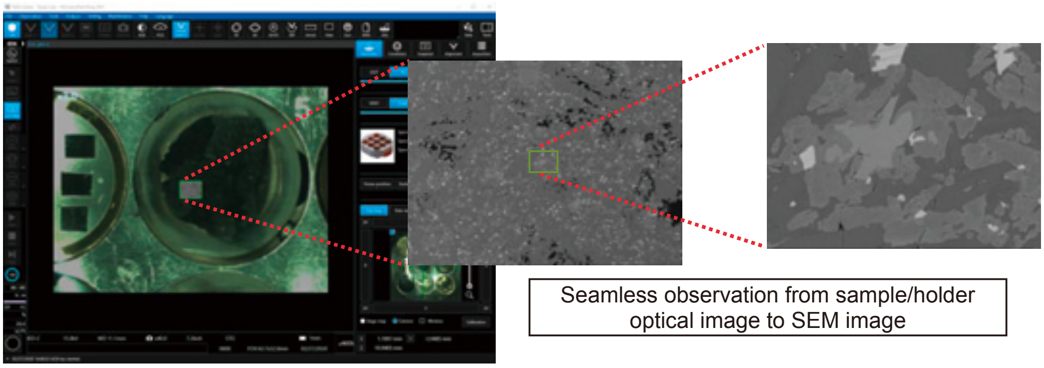

Seamless observation from sample/holder optical image to SEM image

Fig. 5 Live Analysis function with Spectrum Monitor window

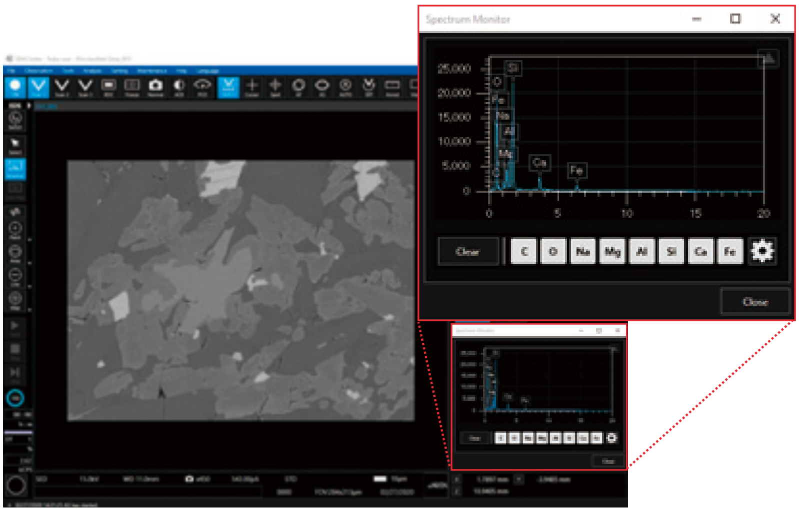

Fig. 6 Live Map window

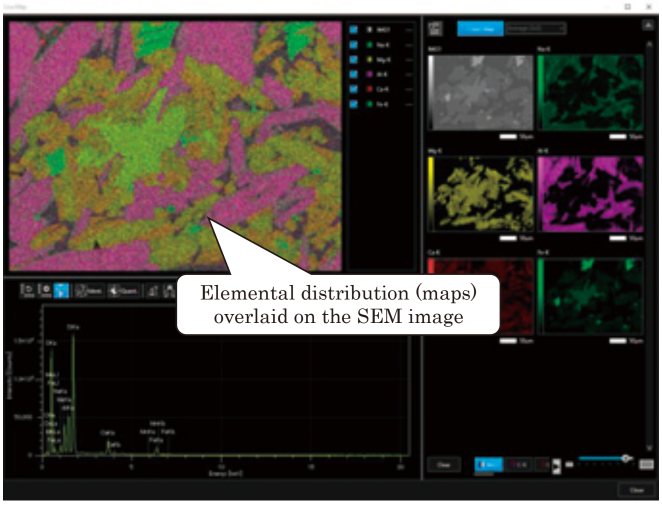

Elemental distribution (maps) overlaid on the SEM image mouse cursor can be focused as well. Auto focus is effective even for backscattered electron images as the bandwidth of the backscattered electron detector (BED-C, BED-T) is over twice as high as previous models. Users can identify the major elements in real time using the Live Analysis function described earlier and search for the target field of view while viewing live backscattered electron images easier than in the past (**Fig. 7**).

The probe current is instantly set with the new auto probe current function as well, using the setting history, in order to improve ease of use. These auto focus and probe current settings are enabled for the presetting of analysis conditions for sequential analysis and they can be automatically performed within an analysis sequence.

• OM Auto Focus

The OM Auto Focus function for automatically adjusting the specimen's height is now provided as standard (**Fig. 8**). The height of the specimen can be automatically adjusted via the OM Auto Focus to the optimum analytical position by presetting it in a sequence for sequential analyses or analysis of multiple points. It also can be manually enabled from the specimen stage controller.

• EPMA-OM Linkage System *miXcroscopy*™ *(option)*

Stage coordinates can be linked with Nikon optical microscopes. This enables users to easily search analysis points using polarized light observation and/or transmitted illumination of the optical microscopes, and perform analysis using the EPMA. This coordinate linkage can be connected to the JXA-*i*SP100/JXA-*i*HP200F.

Analysis - Perform Efficient and Accurate Elemental Analyses Easier

• Easy EPMA

"Easy EPMA" (**Fig. 9**) is the function that enables EPMA analysis with a simplified four steps procedures: 1) select analysis mode, 2) select measurement sensitivity, 3) register analysis position(s), and 4) register element(s).

Selecting an analysis mode from "Qual", "Line scan", and "Map" as well as the measurement accuracy and clicking "Set electron optics condition" automatically sets the optimum accelerating voltage and appropriate beam current. For the analysis position, the center of the screen is selected in qualitative analysis and the current field of view is selected from area (map) analysis.

• EDS, XRF, EPMA Integration

We have also developed an integration function for performing the trace element analysis with WDS, which loads the identified elements information from inner EDS as well as EDXRF (JEOL JSX-1000S), which can detect a few ppm level trace elements including into a several square mm of wide area. Using this function, EPMA beginner operators can start to measure its sample efficiently, because the appropriate spectrometers and analyzing crystals of WDS are automatically suggested based on this function (**Fig. 10**).

Our existing EPMAs can also perform the WDS/EDS integration map, which enables comprehensive data analysis. This system provides the maximum functionality for efficient data acquisition for a wide area stage scan map where all of the

Fig. 7 Effect of the new auto function (Specimen: Steel fracture surface, Accelerating Voltage: 15 kV, Magnification: ×3,000)

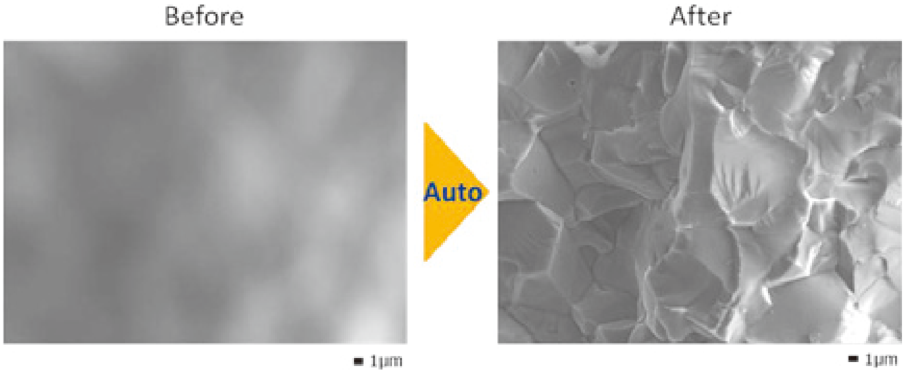

Fig. 8 OM Auto Focus being performed

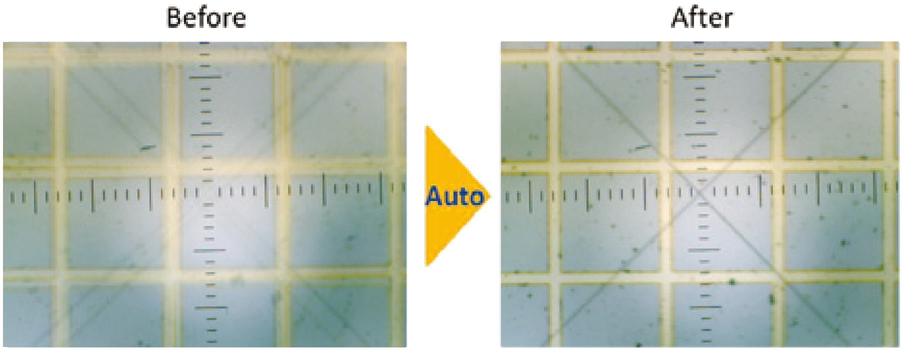

major elements can be mapped with EDS and up to five trace or minor elements can be mapped using WDS. An analysis example is shown in **Fig. 11**. During data acquisition, EDS spectral map data are automatically identified and constructed for each elemental distribution data. This system prevents elements from being overlooked. Moreover, these elements that have not been identified can be added by reconstructing the map data after measurement.

Self Maintenance – Easier Maintenance of Instrument Conditions

- 18 Stored "in-chamber" reference materials for spectrometer calibration

The JXA-*i*SP100 and JXA-*i*HP200F have stored a calibration specimen set for calibrating the WD/ED spectrometers mounted in the specimen chamber (**Fig. 12**). As the position of these calibration specimen sets are registered to the WD spectrometer calibration program, WD calibration can be performed easily without requiring any specimen exchange. Almost no maintenance is required even for Mg or Al whose surfaces tend to get oxidized.

And also, maintenance messages are displayed on the EPMA screen when maintenance is suggested for the mechanical drive units of the specimen stage, WDS, or other parts after some longtime operations, suggesting to the user to calibrate the spectrometer or take other necessary actions (see **Fig. 13**, this program is named as Customer Support Tool). The operator can always keep the instrument in good condition by regularly performing maintenance work such as WD calibration. JXA-*i*SP100 also has a function to monitor the operating time of the W filament or LaB_6 emitter and notify when it needs to be replaced before the end of filament lifetime.

Fig. 9 Easy EPMA

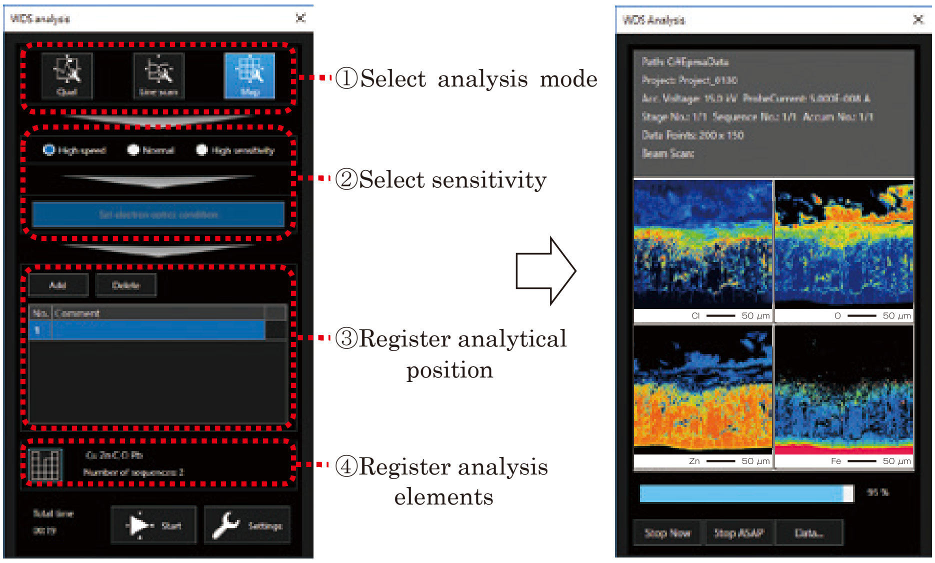

Path: C:\EpmaData
Project: Project_0130
Acc. Voltage: 15.0 kV ProbeCurrent: 5.000E-008 A
Stage No.: 1/1 Sequence No.: 1/1 Accum No.: 1/1
Data Points: 200 x 150
Beam Scan

Fig. 10 EDS, XRF-EPMA integration function

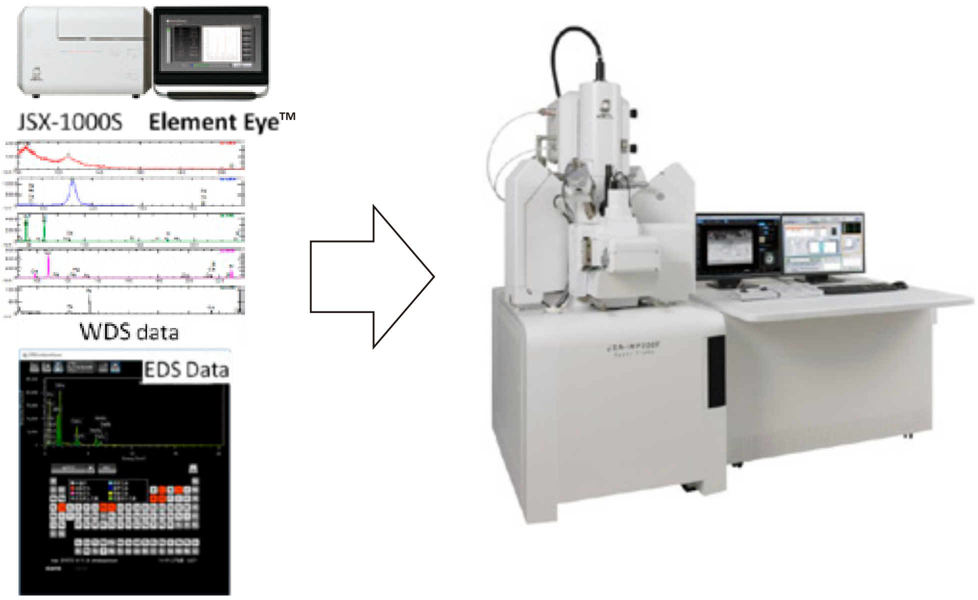

Analysis examples

To illustrate by an example analytical capability of XRF-EPMA integration system, we analyzed natural rock sample from the Okutama-Shiromaru mine including tokyoite micro grains. Tokyoite is vanadate mineral and the chemical composition is Ba_2Mo_3+$(VO_4)_2(OH)$, which was certified as a new mineral. Tokyoite is found as minute aggregate composed of very minute irregular grains under 15 µm in the sample from Shiromaru mine.

• Pre-analysis screening with an X-ray Fluorescence Analyzer XRF (XRF-EPMA Integration)

The rock sample from Shiromaru mine was mounted on hot mounting resin, and surface polished with sandpapers and diamond pastes (~1 µm). This sample was measured using JSX-1000S XRF analyzer capable of analyzing an area of several mm^2 in a short time for major to trace elements (**Fig. 14**). With a measurement of 1 minute, trace elements such as V, Ba, Rb and Sr in the rock sample were detected along with major elements (e.g. Si, Al. Ca and Fe).

The JXA-***i***SP100 and JXA-***i***HP200F can import result of quantitative analysis of JSX-1000S, and automatically select the appropriate analyzing crystals on the EPMA measurement for the identified elements by XRF.

• WDS-EDS Integration on the map analysis

WDS-EDS integration system enables acquiring elemental maps by EDS simultaneously with WDS mapping. For example, it is possible to assign the mapping of EDS for major elements, and WDS measurement with high S/N ratio for trace elements. This system can efficiently and rapidly analyze samples consisting of the large number of elements.

Energy resolution of spectrometer is at issue of peak interferences on X-ray emission spectrum. Tokyoite containing V and Ba, the V-Kα line and Ba-Lα line interfere with Ti-K line on the EDS measurement, due to the cause of misidentifying the characteristic X-rays of V as Ti. In the case of WDS, wavelength resolution is high enough to separation of Ti, V and Ba characteristic X-ray peaks (**Fig. 15**).

• Automatic Phase Map Generation

Phase Map Maker software can generate map of phases including analyte elements with single click. Phase classification is made by high-speed cluster analysis (HSCA) calculation. The phase map can be created from simultaneously acquired EDS and WDS map data. It is also possible to analyze the correction of each element in detail using the corresponding scatter diagrams (**Fig. 16**).

XRF and WDS-EDS integration system and Phase Map Maker software are possible to make a sequential analysis from the screening of the contained elements in the sample to the identification of phase structures as quickly and easily.

Fig. 11 Combined WDS and EDS maps collected with WDS/EDS integration (Specimen: Basalt from Mt. Fuji, Accelerating Voltage: 15 kV, Magnification: ×500)

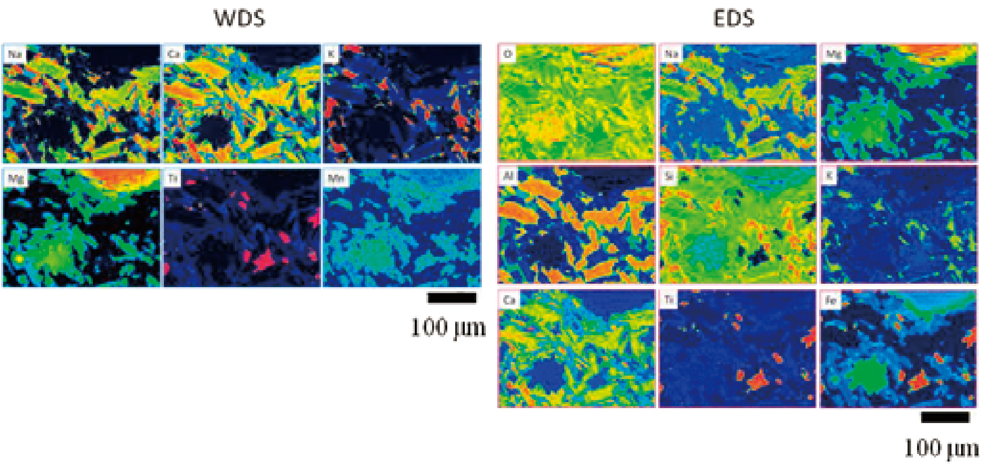

Fig. 12 Calibration specimens for WDS/EDS mounted on the specimen stage

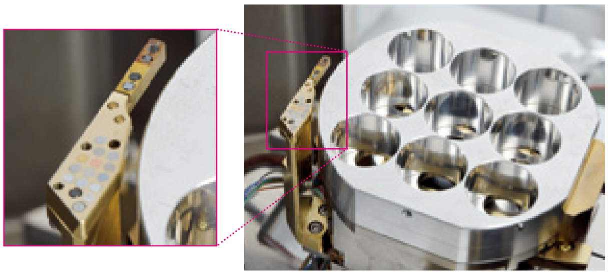

Fig. 13 Example of the customer support tool display

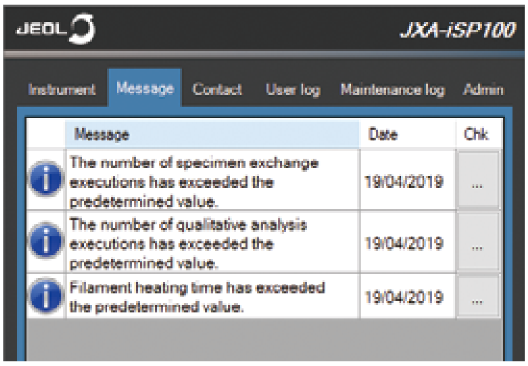

	Message	Date	Chk
i	The number of specimen exchange executions has exceeded the predetermined value.	19/04/2019	...
i	The number of qualitative analysis executions has exceeded the predetermined value.	19/04/2019	...
i	Filament heating time has exceeded the predetermined value.	19/04/2019	...

Fig. 14 XRF results from JEOL JSX-1000S of a rock sample including Tokyoite

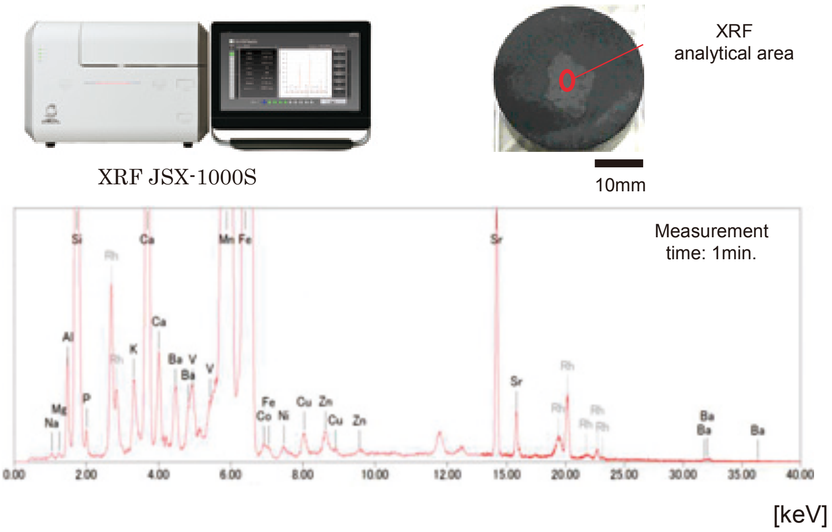

Elements	mass%
Na	1.2626
Al	2.2791
Si	12.3107
P	0.1420
K	0.3759
Ca	2.9747
V	0.1241
Mn	78.3310
Fe	0.5295
Co	0.0710
Ni	0.0650
Cu	0.0860
Zn	0.0894
As	0.0066
Rb	0.0027
Sr	0.7855
Mo	0.0066
Sb	0.0110
Ba	0.5466

Fig. 15 Combined WDS/EDS maps of a rock sample containing Tokyoite

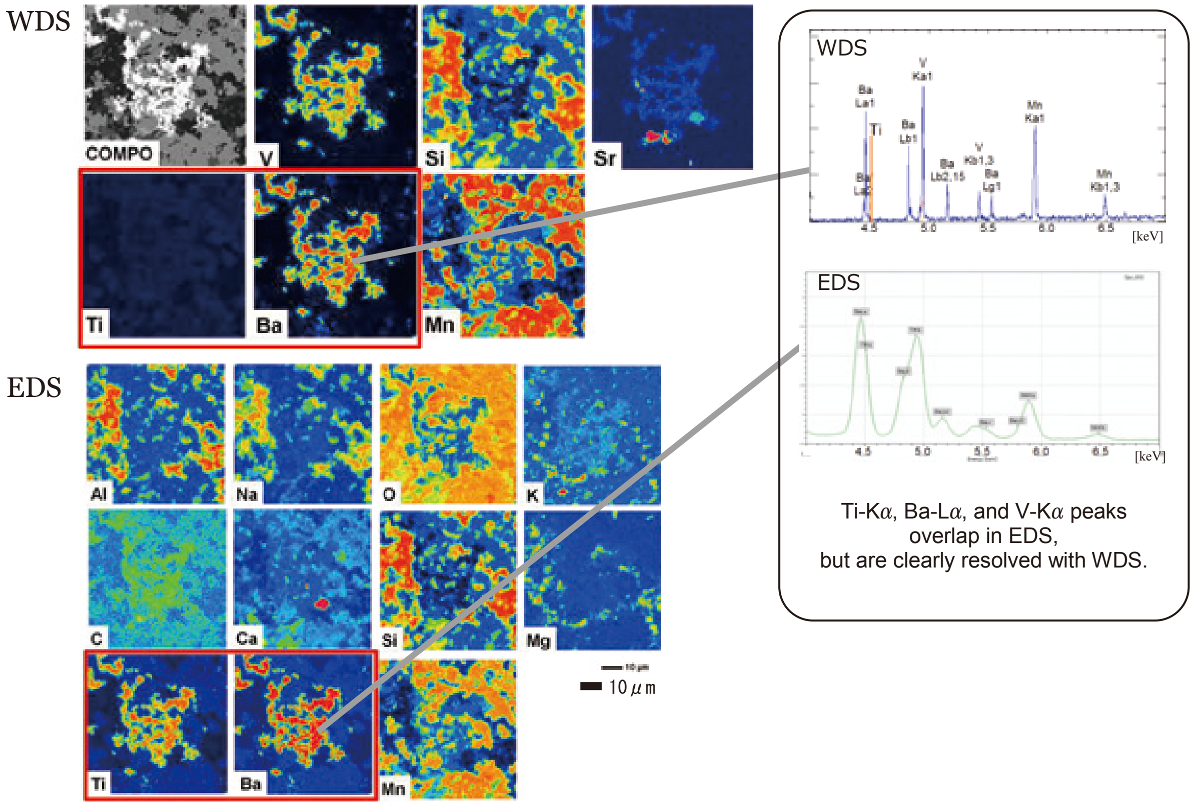

Ti-Kα, Ba-Lα, and V-Kα peaks
overlap in EDS,
but are clearly resolved with WDS.

Fig. 16 Phase map and scatter plots of a rock sample containing Tokyoite using Phase Map Maker

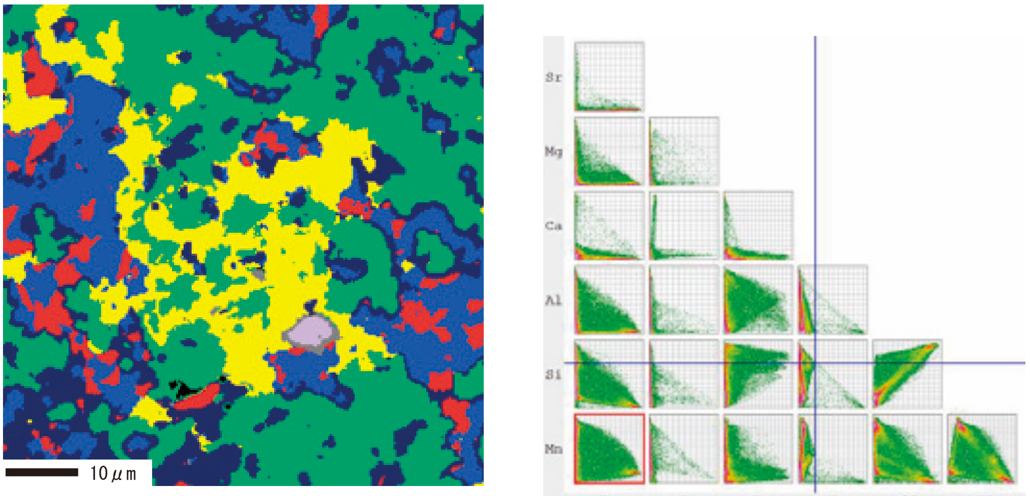

Phase map by high-speed cluster analysis (HSCA)

Scatter plots of X-ray intensity of each element

Summary

The features of new EPMA JXA-*i*SP100 and JXA *i*HP200F are summarized below.

Improvement of basic performance

The JXA-*i*HP200F provides 3 µA of maximum probe current. Probe current stability is ±0.3%/hr. and ±1.0%/12 hrs. The high probe current stability is due to an ion getter pump added to the electron gun chamber in order to achieve an ultra-high vacuum. A revised electron optics with the use of a new Electron Optical System control engine has improved the secondary electron image resolution to 2.5 nm at 30 kV.

Auto sample loader and stage navigation system

Auto sample loading system can be performed that processes from specimen introduction to acquisition of auto stage navigation image with just single click on mouse.

The stage navigation image shows the specimens positions in the holder so that users can easily move to the specimen and area of interest.

The Live Analysis function enables users to check elements in the field of view in real time with EDS while observing the live SEM image. This allows easy surveying for elements and the desired analysis field of view.

With the Zeromag function, an optical image of the sample is overlaid on the SEM image and is seamlessly connected and observed with changes of the observation magnification.

The EPMAs are equipped with an OM Auto Focus for accurately adjusting the height of the specimen to the analytical WD. The "ease of use" has been significantly improved with probe current setting and SEM image auto focus of which the accuracy and speed have been improved with the new Electron Optical System control engine.

Fast and easy setting of EPMA analysis

"Easy EPMA" is a function that enables EPMA analysis with a simplified four step procedures: 1) select analysis mode, 2) select measurement sensitivity, 3) register analysis position(s), and 4) register element(s).

Selecting an analysis mode from "Qual", "Line scan", and "Map" as well as the measurement accuracy and clicking "Set electron optics condition" automatically sets the optimum accelerating voltage and beam current.

EPMA analysis is simplified in EDS/XRF-EPMA integration system. Result of EDS or XRF analysis can be imported to EPMA operation software, and automatically set the analyzing crystals and detectors of EPMA. EDS measurement can simultaneously be made with WDS mapping analysis, and both data can be analyzed on the WDS/EDS integration system. In the Phase Map Maker software, the phase map is automatically generated with single click, and the identification of phase structure and comparing correlation of multiple elements are carried out with simple operation.

Easy maintenance

With 18 calibration standards, stored in place on the stage, the spectrometer can be easily calibrated.

A maintenance notification appears when calibration or maintenance is suggested; calibration and maintenance work can be performed at an appropriate time.

References

[1] "Electron Probe Microanalyzer" edited by the Surface Science Society of Japan, published by MARUZEN-YUSHODO Co., Ltd. (1998).
[2] R. Castaing: Ph. D. thesis, Univ. Paris (1951).
[3] S. Tagata: Ultra-high speed wide area multi-analyzer, "KINZOKU MATERIALS SCIENCE & TECHNOLOGY" extra edition (1984).
[4] K. Kawabe et al.: Coated multilayer dispersion element for X-ray microanalysis, Proc XI Int'l Congress Electron Microscopy (1986) p.569-570.
[5] H. Yamada, T. Okumura, T. Kimura and W. Knoll, Proc. of ICEM 15th DURBAN (2002) p.343.

High-Sensitivity, High-Throughput Analysis of Residual Pesticides in Foods by JMS-TQ4000GC Combined with Large-Volume Injection Technique and Fast-GC Method

Takao Fukudome MS Business Unit, JEOL Ltd.

The Gas Chromatograph (GC) Triple Quadrupole Mass Spectrometer (TQMS), the JMS-TQ4000GC, has a feature of high ion selectivity derived from tandem mass spectrometry same as conventional TQMS. In addition to that, JMS-TQ4000GC has two kinds of SRM (selective reaction monitoring) modes called as high-speed and high-sensitivity SRM mode that are achieved by JEOL's unique short collision cell technology. The combination of high-speed SRM mode of the JMS-TQ4000GC and Fast-GC method with large volume injection (LVI) technique was applied for the analysis of residual pesticides in foods.

This combination method of high-speed SRM and Fast-GC with LVI technique could achieve the detection of 1 ppb concentration level for residual pesticides that correspond to on-tenth of standard criterion in positive list system with reducing the total measurement time to less than 15 minutes that corresponds to half of the measurement time with conventional method.

Introduction

The criterion called 'Positive list system' that was introduced by the ministry of health, labor and welfare, Japan in 2006 [1] regulates the residual level in food for approximately 800 kinds of pesticides. There are difficulties to detect the trace amount of various kinds of pesticides in the complex matrix. This is one reason why GC-TQMS system that can provide higher selectivity than the GC-single quadrupole MS system is mainly used for the residual pesticides analysis. On the other hands, the high-through-put capability is also required for the residual pesticides analysis in foods because many amount of samples should be analyzed for the limited time period. In the case of the pesticides analysis in water sample, FastGC technique used to be used to improve the time consuming situation. However, it was difficult that FastGC technique would apply to the residual pesticides analysis with GC-TQMS because it takes a certain period for ion transition in the collision cell of conventional GC-TQMS system.

The unique features of the JMS-TQ4000GC (**Fig. 1**) are the two kinds of SRM measurement mode called "high-speed SRM mode / high-sensitivity SRM mode" that could be achieved by JEOL's unique collision cell technology (patent No.: US8692191, EP2469578, US8604420). The "high-speed SRM mode" could be useful for the screening analysis for many kinds of target compound that gives weight to the high-through-put capability. On the other hands, the "high-sensitivity SRM

Fig. 1 External appearance of JMS-TQ4000GC

›› 3-1-2, Musashino, Akishima, Tokyo, 196-8558, Japan | E-mail: tfukudom@jeol.co.jp

mode" should be applied for the measurement that gives weight to the sensitivity and accuracy of measurement, and it is also useful for the accurate quantitative analysis for the focused target compounds that were sorted out by screening analysis with the "high-speed SRM" mode. It was reported that the high-through-put analysis at 10 ppb level corresponding the regulated concentration level of the criterion could be achieved within 15 minutes by using the combination of Fast-GC technique and the "high-speed SRM" mode of JMS-TQ4000GC [2]. The results were reported in this article that the combination of high-speed SRM mode and Fast-GC with LVI technique applied to the measurement of the 1 ppb concentration level (equivalent to one magnitude lower than 10 ppb) within 15 minutes.

Features of Hardware

Overview of "short collision cell"

The overview of the short collision cell is illustrated in **Fig. 2**. The length of this innovative short collision cell is 15 mm in total length, which is as short as one-tenth of the conventional ion-guide. This feature dramatically shortens the ion ejection time from the collision cell, for compromising fast SRM measurement and avoiding the interfering ions (cross-talk). Also, continuous ion accumulation and instantaneous ejection of the accumulated ions within the collision cell makes the ions into pulses, and data acquisition only for the time of ejection of these ion pulses leads to accomplishment of noise reduction and enhanced detection sensitivity.

Ion accumulation

For ion accumulation within the collision cell, the short accumulation mode (High Speed mode) and the long accumulation mode (High Sensitivity mode) are selectable. In the High Speed SRM mode, the fast SRM measurement up to 1,000 channels can be achieved though the sensitivity enhancement is limited due to the short ion accumulation time and the short noise elimination time. On the other hand, in high sensitivity mode, the sensitivity enhancement can be expected based on the effect of long noise elimination time that is induced by long ion accumulation time though the switching speed of SRM channels is limited up to 100 channels per second (**Fig. 3**).

Experiments

Outline

292 kinds of pesticides were measured by using the combination of high speed SRM mode of JMS-TQ4000GC and FastGC condition. The large volume of sample solution (20 µL) could be applied to the GC-TQMS system because the LVI-S200 (AiSTI SCIENCE) was installed to the GC injection port as a large-volume injection system.

Samples

Standard pesticide mixture solutions (PL1,2,3,4,5,6,9,10,11, 12,13; FUJIFILM Wako Pure Chemical Corporation) were used for measurement. Spinach and a fruit tart as real sample were processed according with STQ method. Two kinds of spiked sample solution for spinach and fruit tart were prepared by spiking the standard solution to the extracted solution so that the final concentration of each pesticides could be 1 ppb and 100 ppb.

The 1,000 ng of polyethylene glycol (PEG300) was spiked to the standard solutions for calibration curves to avoid the adsorption of pesticides on the glass insert of GC injection port.

GC condition

Injection port: LVI-S200 (AiSTI SCIENCE) as a large-volume injection system
Injection mode: Solvent Vent
Injection volume: 20 µL
Injection port temperature:
100 °C (0.1 min) → 260 °C (120 °C/min, 3 min) → 280 °C (20 °C/min, 9 min)

Fig. 2 Overview of short collision cell

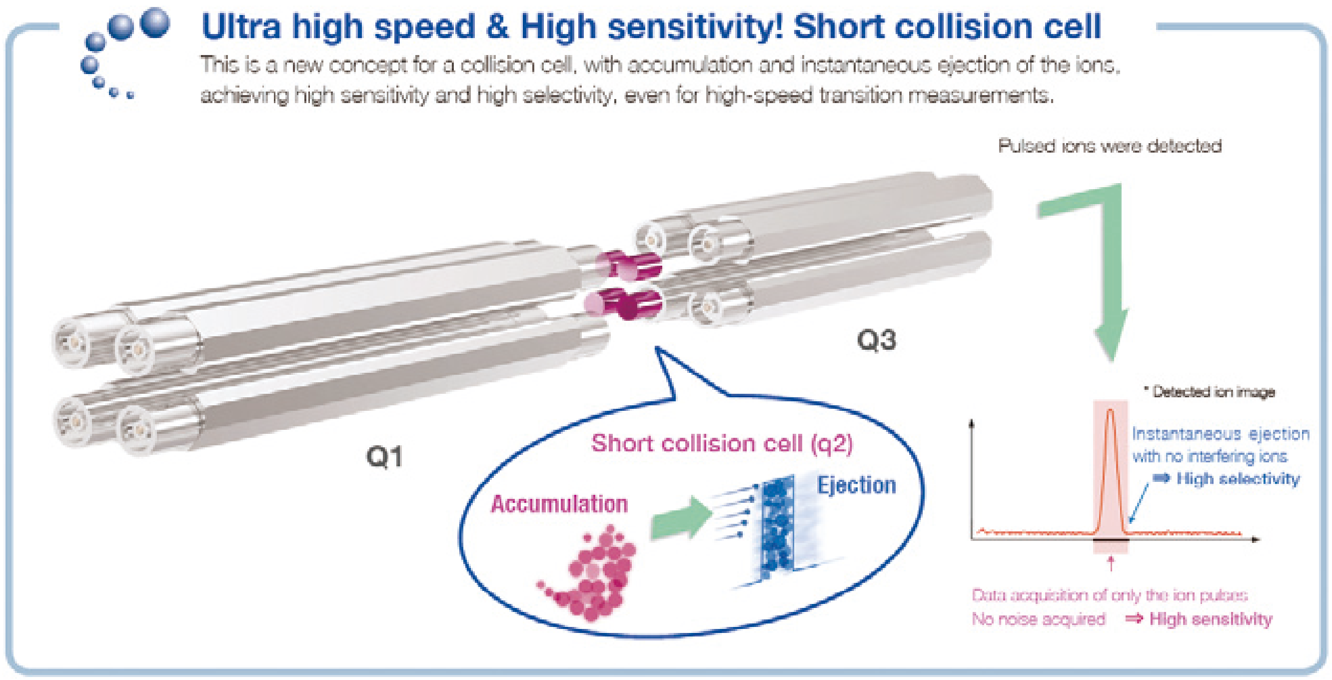

(Patents : JP5296505, US8692191, EP2469578, US8604420)

Oven: 0 °C (3 min) → 50 °C/min → 120 °C (0 min) → 30 °C/min → 300 °C (4.6 min) (total: 15 min)
Column: DB-5ms (Agilent Technologies), 20 m × 0.18 mm, 0.18 µm
Column control mode: Constant Flow
Column flow rate: 0.7 mL/min

MS condition

Triple QMS: JMS-TQ4000GC (JEOL)
Ionization condition: EI, 70 eV (50 µA), 280 °C
GC interface temperature: 300 °C
SRM mode: High Speed

Results and Discussion

Total ion current chromatograms (TICCs) as measurement results of the 1ppb standard solution, 1ppb spiked sample solution of spinach and 1ppb spiked sample solution of fruit tart were shown in **Fig. 4**. All pesticides were eluted within 15 min under the FastGC condition described before. It means that 15 min total measurement time under FastGC condition correspond to almost half of the measurement time by using conventional GC condition issued by Ministry of Health, Labor and Welfare, Japan [2].

The extracted ion chromatograms (EICs) for 4 kinds of

Fig. 3 Overview of ion accumulation

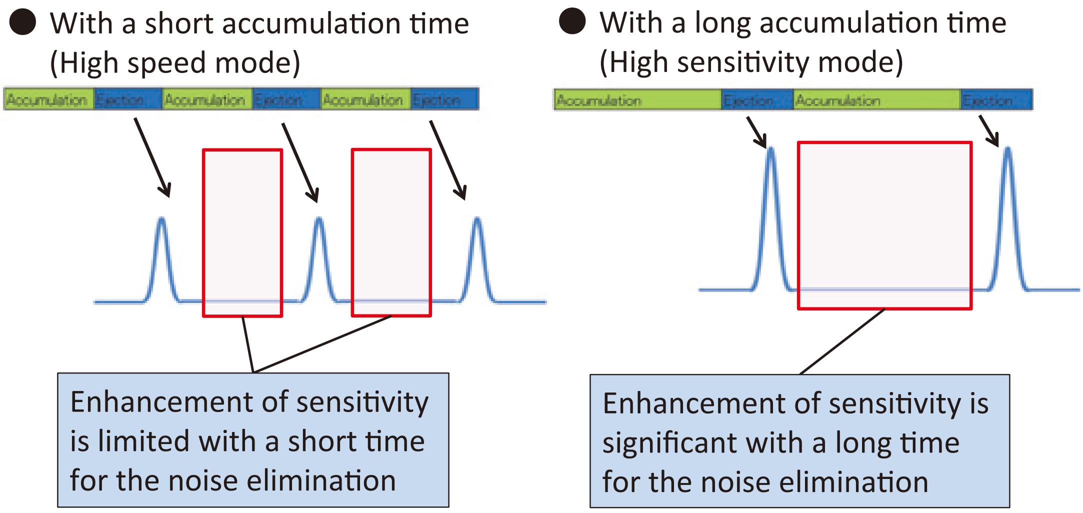

Fig. 4 Total ion current chromatograms of standard solution at 1 ppb concentration and the spinach and fruit tart samples to which the standard samples were spiked at 1 ppb concentration.

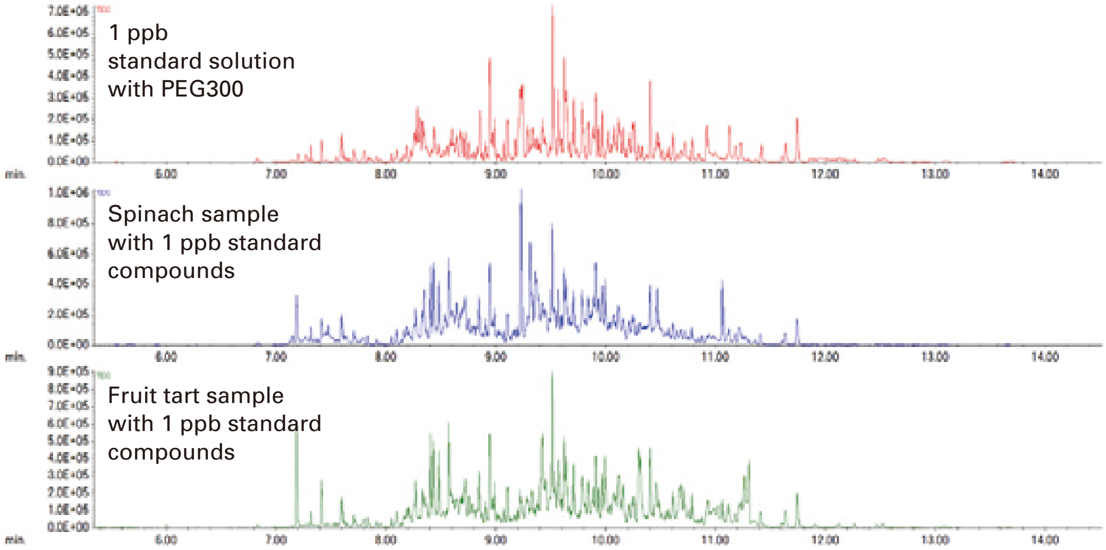

pesticides that were obtained from 1ppb standard solution and 2 kinds of spiked solution were shown in **Fig. 5**. Almost peaks of 292 pesticides on TICCs were overlapped and were not separate enough at chromatographic point of view due to the very short measurement time of FastGC condition. However, each peak corresponding to the pesticides on EICs could be clearly detected due to the high selectivity of SRM measurement by GC-TQMS. Although the abnormal baseline fluctuation and the several ghost peaks that were not found in EIC of standard solution were observed in EICs due to the huge amount of matrix compounds in the real samples, the detection of those clear peaks for the target pesticides suggested that the high speed SRM mode of JMS-TQ4000GC could work correctly without any influence of cross-talk even under the high speed SRM switching condition. Approximately 50 kinds of pesticides or more needed to be monitored at the same time under this FastGC condition. Since two kinds of SRM channels has to be monitored for 1 kinds of pesticide, 100 SRM channels or more has to be monitored at same time for more than 50 kinds of pesticides. In addition, high speed SRM switching capability is required to keep the enough data points for the very sharp shape peak by Fast GC condition. For instance, if 5 data points per second as data acquisition speed is necessary, the SRM switching speed more than 500 SRM channels per second is also necessary as the instrument specification of GC-TQMS. For this reason, JMS-TQ4000GC that can achieve the high speed SRM switching, 1000 SRM channels per second was able to be applicable for this type of measurement that requires both capability of multicomponent analysis and FastGC simultaneously.

Concerning the two kinds of spiked samples (1ppb), the distribution of the coefficient of variation (CV) values of peak area corresponding to each pesticide were summarized in **Fig. 6**.

Fig. 5 SRM chromatograms of standard solution at 1 ppb concentration and the spinach and fruit tart samples for 4 kinds of pesticides.

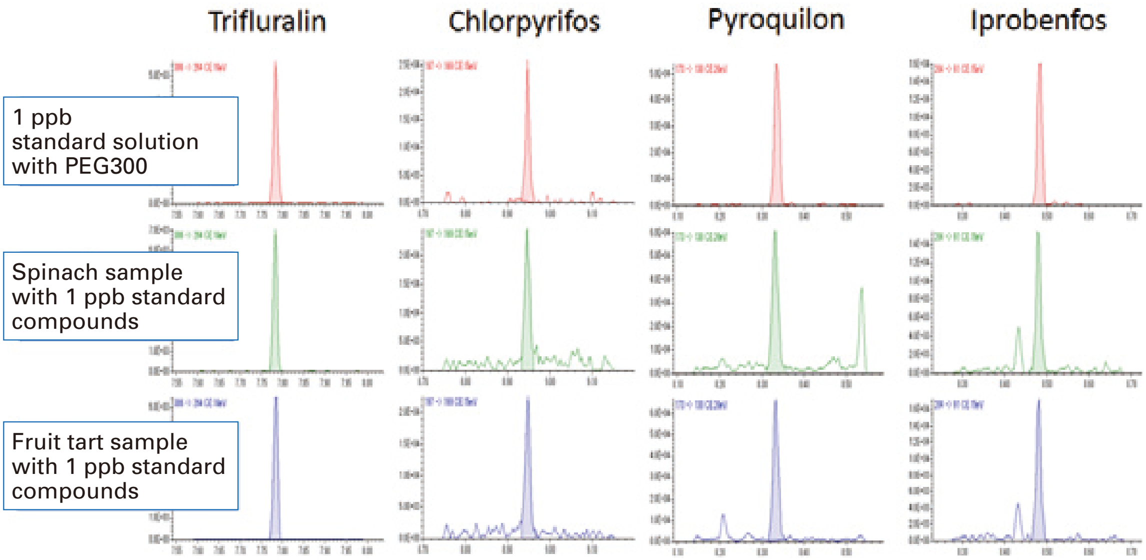

Fig. 6 Distribution of coefficient of variation values of peak area corresponding to each pesticide in the spinach and fruit tart samples to which the standard sample were spiked at 1 ppb (n=8)

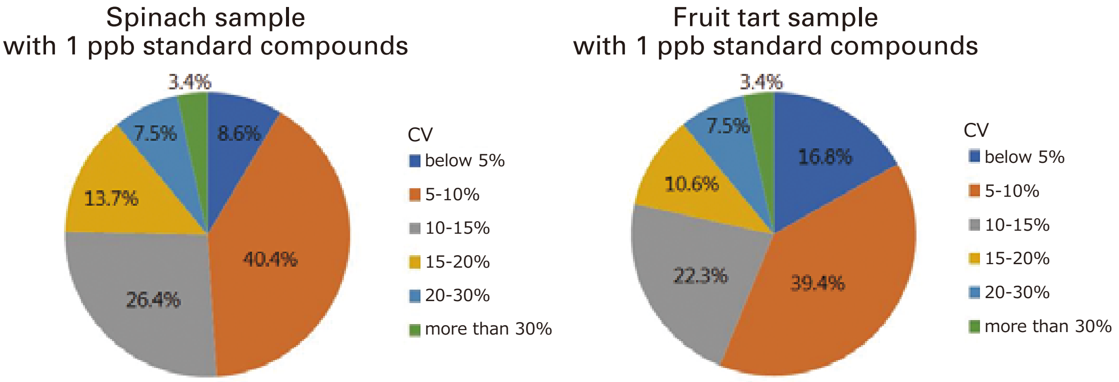

The CV values corresponding to almost 90% of 292 pesticides were below 20%. The CV values corresponding to 49% of 292 pesticides (in case of spinach) and 56% (in case of fruit tart) were less than 10%.

The distribution of the detection limit values corresponding to 292 pesticides that were estimated from the CV values were shown in **Fig. 7** for both of spinach and fruit tart samples. The values of the instrumental detection limit for 81.5% of 292 pesticides (in case of spinach) and 83.6% (in case of fruit tart) were able to achieve to less than 0.5 ppb. In addition, the value of detection limit for the 97.6% of 292 pesticides in both case of spinach sample and fruit tart sample were below 1ppb. These results suggested that the FastGC measurement condition consisted of the high speed SRM mode of JMS-TQ4000GC and the large volume injection system of LVI-S200 (AiSTI SCIENCE) could achieve enough sensitivity required for the residual pesticides analysis in food.

The distribution of the coefficient of determination for calibration curves of 292 pesticide was shown in **Fig. 8**. For the calibration curves between 1 ppb and 100 ppb, the coefficient of determination was found to be 0.990 or higher for 93.8% and 0.995 or higher for 86.3% of 292 pesticides.

Conclusion

As the result of multicomponent analysis of 292 kinds of pesticides by JMS-TQ4000GC combined with Fast GC method and the large volume injection technique, it was found the total analysis time could be reduced to 15 min. The CV values of the peak areas of the spiked samples (1ppb) for 90% of 292 pesticides were less than 20%. And the detection limit value estimated from those values of the spiked samples (1 ppb) were below 1ppb for 97.6% of 292 pesticides. The coefficient of determination of the calibration curves from 1ppb to 100ppb concentration about 93.8% of 292 pesticides could be achieved more than 0.990. Those results suggested the measurement method by JMS-TQ4000GC combined with Fast GC and the large volume injection technique was able to make high sensitivity (the detection limit less than 1 ppb) consist with high through put (15 min as total measurement time).

References

[1] Ministry of Health, Labor and Welfare, Japan; Homepage (in Japanese), https://www.mhlw.go.jp/stf/seisakunitsuite/bunya/kenkou_iryou/shokuhin/zanryu/index.html

[2] Nihondenshi news (in Japanese) **vol.51 No.1**, (2019), p58-64.

[3] Ministry of Health, Labor and Welfare, Japan; Notification test method, “Comprehensive analysis methods of pesticides in agricultural foods using GC/MS” (in Japanese).

Fig. 7 Distribution of instrumental detection limits value corresponding to 292 pesticides for spiked samples.

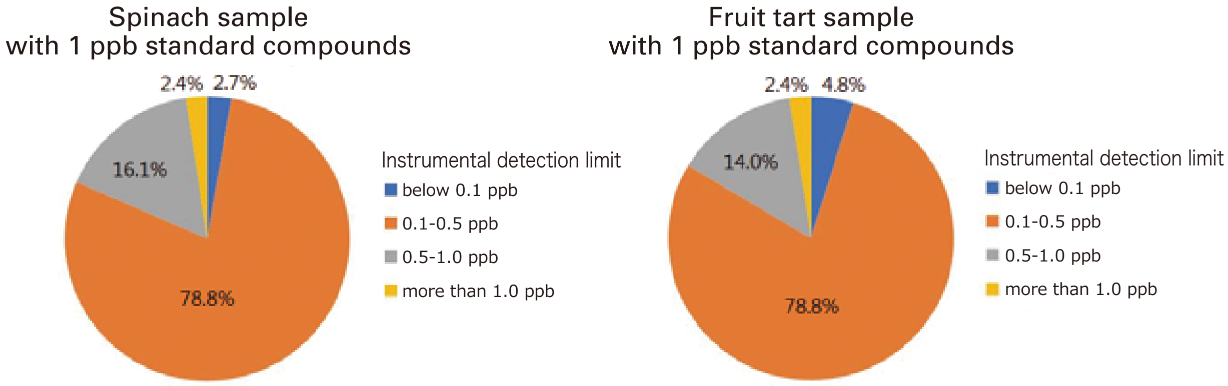

Fig. 8 Distribution of the coefficient of determination for calibration curves of 292 pesticides.

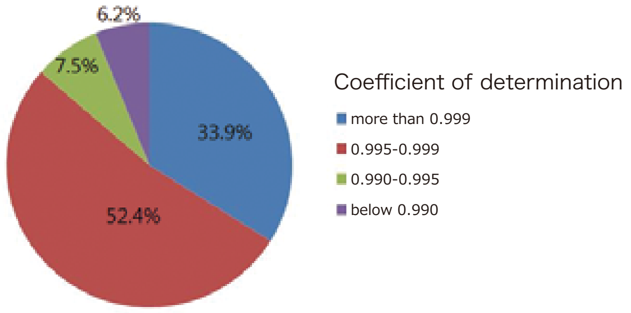

Mass Spectrometry Imaging using the JMS-S3000 "SpiralTOF™-plus" Matrix Assisted Laser Desorption Ionization Time-of-Flight Mass Spectrometer

Takaya Satoh MS Business Unit, JEOL Ltd.

Matrix assisted laser desorption/ionization (MALDI) is one of the soft ionization methods. By selecting a proper compound to enhance the ionization efficiency (called "matrix"), various kinds of organic compounds can be ionized. In 2010, JEOL released the JMS-S3000 "SpiralTOF™", which adopted a spiral ion optics system combined with MALDI ion source. In recent years, MALDI-TOFMS (time-of-flight mass spectrometer) has been widely used for mass spectrometry imaging (MSI) to visualize the localization of target compounds on the sample surface. The SpiralTOF™ is a suitable system for MALDI-MSI because it can achieve high mass-resolution even in low mass region, which was difficult by the conventional reflectron TOFMS. In 2019, JEOL has introduced the new "SpiralTOF™-plus", which has improved the data acquisition speed while keeping the inherent high mass-resolution. This report presents the features of the SpiralTOF™-plus and the advantages in practical applications using this system.

Introduction

In the Matrix Assisted Laser Desorption Ionization (MALDI), co-crystals of the matrix and sample compounds are made by spotting the mixture of their solutions on the target plate and air-dried. The ultraviolet laser is irradiated on the co-crystal to ionize the sample. By selecting the suitable matrix according to the sample, it is possible to ionize variety kinds of organic compounds, including proteins, peptides, nucleic acids, glycans, lipids, drugs and synthetic polymers. Using MALDI, ions with wide-molecular weight can be generated as singly charged ions. Also, the MALDI is a pulsed ionization technique, and it is best match to combined with a time-of-flight mass spectrometer (TOFMS). The MALDI is difficult to online-connect with a chromatography system (gas chromatography, liquid chromatography, etc.), and separation of compounds included in sample depends on the mass resolution of TOFMS. However, mass resolution of conventional reflectron TOFMS is often insufficient, especially for low mass range. It is even said that the reflectron TOFMS cannot be applicable to analyzing the compounds of molecular weight 500 or less. Another reason is that, the Post Source Decay (PSD) ions which originated from spontaneous decay are detected as the noise in the low molecular range, thus making it difficult to detect minor components. In order to solve this issue, JEOL introduced the MALDI-TOFMS system, the JMS-S3000 "SpiralTOF™" in 2010. With its unique spiral ion optics system, the SpiralTOF™ achieved a 17 m-long flight path in a limited space. Thus, the SpiralTOF™ successfully provided ultrahigh mass-resolution and ultrahigh mass accuracy. Another feature of this ion optical system is consisted of four electrostatic sectors, which enables to eliminate PSD ions and makes easy to detect minor components. Owing to these features and advantages, it became possible to perform analysis for the low molecular range with high mass-resolution and high mass accuracy, which was difficult to do with the reflectron TOFMS. Recently, MSI (mass spectrometry imaging), which can visualize the distribution of organic compounds on the sample surface, is becoming practical. Most of the target compounds for MSI analyses are low molecular compounds so that SpiralTOF™ has an advantage due to its high analytical capability in the low molecular weight range. In the latter half of 2019, the SpiralTOF™ was upgraded to the "SpiralTOF™-plus". This powerful SpiralTOF™-plus inherits the features of high mass-resolution capability of the SpiralTOF™ and has improved capabilities of MSI. In this report, the features and advantages of the SpiralTOF™-plus will be presented, along with its effectiveness in practical analysis applications.

Features of SpiralTOF™-plus

Figure 1 shows the appearance of the SpiralTOF™-plus and the schematic of the spiral ion optics system. The SpiralTOF™-plus adopts a long-life solid-state laser for ionization, accomplishing fast measurement. The sample ionized in the MALDI source is accelerated to mass separation in the 8-shaped spiral ion optics system which is composed of four electrostatic sectors with eight stories. After one cycle, the ion trajectory is shifted perpendicular to the orbit plane, and thus the spiral orbit is formed. The flight path of one cycle is 2.1 m so that the total flight path extends to 17 m. It is five times longer than that of the reflectron TOFMS. This demonstrates that high mass-resolution is achieved over a

〉〉 3-1-2, Musashino, Akishima, Tokyo, 196-8558, Japan | E-mail: taksatoh@jeol.co.jp

Fig. 1 Appearance of SpiralTOF$^{\text{TM}}$-plus and schematic of a spiral ion optics system.

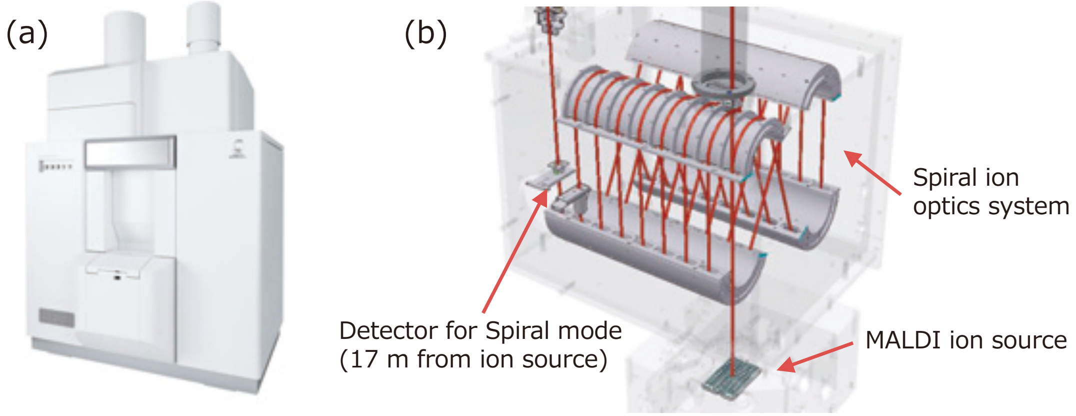

wide mass range. MALDI is one of the major ionization methods, as well as electrospray ionization (ESI). However, MALDI is also known to cause spontaneous fragmentation (called PSD) by excessive internal energy generated at the ionization. The kinetic energy of fragment ions becomes smaller than that of precursor ions. Since the electrostatic sectors have an ability as a kinetic energy filter, the ions derived from PSD with reduced energy cannot pass and these ions are ejected from the ion orbit. As a result, the noise derived from PSD is not detected in a mass spectrum, and thus even trace components can be easily detected.

Mass Imaging (MSI)

In MALDI-MSI, a tissue section (thickness is generally 10 µm or less) is placed on a conductive ITO slide glass, and a matrix solvent is uniformly sprayed using an air-brush, from above the glass. A laser beam is irradiated two dimensionally on the sample surface for acquiring mass spectra from each pixel. After data acquisition, localization of the target compound, which is specified by the peak in mass spectrum, is visualized (see **Fig. 2**). Several MS systems are commercially available for MALDI-MSI. In **Fig. 3**, comparison is made between the mass resolution and data acquisition speed. As described before, the SpiralTOF$^{\text{TM}}$-plus provides higher mass-resolution than the reflectron TOFMS and the SpiralTOF$^{\text{TM}}$-plus can separate isobaric peaks. In terms of data acquisition speed, the SpiralTOF$^{\text{TM}}$-plus is comparable to the reflectron TOFMS. On the other hand, FT-ICR or FT-MS, which has higher mass resolution than TOFMS, is also used for MALDI-MSI. However, an increased data acquisition speed will lead to reduction of mass resolution. Since the mass resolution and data acquisition speed is independent in TOFMS, SpiralTOF$^{\text{TM}}$-plus can achieve optimal combination of high mass-resolution and high-speed acquisition.

Fig. 2 Conceptual view of MALDI-MSI (mass imaging).

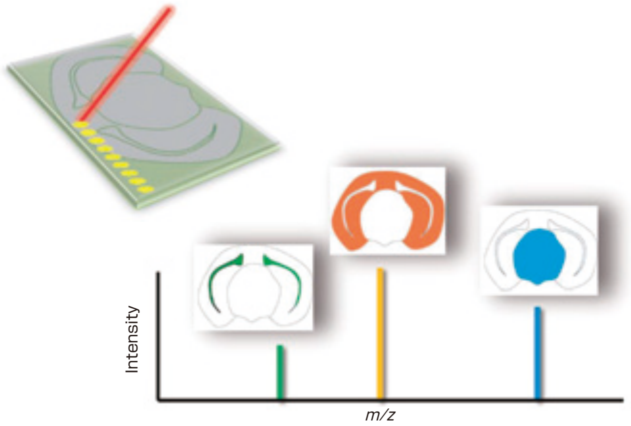

Improvements and Advantages of SpiralTOF$^{\text{TM}}$-plus

The SpiralTOF$^{\text{TM}}$-plus has improved the data acquisition speed for MALDI-MSI to 3 times at a maximum, compared to the conventional SpiralTOF$^{\text{TM}}$. Furthermore, the SpiralTOF$^{\text{TM}}$-plus has increased the maximum number of pixels for measurement from 32,000 points to 200,0000 points. In MALDI-MSI, the sample preparation (making tissue sections and selecting matrix selection) and confirmation of reproducibility take the most time. The present improvements of the SpiralTOF$^{\text{TM}}$-plus has greatly enhanced the efficiency of these processes due to an improved data acquisition speed. In many cases in MALDI-MSI measurement, the size of the pixel is set to 20-50 µm due to enough sensitivity to get. The increase of the maximum number of pixels of SpiralTOF$^{\text{TM}}$-plus allows to acquire the data even from a small sample of a few cm squares under the same acquisition conditions. In **Fig. 4**, the mass images of PC (38:4)[M+K]$^+$(*m/z* 848.557) and Galactosyl ceramide (C24h:1)[M+K]$^+$(*m/z* 848.638) from a a mouse brain tisseu section are shown. These two lipids have only a mass difference of 0.1 u, which cannot be separated with the reflectron TOFMS. By comparing these two mass iamges made by SpiralTOF$^{\text{TM}}$-plus, it is clear that the two lipids have different localization. In the case of using a reflectron TOFMS, which cannot separate two masses, it cannot provide proper information of compounds and their localization. The size of measurement range is 10.46 × 6.06 mm. In the mass images on the top column, the mass-image pixel size is 20 µm, enabling high-resolution mass images to be created. The number of pixels is 158,000 and this indicates that the SpiralTOF$^{\text{TM}}$ can only create a mass image of one-fifth area compared to the SpiralTOF$^{\text{TM}}$-plus. In the mass images on the middle column and bottom column in Fig. 4, pixel binnings were performed with 3 × 3 and 5 × 5 to make the pseudo 60 µm and 100 µm pixel mass images. The number of pixels were 17,000 and 6,000, respectively (left-side

Fig. 3 Correlation diagram between mass resolution and data acquisition speed for MALDI-MSI.

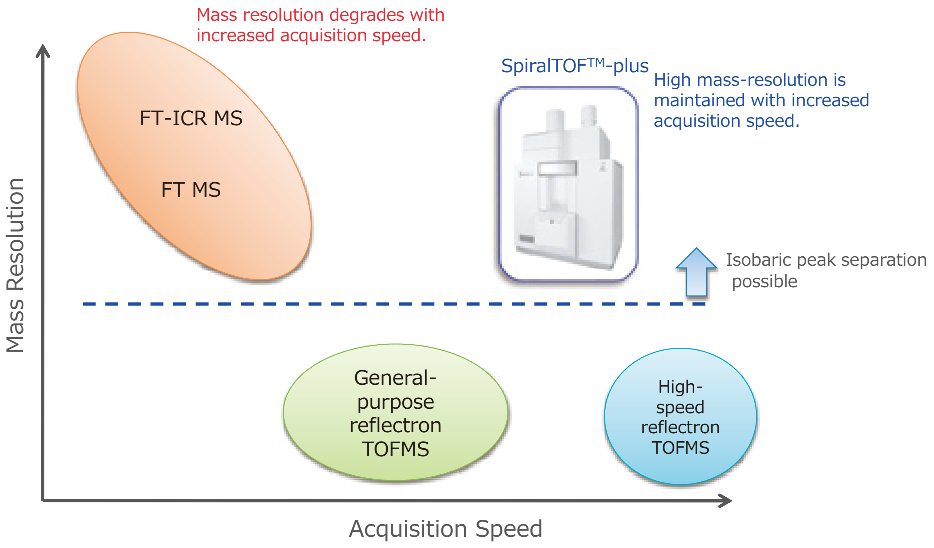

Fig. 4 Mass images acquired with SpiralTOF™-plus: PC(38:4) $[M+K]^+$ (*m/z* 848.557), left side and Galactosyl ceramide(C24h:1) $[M+K]^+$ (*m/z* 848.638), right side.

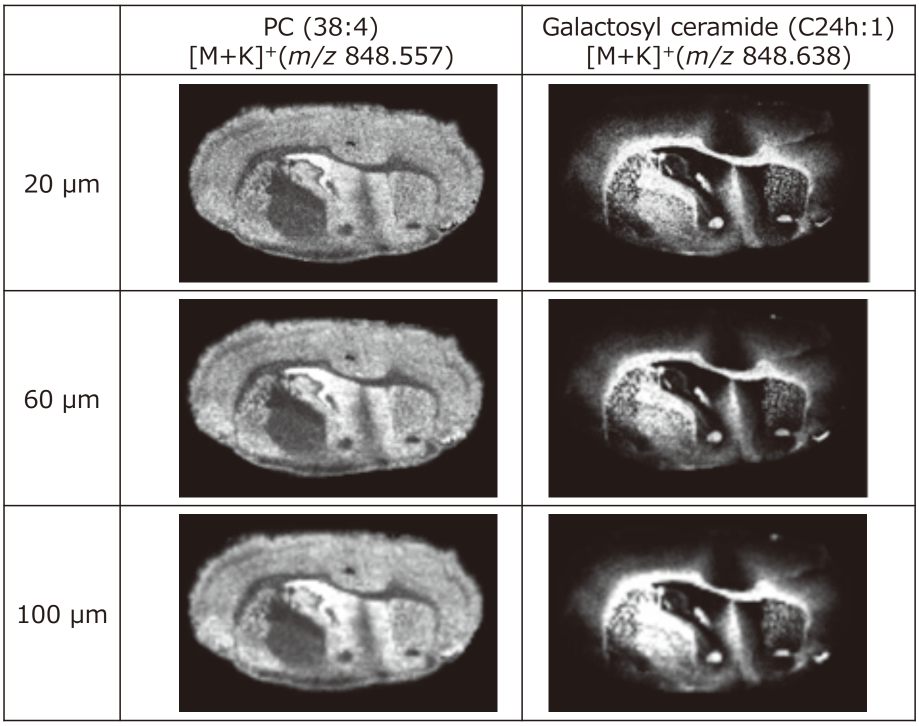

and right-side). It is estimated that, the time requried to acquire the data with these numbers of pixels is one hour and 22 minutes, respectively. Although the mass images show a little unclear contrast, it is sufficient to consider the preparation methods and to confirm the data repoducibility. The time for data acquistion, which will be comparable to time for making tissue selction or matrix application, will be shortened enough to eliminate bottle neck through the MSI measurement.

Conclusion

The SpiralTOF™-plus has maintained high mass-resolution provided by the SpiralTOF™ and has improved capabilities of MALDI-MSI. Due to higher data acquisition speed and the increased maximum number of pixels, the SpiralTOF™-plus has achieved more efficient study using MALDI-MSI, thus playing a significant role in various mass spectrometry studies.

GRAND ARM™ over GRAND ARM™

Atomic Resolution Analytical Microscope

JEM-ARM300F2
GRAND ARM™2

A New Atomic Resolution Electron Microscope has been released!
The “GRAND ARM™” has been upgraded.
This new “GRAND ARM™2” enables observation at ultrahigh spatial resolution with highly sensitive analysis over a wide range of accelerating voltages.

The newly developed FHP2 objective lens polepiece combines ultrahigh spatial resolution and highly sensitive X-ray analysis

The FHP objective lens polepiece, for observation at ultrahigh spatial resolution, has been upgraded.

① Highly sensitive X-ray analysis can be performed at ultrahigh spatial resolution. Compared with the previous FHP, more than double the X-ray detection efficiency (Total solid angle of 1.4 steradians) can be achieved with the FHP2.

② Low optical coefficients, low Cc coefficient & low Cs coefficient enable ultrahigh spatial resolution and highly sensitive X-ray analysis to be performed over a wide range of accelerating voltages.
(Guaranteed STEM resolution: 53 pm @300 kV, 96 pm @80 kV)*

*This is the case when the STEM Expanding Trajectory Aberration (ETA) Corrector is incorporated.

The WGP objective lens polepiece enables ultrahighly sensitive X-ray analysis and various types of In-situ experiments to be performed.

The WGP, which has a wide gap between its upper pole and its lower pole, is also available.

Because of a wide gap, the WGP enables,

① Large-sized SDDs to be brought closer to the specimen, allowing ultrahighly sensitive X-ray analysis to be performed.
(Total solid angle of 2.2 steradians)

② Thick special specimen holders are able to fit within the polepiece gap, making it possible for various types of In-situ experiments to be performed

JEOL Cs corrector & Corrector System Module (JEOL COSMO™)

Cs correctors developed by JEOL are used on the GRAND ARM™2.

Incorporating the FHP2 into this system can achieve a STEM spatial resolution of 53 pm, and using the WGP with this system can achieve a STEM spatial resolution of 59 pm. (@300 kV) JEOL COSMO™, Corrector System Module, makes it possible to execute aberration correction easily and quickly.

Cold Field Emission Electron Gun (CFEG) provided as a standard

CFEG, a highly stabilized cold field emission electron gun with a smaller energy spread is equipped as standard.

An enclosure not affected by external disturbances

This new enclosure is standard in order to reduce external disturbances such as air flow, changes of room temperature and acoustic noise.

Certain products in this brochure are controlled under the “Foreign Exchange and Foreign Trade Law” of Japan in compliance with international security export control. JEOL Ltd. must provide the Japanese Government with “End-user’s Statement of Assurance” and “End-use Certificate” in order to obtain the export license needed for export from Japan. If the product to be exported is in this category, the end user will be asked to fill in these certificate forms.

JEOL Ltd.
3-1-2 Musashino Akishima Tokyo 196-8558 Japan Sales Division Tel. +81-3-6262-3560 Fax. +81-3-6262-3577
www.jeol.com ISO 9001 • ISO 14001 Certified

ARGENTINA
COASIN S.A.C.I.yF.
Virrey del Pino 4071,
C1430CAM-Buenos Aires
Argentina
Tel. 54-11-4552-3185
Fax. 54-11-4555-3321

AUSTRALIA & NEW ZEALAND
JEOL (AUSTRALASIA) Pty.Ltd.
Suite 1, L2 18 Aquatic Drive
- Frenchs Forest NSW 2086
Australia
Tel. 61-2-9451-3855
Fax. 61-2-9451-3822

AUSTRIA
JEOL (GERMANY) GmbH
Gute Aenger 30
85356 Freising, Germany
Tel. 49-8161-9845-0
Fax. 49-8161-9845-100

BANGLADESH
A.Q. CHOWDHURY SCIENCE & SYNERGY PVT. LTD.
87, Suhrwardry Avenue, Floor 2
Baridhara, Dhaka1212
Bangladesh
Tel. 8802-9862272, 8953450, 8953501
Fax. 8802-9854428

BELGIUM
JEOL (EUROPE) B.V.
Planet II, Gebouw B
Leuvensesteenweg 542,
B-1930 Zaventem
Belgium
Tel.32-2-720-0560
Fax.32-2-720-6134

BRAZIL
JEOL Brasil Instrumentos Cientificos Ltda.
Av. Jabaquara, 2958 5° andar conjunto 52 ;
04046-500 Sao Paulo, SP
Brazil
Tel. 55-11-5070 4000
Fax. 55-11-5070 4010

CANADA
JEOL CANADA, INC.
3275 1ere Rue, Local #8
St-Hubert, QC J3Y-8Y6, Canada
Tel. 1-450-676-8776
Fax. 1-450-676-6694

CHINA
JEOL (BEIJING) CO., LTD.
Zhongkeziyuan Building South Tower 2F,
Zhongguancun Nansanjie Street No. 6,
Haidian District, Beijing, P.R.China
Tel. 86-10-6804-6321
Fax. 86-10-6804-6324

JEOL (BEIJING) CO., LTD., SHANGHAI BRANCH
2F-BC Room, Building A, Mingji Business Plaza,
No.207 Songhong Road, Changning District,
Shanghai 200335, P.R.China
Tel. 86-21-6248-4487
Tel. 86-21-5836-6350
Fax. 86-21-5836-3668

JEOL (BEIJING) CO., LTD., GUANGZHOU BRANCH
N1601, World Trade Center Building,
#371-375, Huan Shi Road East, Guangzhou,
Guangdong Prov., 510095, P.R.China
Tel. 86-20-8778-7848
Fax. 86-20-8778-4268

JEOL (BEIJING) CO., LTD., WUHAN BRANCH
Room A2118, Zhongshang Plaza Office Bldg.,
No. 7 Zhongnan Road, Wuhan,
Hubei, 430070, P.R.China
Tel. 86-27-8713-2567
Fax. 86-27-8713-2567

JEOL LTD. (BEIJING) CO., LTD., CHENGDU BRANCH
1807A Zongfu Building,
NO. 35 Zhongfu Road, Chengdu, Sichuan, 610016
P.R. China
Tel. 86-28-86622554
Fax. 86-28-86622564

EGYPT
JEOL SERVICE BUREAU
3rd Fl. Nile Center Bldg., Nawal Street,
Dokki, (Cairo), Egypt
Tel. 20-2-3335-7220
Fax. 20-2-3338-4186

FRANCE
JEOL (EUROPE) SAS
Espace Claude Monet, 1 Allee de Giverny
78290, Croissy-sur-Seine, France
Tel. 33-13015-3737
Fax. 33-13015-3747

GERMANY
JEOL (GERMANY) GmbH
Gute Aenger 30
85356 Freising, Germany
Tel. 49-8161-9845-0
Fax. 49-8161-9845-100

GREAT BRITAIN & IRELAND
JEOL (U.K.) LTD.
JEOL House, Silver Court, Watchmead,
Welwyn Garden City, Herts AL7 1LT, U.K.
Tel. 44-1707-377117
Fax. 44-1707-373254

GREECE
N. ASTERIADIS S.A.
56-58,S. Trikoupi Str. P.O. Box 26140
GR-10022, Athens, Greece
Tel. 30-1-823-5383
Fax. 30-1-823-9567

HONG KONG
FARMING LTD.
Unit No. 1009, 10/F., Prosperity
663 King's Road, North Point, Hong Kong
Tel. 852-2815-7299
Fax. 852-2581-4635

INDIA
JEOL INDIA PVT. LTD.
Unit No.305, 3rd Floor,
ABW Elegance Tower,
Jasola District Centre,
New Delhi 110 025, India
Tel. 91-11-4595-8000
Tel. 91-11-4595-8005
Tel. 91-11-4595-8017

JEOL INDIA PVT. LTD. Mumbai Office
214 E Square, Subhash Road,
Vile Parle (EAST),
Mumbai 400 057, India
Tel. 91-22-2612-9387

JEOL INDIA PVT. LTD. Bangalore Office
125, Brigade Road,
Unit No.402, Level 4, Palms Square,
Bangalore-560025, India
Tel. 91-80-4375-3351

JEOL INDIA PVT. LTD. Kolkata Office
Regus, The Legacy, 25 / A,
Shakespeare Sarani,
Kolkata - 700017, India
Tel. 91-98-3023-0484

JEOL INDIA PVT. LTD. Hyderabad Office
422, Regus Solitaire Business centre.
1-10-39 to 44, level 4, Gumidelli Towers, Old Airport Road,
Begumpet, Hyderabad - 500016, India
Tel. 91-40-6704-3708

INDONESIA
PT. TEKNOLABindo Penta Perkasa
Komplek Gading Bukit Indah Blok I/11
Jl. Bukit Gading Raya Kelapa Gading Permai,
Jakarta 14240, Indonesia
Tel. 62-21-45847057/58
Fax. 62-21-45842729

ITALY
JEOL (ITALIA) S.p.A.
Palazzo Pacinotti - Milano 3 City,
Via Ludovico il Moro, 6/A
20080 Basiglio(MI) Italy
Tel. 39-02-9041431
Fax. 39-02-90414343

KOREA
JEOL KOREA LTD.
Dongwoo Bldg. 7F, 1443, Yangjae Daero,
Gangdong-Gu, Seoul, 05355, Korea
Tel. 82-2-511-5501
Fax. 82-2-511-2635

KUWAIT
Ashraf & CO. Ltd.
P.O.Box 3555 Safat 13036, Kuwait
Tel. 965-1805151
Fax. 965-24335373

MALAYSIA
JEOL (MALAYSIA) SDN.BHD.
508, Block A, Level 5,
Kelana Business Center,
97, Jalan SS 7/2, Kelana Jaya,
47301 Petaling Jaya, Selangor, Malaysia
Tel. 60-3-7492-7722
Fax. 60-3-7492-7723

MEXICO
JEOL DE MEXICO S.A. DE C.V.
Arkansas 11 Piso 2
Colonia Napoles
Delegacion Benito Juarez, C.P. 03810
Mexico D.F., Mexico
Tel. 52-5-55-211-4511
Fax. 52-5-55-211-0720

Middle East
JEOL GULF FZCO
P.O. Box No. 371107
Dubai Airport Free Trade Zone West Wing 5WA No. G12,
Dubai, UAE
Tel. 971-4-609-1497
Fax. 971-4-609-1498

PAKISTAN (Karachi)
ANALYTICAL MEASURING SYSTEM (PVT) LTD. (AMS LTD.)
14-C Main Sehar Commercial Avenue Lane 4,
Khayaban-e-Sehar,
D.H.A-VII, Karachi-75500, Pakistan
Tel. 92-21-35345581/35340747
Fax. 92-21-35345582

PANAMA
PROMED S.A.
Parque Industrial Costa del Este
Urbanizacion Costa del Este
Apartado 0816-01755, Panama, Panama
Tel. 507-303-3100
Fax. 507-303-3115

PHILIPPINES
JATEC Philippines Corporation
28 Floor, The Enterprise Center Tower 2,
Ayala Avenue corner Paseo de Roxas,
Brgy. San Lorenzo, Makati City, 1226 Philippines
Tel. (632) 849 3904

PORTUGAL
Izasa Portugal Lda.
R. do Proletariado, 1
2790-138 CARNAXIDE, Portugal
Tel. 351-21-424-73-00
Fax. 351-21-418-60-20

QATAR
Mannai Trading Company W.L.L.
ALI Emadi Complex,
Salwa Road P.O.Box 76, Doha, Qatar
Tel. +974 4455-8216
Fax. +974 4455-8214

RUSSIA
JEOL (RUS) LLC
Krasnoproletarskaya Street, 16,
Bld. 2, 127473, Moscow,
Russian Federation
Tel. 7-495-748-7791/7792
Fax. 7-495-748-7793

SAUDI ARABIA
ABDULREHMAN ALGOSAIBI G.T.C. (Riyadh)
Algosaibi Building-Old Airport Road
P.O. Box 215, Riyadh-11411, Saudi Arabia
Tel. 966-1-477-7932

SCANDINAVIA
SWEDEN
JEOL (Nordic) AB
Hammarbacken 6A, Box 716, 191 27 Sollentuna
Sweden
Tel. 46-8-28-2800
Fax. 46-8-29-1647

SINGAPORE
JEOL ASIA PTE.LTD.
2 Corporation Road
#01-12 Corporation Place
Singapore 618494
Tel. 65-6565-9989
Fax. 65-6565-7552

SOUTH AFRICA
ADI Scientific (Pty) Ltd.
370 Angus Crescent,
Northlands Business Park, 29 Newmarket Road
Northriding, Ranburg, Republic of South Africa
Tel. 27-11-462-1363
Fax. 27-11-462-1466

SPAIN
IZASA Scientific SLU.
Argoneses, 13, 28108 Alcobendas,
Madrid, Spain
Tel. 34 902 20 30 80
Fax. 34 902 20 30 81

SWITZERLAND
JEOL (GERMANY) GmbH
Gute Aenger 30
85356 Freising, Germany
Tel. 49-8165-77346
Fax. 49-8165-77512

TAIWAN
JIE DONG CO., LTD.
7F, 112, Chung Hsiao East Road,
Section 1, Taipei, Taiwan 10023 (R.O.C.)
Tel. 886-2-2395-2978
Fax. 886-2-2322-4655

For NMR & Mass Spectrometer Products:
TechMax Technical Co., Ltd.
5F., No.11, Wuquan 2nd Rd., Wugu Dist.,
New Taipei City 248, Taiwan (R.O.C.)
Tel. 886-2-8990-1779
Fax. 886-2-8990-2559

For Semiconductor Products:
JEOL TAIWAN SEMICONDUCTORS LTD.
2F-2, No. 192, Dongguang Rd.
East Dist., Hsinchu City 30069,
Taiwan (R.O.C.)
Tel. 886-3-571-5656
Fax. 886-3-571-5151

THAILAND
BECTHAI BANGKOK EQUIPMENT & CHEMICAL CO., Ltd.
300 Phaholyothin Rd. Phayathai, Bangkok 10400,
Thailand
Tel. 66-2-615-2929
Fax. 66-2-615-2350/2351

JEOL ASEAN TECHNICAL CENTER (JATC)
MTEC building room 533
114 Moo9, Thailand Science Park
Paholyothin Rd., Klong 1, Klong Luang,
Pathumthani 12120
THAILAND
Tel. 66-2-564-7738
Fax. 66-2-564-7739

THE NETHERLANDS
JEOL (EUROPE) B.V.
Lireweg 4, NL-2153 PH Nieuw-Vennep,
The Netherlands
Tel. 31-252-623500
Fax. 31-252-623501

TURKEY
Tekser A.S.
Kartal Cad. No: 55/3 Inonu Wah.,
Atasehir 34755, Istanbul, Turkey
Tel. 90-216-5736470
Fax. 90-216-5736475

USA
JEOL USA, INC.
11 Dearborn Road, Peabody, MA 01960, U.S.A.
Tel. 1-978-535-5900
Fax. 1-978-536-2205/2206

JEOL USA, INC. WEST OFFICE
5653 Stoneridge Drive Suite #110
Pleasanton, CA 94588, U.S.A.
Tel. 1-925-737-1740
Fax. 1-925-737-1749

VENEZUELA
GOMSA Service and Supply C.A.
Urbanizacion Montalban III
- Residencias Don Andres - Piso 7 - Apartomento 74
Avenida 3, entre calles 7 y 6
Montalban, Caracas, Venezuela
Tel. 58-212-443-4342
Fax. 58-212-443-4342

VIETNAM
TECHNICAL MATERIALS AND RESOURCES
IMPORT-EXPORT JOINT STOCK COMPANY(REXCO)
Hanoi Branch
SALES & SERVICE
155-157 Lang Ha Street, Dong Da District, Hanoi, Vietnam
Tel. +84 (43) 562 0516
Fax. +84 (43) 853 2511

(Ser. No. 138)

No. 9401F031C Printed in Japan, Kp